Computational Studies of Correlated 1D and 3D Systems: A Density Functional Theory Approach

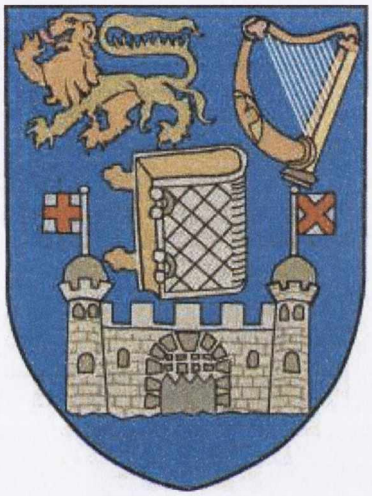

Akinlolu Akande

A thesis submitted for the degree of
Doctor of Philosophy
School of Physics
Trinity College Dublin

March 2011

Declaration

I, Akinlolu Akande, hereby declare that this dissertation has not been submitted as an exercise for a degree at this or any other University.

It comprises work performed entirely by myself during the course of my Ph.D. studies at Trinity College Dublin. I was involved in a number of collaborations, and where it is appropriate my collaborators are acknowledged for their contributions.

A copy of this thesis may be lended or copied by the Trinity College Library upon request by a third party provided it spans single copies made for study purposes only, subject to normal conditions of acknowledgement.

Abstract

This thesis describes a number of theoretical investigations into the electric and magnetic properties of one-dimensional and three-dimensional correlated systems. Our studies are based on suitable and efficient implementations of different approximations to the exchange-correlation (XC) energy functional of ground state density functional theory (DFT).

Part I is devoted to investigate the accuracy and the applicability of lattice DFT (LDFT) to strongly correlated one-dimensional systems. We perform calculations within the framework of the Bethe Ansatz local density approximation (BALDA) to the LDFT formulation of the Hubbard model. This approximation is capable of describing both Luttinger liquids and Mott-insulators. In an attempt to establish a general consensus concerning the accuracy of LDFT-BALDA scheme, a set of benchmark calculations are performed with numerically accurate methods such as exact diagonalization, density matrix renormalization group and Bethe Ansatz techniques.

We validate the capability of the LDFT-BALDA to compute ground state properties such as total energies and the static linear polarizabilities for the Hubbard model. The response of the exact XC potential is found to point in the same direction as an external electric field. This is well reproduced by the BALDA approach, although the fine details depend on the specific parameterization for the local approximation. A numerical proof for the non-locality of the XC functional is also provided.

Furthermore, an expression for the XC energy of the Hubbard Hamiltonian including a vector potential is developed and implemented within the BALDA for the

first time. This allows us to construct an extention of LDFT to current-LDFT. Transport properties such as persistent current and Drude weight are studied with this new scheme. The theoretical method explored in this work is an important and promising step forward in the study of large one-dimensional systems. An example of these is ultracold fermions on optical lattices, known to be versatile and robust for probing fundamental condensed-matter physics problems.

Finally Part II investigates the bandstructures and exchange interactions for a number of prototypical correlated materials by using an approximate atomic self-interaction corrections (ASIC) method to DFT. In general, the ASIC scheme drastically improves the bandstructure which, for almost all the cases investigated, resemble closely available photo-emission data. In contrast, the results for the exchange parameters suffer from similar problems encountered with the LDA. This reflects the subtle interplay between exchange and correlation energy, not captured in full by the ASIC.

Acknowledgements

"So then it is not of him that willeth, nor of him that runneth, but of God that sheweth mercy" Romans 9:16. *"A person cannot receive even one thing unless God gives it from heaven"* John 3:27.

My first gratitude goes to God from whom wisdom, strength, mercy and grace flow. Without Him I could do nothing including this Ph.D. so unto Him I return all the glory, honour and praise for the successful completion of this programme. He stood by my side and in Him I found solace even when the goings were tough.

My supervisor, Prof. Stefano Sanvito, is a man of great heart and intelligence. His diligence, unquenchable curiosity and enthusiasm for scientific research have made him unparalleled amongst his colleagues. I am particularly grateful for his extraordinary patience in providing practical guidance to both scientific and personal issues during the course of this Ph.D. I have benefitted tremendously from his teachings and continual supports and encouragements. Also, his wife, Stefania (who incidentally was an executive officer in the School of Physics) has also been helpful both on personal level especially when I first arrived and on getting administrative work done.

Computational Spintronic Group is one of the largest groups in the School of Physics. There are many people to thank for their assistance one way or the other. When I joined the group in 2005, I met graduate students: Alex Rocha (a brilliant chap always willing to be of assistance anytime), Chaitanya Das Pemmaraju (responsible for the implementation of ASIC in Siesta), Maria Stamenova (an unassuming

and kind lady from whom I have had fruitful discussions), Ivan Rungger (whose insights on computational issues and physics generally were very helpful), Ruairi Hanafin and Will Lee (whom we started almost the same time). There were also two postdocs as at the time: Miguel Afonso Oliveira and Tom Archer (who is still with the group) provided system administration supports.

Ever since, the group has "exploded" in number: Nadjib Baadji (who provided assistance for various computational techniques and insights that have truly enlightened this work), Durga Sankar Kusanakurthi, Andrea Droghetti (whose insightful suggestions, particularly at the beginning of the use of LDFT, helped to move the part forward), Nuala Caffrey (a level-headed lady who at one point or the other has taken time to edit many of my scientific write-ups including some parts of this thesis), Aaron Hurley, Anna Pertsova, Mauro Mantega, Kapildeb Dolui, Clotilde Cucinotta, Igor Popov, Xihua Chen, Sandip Bhattacharya, Thomas James Cathcart and Awadhesh. I will not forget to mention those I shared the same office with and have made the experience pleasurable. They were all members of Dr. Mauro Ferreiras group: Stephen Power, Luiz Felipe Pereira (who was also finishing the same time with me), former students David Kirwan and Andrew Wall and former postdoc Claudia Gomes Rocha. Dr. Mauro Ferreira is also an academia I hold in high esteem. He is an amazing teacher with an enthusiasm for physics that is contagious.

My research was supported by Science Foundation of Ireland under the grants SF105/RFP/PHY0062 and 07/IN.I/1945. Computational resources have been provided by HEA IITAC project managed by the Trinity Centre for High Performance Computing (TCHPC) and by the Irish Centre for High End Computing (ICHEC).

Without the immense spiritual, emotional and physical supports that I have received from my immediate family, there is no doubt that the programme would have been frustrating. My wife, Adebola Morayo, has been terrific in giving cheerful and much needed assistance. We both went through 'highs' and oftentimes 'lows' during

the programme. Her patience, endurance, love and words of encouragement gave me impetus to continue until I finished. Our son, Daniel, was graciously understanding. Many times, I left the house very early in the morning before he woke up and returned late in the evening while he was asleep. I would be told that the first person he asked after was his daddy. I acknowledge his love and understanding during those times. I will like to thank my parents, my parent-in-laws and my extended family members. Their prayers are always helpful and supportive.

The Redeemed Christian Church of God (RCCG) - Miracle Land, Seat of Mercy and Kingdom Connection - made my spiritual life worthwhile during my stay in Ireland. I have shared fellowship and friendship with a lot of brethren who have inspired me and have been a source of blessing to my family especially my beloved Pastor and Mrs. Alex Alajiki.

I want to appreciate a family friend in Nigeria - Mr. and Mrs. Okiki - whose mentorship is one of a kind. They are always there to give my family support. I thank the family of Pastor and Mrs. Tunde Jaiyebo for their special solidarity for my family in prayers and support.

This programme gave me the opportunity to make a number of friends with a lot of people. I will particularly appreciate the families of the Oguntoyinbos (who are always warm-hearted and kind to my family), the Olayiwolas (whose family has taken mine as personal friends), Omolara Igonor (who edited some part of this work), the Olatuyis (whom we lived very close to their house and we shared some of their things), the Olubiyis (who rented out their BQ to us when we needed it most), the Aperes (who always welcome us to their home anytime there is need for it), the Anjorins (especially Dami who did some rearrangements at the beginning of the writing), the Oduwoles and lastly all members of the African Change Initiative (ACI) who we are committed to the great cause of making positive changes in the continent of Africa.

Finally, I have been privileged to pass through the tutorship of many advisors who have positively contributed to my academics in no small way. Amongst them are Prof. Sandro Scandolo, Prof. Olatunde Akinlade, Dr. Caetano Miranda, Dr. G. A. Adebayo and Dr. (Mrs.) Alatise.

Contents

List of Figures

List of Tables

Chapter 1

General Introduction

Research in condensed matter physics is geared towards understanding the macroscopic behaviour of various quantum mechanical systems, beginning from a detailed description of the individual particles and how they interact with each other. Quite a number of problems in this field have been effectively described within a single particle picture [1], i.e. by using the band theory, where each electron moves in the periodic potential created by the positive ions and by the average potential of all the other electrons (this forms the mean field). Despite the success that single particle theory enjoyed in the twentieth century, it was not long before it was shown that band theory breaks down for a large number of insulating $3d$ transition metal compounds like NiO and CoO [2]. Band theory in fact predicts them to be metallic whereas they are all insulators. The reason for the erroneous band theory description was early attributed to neglecting contributions to the repulsive Coulomb interaction (going beyond the mean field level) between the electrons in the d-orbitals by Mott and Peierls [3]. Later, Mott [4] and Hubbard [5] indeed showed that if the electron-electron interaction is larger than the bare electronic bandwidth, the system will be indeed an insulator.

Therefore, a proper description of *electron correlation*, the fact that electrons feel the presence of each other's motion due to the Coulombic force acting between

them, is critical for many different classes of materials in condensed matter. Effects due to electron correlation are defined from an operational point of view as any purely electronic phenomenon which can not be explained within the independent-electron (the mean field) approximation [6]. Thus, material systems whose electronic structure cannot be described at a mean field level are conventionally referred to as strongly correlated systems.

Studies on these materials have given tremendous insights into phenomena such as magnetism, the quantum Hall effect, charge and spin localization, charge ordering, metal-insulator transitions and superconductivity, to mention just a few. Also, phenomena such as the Kondo effect [7], where magnetic impurities are embedded in metals, are dominated by electron correlations. This highlights the important role that electron-electron interaction plays in many-body fermionic systems, such as transition metal oxides, rare-earth elements and actinides, their compounds and alloys and some organic compounds.

A very important theoretical framework that has been employed to understand the effects of electronic interactions in material systems is based on Landau's Fermi liquid theory [8]. In this theory, electrons behave qualitatively as quasi-free particles; that is, the only effects of any interaction with other electrons are the modification of their effective mass and the possibility of being scattered [9]. For many years, the theory was used to study electron dynamics in solids with great theoretical success until it was realized that some systems completely deviate from predicted results. In low dimensional systems, especially one dimension, the Fermi liquid theory breaks done and is replaced by a new state of matter known as Luttinger liquid, a concept introduced by Haldane [10] after the exactly solvable Luttinger model [11].

There has been much theoretical progress in the description of the Luttinger liquid as well as experimental realization of systems that could be candidates for such a one-dimensional physics [12]. Advances in nanotechnology have made it possible

to fabricate one-dimensional systems such as carbon nanotubes [13], atomic wires on insulating surfaces [14], inorganic crystalline nanowires [15] and organic materials like Bechgaard salts [12, 16]. Their unique characteristics, as compared to bulk materials, make them good candidates for several applications in different fields including nanoelectronics, pharmaceutical and cosmetics. In addition, a system comprising of many parallel one-dimensional chains is considered to be a convenient geometry for quantum information processing [17].

More recent experimental studies have shown that some conjugated polymers do not behave like two- or three-dimensional materials but as one-dimensional metals [9, 18], in contrast to previously held beliefs. These polymers are hopeful candidates in the quest to make electronic devices from organic materials. Although the field still presents many challenges, appreciable progress has led to the development of promising prototypes of thin-film transistor and photovoltaic devices, and even commercialization of organic light-emitting diodes [9]. It is evident that theoretical studies on one-dimensional objects will provide a powerful platform for the development of new ideas with promising applicability.

In any dimension, simplified models (in contrast to fully quantitative electronic structure theories such as density functional theory) are often adopted to obtain valuable insights into the behaviour of complicated systems. There are two classes of models used in the study of interacting fermions. The first one is formed by *lattice models*, where electrons are tightly bound to the regular sets of spatially defined points produced by a lattice of atomic nuclei, while the electrons are able to move between adjacent nuclei. The second class of models is populated by *continuum models*. Here, an interacting electron fluid is moving in a uniform background of positive charge.

Quite generally, lattice models have a richer phenomenology than the continuum ones, since the second can be obtained as a limiting case of the first [19]. For example,

the peculiarity of some features like the SU(2) symmetry in the Hubbard model - a lattice model that will be discussed in detail later - is directly attributed to the discreteness of the lattice [19]. Moreover, models that describe itinerant electrons on discrete lattices offer a wider range of numerical algorithms to solve them than the continuum ones. Nonetheless, the continuum models describe certain aspects of the physics of the lattice models and are also interesting in their own right (see reference [19] for examples), mostly because some of the solutions can be derived analytically. In this thesis, however, we mostly focus on lattice models.

One-dimensional systems are often easier to handle for a theorist than their two- or three-dimensional counterparts. In particular, one-dimensional strongly correlated systems modeled by means of effective lattice Hamiltonians, but capable of capturing the relevant physical properties arising from electron correlation, are usually mathematically tractable and general enough to be applied to a variety of problems. Among the many effective Hamiltonians that one can construct is the Hubbard model [20, 21, 22] which has enjoyed a vast popularity since it can capture the subtle interplay between Coulomb repulsion and kinetic energy, while remaining simple.

For instance, progress in ultra-cold atom experiments is considered to be one of the significant advancement in recent years [23] allowing experimental tests of methods in condensed matter. In particular, one can experimentally ascertain the Hubbard model and its extentions by using a fermionic quantum gas loaded into an optical lattice [24]. Within this atomic approach, the Hubbard Hamiltonian is obtained as a direct result of the optical lattice potential created by interfering laser fields and short-ranged ultracold collisions. In one-dimension (1D), a sinusoidal optical potential are easily created for trapped atoms [25] and thus gives a platform to simulate the physics of the Hamiltonian. Theoretical calculations can then be compared directly with results obtained from such systems.

Although exact solutions of the Hubbard model are known in particular limits

[26], a general one for an arbitrary system, which can be finite and inhomogeneous, requires a numerical treatment. This however represents a severely demanding task, since the Hilbert space associated to the Hubbard Hamiltonian for L sites is 4^L dimensional, so that exact (Lanczos) diagonalization (ED) can only handle a relatively small number of sites. Other many-body approaches, such as the density matrix renormalization group (DMRG) [27, 28], extend the range to a few hundred sites, but little is possible beyond that limit. It would be then useful to have a method capable of describing accurately the ground state and still having the computational overheads of a mean field approach. Such a method is provided by lattice density functional theory (LDFT).

LDFT was initially proposed by Gunnarsson and Schonhammer [29, 30] as an extension of standard, *ab initio*, DFT [31, 32] to lattice models. The theory essentially reformulates the Hohenberg-Kohn theorem and the Kohn-Sham construction in terms of the site occupation instead of the electron density. Although originally introduced with a pedagogical purpose, LDFT has enjoyed a growing success and it has been already applied to a diverse range of problems. These include fundamental aspects of DFT and of the Hubbard model, such as the band-gap problem in semiconductors [29], the dimerization of 1D Hubbard chains [33] and the formation of the Mott-Hubbard gap [34]. LDFT has also been employed for investigating effects at the nanoscale traceable to strong correlation, like the behavior of impurities [35], spin-density waves [36] and inhomogeneity [37], as well as more exotic aspects like the phase diagram of harmonically confined 1D fermions [38] and that of ultracold fermions trapped in optical lattices [39, 40, 41]. More recently LDFT has been extended to the time-dependent domain [42], to quantum transport [43] and to response theory [44].

As in standard DFT, LDFT is also in principle exact. However its practical implementation is limited by the accuracy of the unknown exchange correlation (XC)

functional, which introduces many-body effects into the theory. The construction of an XC functional begins with choosing a reference system, for which some exact results are known. These impose a number of constraints that the XC functional must satisfy, as for example its asymptotic behavior or its scaling properties. The functional is then built by interpolating and fitting to known many-body reference results. Such a construction for instance has been employed in the case of the local density approximation (LDA) in *ab initio* DFT. The reference system in two and three dimensions is usually an electron gas of some kind, since one aims at reproducing a Fermi liquid. However in 1D the known ground state has a Luttinger-liquid nature and so the reference system should be chosen accordingly. In the case of the Hubbard Hamiltonian in 1D a powerful result is that obtained by Lieb and Wu [45] for the homogeneous case by using the Bethe Ansatz (BA). This is the basis for constructing an XC functional for the Hubbard model in 1D [34, 35].

This thesis investigates both one-dimensional and three-dimensional correlated systems using efficient theoretical methods. We divide this work into two rather independent parts. The focus of the first one (Chapters 2, 3, 4 and 5) is on one-dimensional systems while that of the second part (Chapters 6 and 7) is on three-dimensional ones.

In the first part, we employ a range of existing approximations to LDFT and its corresponding extension to current-LDFT (CLDFT) in our studies. We begin by calculating ground state energies of one-dimensional finite-site systems described by the homogeneous Hubbard model with different boundary conditions and over a broad range of parameters. The results are compared with those obtained with the numerically exact methods in order to test the reliability of these approximations to the XC potentials. We perform similar calculations for the inhomogeneous Hubbard Hamiltonian.

Next, we evaluate the ability of the approximations to the XC functional for

the 1D Hubbard model to predict the electrical response of finite 1D chains to an external electric field both far from and in the vicinity of the Mott transition. This is relevant, not just as a test for Hubbard LDFT, but also for understanding real materials whose electrical response can be mimicked in terms of the Hubbard model [46]. In particular the 1D case can provide important insights into the nonlinear optical properties of polymers [47].

We then provide a scheme to construct a new LDA-based XC potential within the CLDFT for one-dimensional Hubbard model. The resulting functional is applied to study mesoscopic rings with a view to describe the physics of Ahanorov-Bohm (AB) rings and also to test its performance. We calculate ground state properties such as ground state energies, persistent current and Drude weight of Hubbard rings with repulsive interactions enclosed by a magnetic flux. The accuracy and capability of this functional to capture the periodic variation of ground state energy and corresponding persistent current as a function of the magnetic flux is discussed. Finally, its limitations compared to other numerical procedures are identified.

The main goal of the second part is to investigate the magnetic behaviour of several systems using the computationally efficient atomic self-interaction correction (ASIC) scheme in DFT. The aim of this part is to quantitatively describe magnetic interactions, namely extracting exchange couplings, J, of important systems like ionic insulators and some transition metal oxides. In particular, we map total energy calculations onto a Heisenberg model and compare the calculated exchange constants to available experimental data as well as to other values reported in the literature. The accurate description of this quantity is useful for evaluating the Curie or Néel temperature, the magnetic susceptibility and also to interpret neutron diffraction experiments. A number of these systems are becoming increasingly interesting due to their modern magnetoelectronic applications, which makes the understanding of their magnetic properties crucial. Indeed, theoretical studies in this area are further

encouraged, especially for systems where experimental data are not available, in order to explore their potential technological applications.

The thesis is organized in the following way:

In Chapter 2, we give the theoretical background to the many concepts used. We begin by introducing various effective lattice Hamiltonians often used to describe quantum systems. Next, we discuss the Hubbard model in more detail, being the model of interest for the first part of this work. We then briefly introduce the basic idea of the Fermi and Luttinger liquids as used in describing interacting systems. Since one-dimensional systems are our main consideration, we summarize the BA technique for the homogeneous Hubbard model. Finally, the main concepts behind DFT, starting from the basic of Hohenberg and Kohn theorems to the various approximations to the XC potentials are presented.

In Chapter 3, we provide an overview of some numerical methods often used to treat low-dimensional strongly correlated systems. We present a very brief introduction to ED by using the Lanczos method, the numerical renormalization group (NRG) and the DMRG. In addition, the key idea of LDFT is explained for the one-dimensional Hubbard model. Finally, the approximations to the XC potential within Bethe Ansatz local density approximation (BALDA) in its spin-polarized and non spin-polarized forms are outlined. Codes implementing all the various flavours of the XC potential within BALDA and those of the self-consistency cycle of the DFT have been written by us from the scratch.

In Chapter 4, we report results for the LDFT within the BALDA when applied to some ground state properties. Ground state energies of different class of homogeneous and inhomogeneous systems are calculated and compared with other numerically exact methods. We also present numerical calculations on the linear polarizabilities

of finite 1D chains in the presence of an external electric field. Our strategy is that of constantly comparing our DFT results with those obtained with highly accurate many-body schemes. In particular we use ED for small chains and the DMRG method for larger systems. We discuss results, first for the electrical polarizabilities and then for the response of the XC potential to an external electric field. Finally, we carry on a numerical investigation on the validity of the local approximation to the XC functional.

Chapter 5 aims at introducing our extension to the existing LDFT formulation within the BALDA of references [34, 35, 36] to CLDFT for the one-dimensional Hubbard model. The transport properties of mesoscopic Hubbard rings threaded by a magnetic flux are the subject of investigation. We begin with analytical solutions for non-interacting quantum rings. We outline the BA solutions to a homogeneous ring with magnetic flux when Coulomb interaction is switched on within the Hubbard model. We have written a code solving the equations of the BA numerically. Then we introduce CLDFT and its LDA to the XC potential where we have written, from the scratch, codes implementing the formalism. Results for ground state energies, persistent current and Drude weight for the repulsive homogeneous and inhomogeneous case are reported and compared with other numerically established methods.

Chapter 6 introduces the numerical framework of *Siesta*, an advanced DFT code using pseudopotentials. Also, additional functionals to account for self-interaction errors in a computationally efficient scheme based on atomic orbitals are presented. Finally, the so called DFT+U within the LDA, which is important in describing strongly correlated electron systems, is briefly outlined.

In Chapter 7, we investigate the performance of the ASIC when calculating exchange parameters for interesting solid state systems. We begin with hypothetical linear chains of hydrogen and helium often used as a benchmark in quantum chem-

istry. We then present detailed studies using ASIC on ionic antiferomagnet and transition metal oxides.

Finally, results for the two parts are summarized in Chapter 8. We highlight perspectives for further theoretical investigations in the subject of LDFT for strongly correlated systems. Also we provide outlook for future work in estimating exchange parameters.

This thesis has five appendices. Appendix A includes the solution of a non-interacting fermion gas. The expression for an exact spin-polarized XC potential for 1D repulsive Hubbard model is derived in appendix B. We give in appendix C the BALDA for the CLDFT. Appendix D contains tables to generate the contour plots in Chapter 4. Lastly, appendix E gives the list of publications from this work.

Part I

Chapter 2

Theoretical Background

2.1 Lattice model Hamiltonians

As already pointed out in the introduction, model Hamiltonians are often adopted as the starting point of developing a quantum theory for correlated electrons instead of investigating real quantum many-body systems. Effective Hamiltonians contain the essential features of the problem under investigation while integrating out any unwanted parts of the Hamiltonian's spectrum, i.e. eliminating unnecessary computational overheads. In this section, we will illustrate how this "reduction" of degrees of freedom can be done. Let us consider a general Hamiltonian governing the dynamics of N electrons with mass m_e and charge e,

$$\hat{H} = \sum_{i=1}^{N} \left[\frac{\vec{p}_i^{\,2}}{2} + v(\vec{x}_i) \right] + \sum_{1 \le i < j \le N} \frac{e^2}{|\vec{x}_i - \vec{x}_j|} = \sum_{i=1}^{N} \hat{T}(\vec{x}_i) + \frac{1}{2} \sum_{i<j}^{N} \hat{V}(\vec{x}_i, \vec{x}_j), \qquad (2.1)$$

where $\vec{x}_i$ denotes the position and $\vec{p}_i$ the momentum of i-th particle. The potential, $v(\vec{x}_i)$, has the periodicity of the lattice structure. Here we consider natural units $\hbar = m_e = 1$ and the lattice spacing a is set to unity. In general, $\hat{T}$ denotes both the kinetic energy of the particles and their interaction with the ionic lattice, while $\hat{V}$ is the potential energy of the interaction between particles.

Using the second quantization language, the equation (2.1) becomes

$$\hat{H} = \sum_{ij,\sigma} t_{ij}(\hat{c}^{\dagger}_{i\sigma}\hat{c}_{j\sigma} + hc) + \frac{1}{2}\sum_{ijkl}\sum_{\sigma\sigma'} V_{ijkl}\hat{c}^{\dagger}_{i\sigma}\hat{c}^{\dagger}_{j\sigma'}\hat{c}_{k\sigma'}\hat{c}_{l\sigma}, \tag{2.2}$$

where the operator $\hat{c}^{\dagger}_{i\sigma}$ ($\hat{c}_{i\sigma}$) is called the creation (annihilation) operator because it creates (destroys) an electron of spin σ at the single-particle orbital ϕ_i located at site i. The operators $\hat{c}^{\dagger}_{i\sigma}$ and $\hat{c}_{i\sigma}$ obey the anticommutation rules (see Appendix A). The coefficients t_{ij} and V_{ijkl} are the matrix elements of the operators $\hat{T}$ and $\hat{V}$ respectively, which are defined as

$$\begin{aligned} t_{ij} &= \int d\vec{x}\phi^{*}_{i}(\vec{x})\hat{T}\phi_j(\vec{x}), \\ V_{ijkl} &= \int d\vec{x}\int d\vec{x}'\,\phi^{*}_{i}(\vec{x})\phi_k(\vec{x})\hat{V}(\vec{x},\vec{x}')\phi^{*}_{j}(\vec{x}')\phi_l(\vec{x}'), \end{aligned} \tag{2.3}$$

while the indices i, j, k, l run over all the possible lattice sites, L.

Among all the matrix elements V_{ijkl}, the following three types carry a particular meaning and govern specific physical processes [48]:

- The *direct terms*, $V_{ijij} \equiv V_{ij}$[1], involve integral over square moduli of orbitals and couple density fluctuations at neighbouring sites. This contributes $\sum_{i\neq j}\sum_{\sigma\sigma'} V_{ij}\hat{n}_{i\sigma}\hat{n}_{j\sigma'}$ to the second term of the equation (2.2) ($\hat{n}_i = \sum_{\sigma}\hat{c}^{\dagger}_{i\sigma}\hat{c}_{i\sigma}$). This term is able to induce global instabilities in the charge density distribution known as charge density wave instabilities observed in materials like the magnetite (Fe_3O_4) [6].

- The *exchange terms*, $V_{ijji} \equiv J_{ij}$[2], describe magnetic correlations among the electron spins. By using Pauli Matrix identities, the exchange part of the

[1] $V_{ij} = \int d\vec{x}\int d\vec{x}'|\phi_i(\vec{x})|^2\frac{1}{|\vec{x}-\vec{x}'|}|\phi_j(\vec{x}')|^2 > 0$

[2] $J_{ij} = \int d\vec{x}\int d\vec{x}'\frac{\phi^{*}_{i}(\vec{x})\phi^{*}_{j}(\vec{x})\phi^{*}_{j}(\vec{x}')\phi^{*}_{i}(\vec{x}')}{|\vec{x}-\vec{x}'|} > 0$

electron-electron interaction can be written as

$$\sum_{i\neq j}\sum_{\sigma\sigma'} V_{ijji}\hat{c}^{\dagger}_{i\sigma}\hat{c}^{\dagger}_{j\sigma'}\hat{c}_{i\sigma'}\hat{c}_{j\sigma} = -2\sum_{i\neq j} J_{ij}(\hat{\mathbf{S}}_i\hat{\mathbf{S}}_j + \frac{1}{4}\hat{n}_i\hat{n}_j). \tag{2.4}$$

From the equation (2.3), $J_{ij} > 0$ so that the energy is minimized when the spins point in the same direction. Therefore, this term tends to induce *ferromagnetic order.*

- The *on-site Coulomb terms*, $V_{ijkl} \equiv V_{iiii}$, where the atoms are very well separated and the overlap between neighbouring orbitals is weak. The Coulomb interaction strengths, $V_{iiii} = 2U$[3], (factor 2 is from the spin summation), dominate the interaction mechanism.

Let us neglect all the terms mentioned with the exception of nearest neighbour contribution in the hopping integral, t_{ij} and the on-site Coulomb terms. For identical lattice sites, the hopping integral reduces to $t_{ij} = -t\delta_{\langle ij\rangle}$ $(t > 0)$, where $\langle ij\rangle$ implies adjacent sites. The effective Hamiltonian can be finally written in a simplified form known as the **Hubbard model** [21],

$$\hat{H}_U = -t\sum_{\langle ij\rangle\sigma}(\hat{c}^{\dagger}_{i\sigma}\hat{c}_{j\sigma} + hc) + U\sum_i \hat{n}_{i\uparrow}\hat{n}_{i\downarrow}, \tag{2.5}$$

where $\langle ij\rangle$ denotes summation over nearest neighbour sites. The equation (2.5) does not account for multi-band effects and orbital degeneracy which are not included within the scope of this work. The Hilbert space needed by the Hubbard Hamiltonian is 4^L dimensional, since any site j can be either empty $|0\rangle_j$, singly occupied with an electron having up-spin, $|\uparrow\rangle_j$, singly occupied with an electron having down-spin, $|\downarrow\rangle_j$ or doubly occupied, $|\uparrow\downarrow\rangle_j$. The approximation leading to this model was justified by Hubbard for $3d$-transition metals. He estimated the various parameters

[3] $U = \int d\vec{x}\int d\vec{x}'|\phi_i(\vec{x})|^2\frac{1}{|\vec{x}-\vec{x}'|}|\phi_i(\vec{x}')|^2 > 0$

and came up with $U \approx 10eV$, $V \approx 2 - 3eV$, and $J_{ij} \approx 1/40eV$ [21]. However, other terms may be important depending on the system and/or the subject of interest. A very good discussion on the importance of all the terms included in the Hubbard model and of those neglected can be found in reference [6].

Apart from the Hubbard model, there are several other important model Hamiltonians which approximate real quantum systems and we shall briefly outline some of them here. We assume single orbital per site throughout the course of our description.

The inclusion of direct terms between nearest neighbours within the Hubbard Hamiltonian of the equation (2.5) defines the **extended Hubbard model**;

$$\hat{H} = \hat{H}_U + V \sum_{\langle ij \rangle} \sum_{\sigma\sigma'} \hat{n}_{i\sigma} \hat{n}_{j\sigma'}. \tag{2.6}$$

Also, it is not unusual to have a fermion model where the spins of all the electrons are forced to be polarized in one direction so that by the Pauli principle they can not share the same site. However, these electrons can interact when sitting at nearest neighbouring sites via Coulomb interaction, V. The Hamiltonian that describes such a model is

$$\hat{H} = -t \sum_{\langle ij \rangle} (\hat{c}_i^\dagger \hat{c}_j + hc) + V \sum_{\langle ij \rangle} \hat{n}_i \hat{n}_j, \tag{2.7}$$

and it is known as the spinless fermion Hamiltonian for the **t-V model**. This has been used for investigating problems related to Wigner crystallization [6].

In order to describe the behaviour of magnetic impurities such as Mn, Fe and Co dilutely inserted into non-magnetic metals such as Cu, Ag and Au, the **Anderson model** [49] is usually employed. Here, the Coulomb interaction within the local d or f shells of the magnetic impurities is the essential ingredient. Its relative strength compared to the hybridization strength with the itinerant electrons of the host (i.e. the virtual-bound-state broadening) is responsible for the existence of local magnetic

moments. The Hamiltonian describing the Anderson model is given by

$$\hat{H} = \sum_{k\sigma} \varepsilon_{k\sigma} \hat{c}^{\dagger}_{k\sigma} \hat{c}_{k\sigma} + \sum_{k\sigma} (V_{kd} \hat{c}^{\dagger}_{k\sigma} \hat{d}_{\sigma} + hc) + \varepsilon_d \sum_{\sigma} \hat{d}^{\dagger}_{\sigma} \hat{d}_{\sigma} + U \hat{d}^{\dagger}_{\uparrow} \hat{d}_{\uparrow} \hat{d}^{\dagger}_{\downarrow} \hat{d}_{i\downarrow}, \tag{2.8}$$

where $\hat{c}_{k\sigma}(\hat{d}_{\sigma})$ is the annihilation operator for the conduction (localized) electrons of the host (the impurity), $\varepsilon_{k\sigma}$ represents the energy of a conduction electron with wave-vector k and spin σ and ε_d is the atomic energy of the localized electrons. The degeneracy of the d or f shells is usually neglected. When two electrons occupy the localized orbitals, a Coulomb repulsion U acts between them. Finally, V_{kd} is the matrix elements describing the mixing between the localized orbitals and the conducting electrons.

The study of the Anderson Hamiltonian can be approached by using perturbative methods. In the limit where V_{kd} is very small compared to U and ε_d, a second order perturbation expansion in the exchange interaction leads to the so-called **s-d model** Hamiltonian, which is usually used to describe the Kondo effect [50, 51]. Within this model, the magnetic impurities are replaced by localized spins interacting with the conduction electrons through an exchange term. The s-d Hamiltonian can be written as

$$\hat{H}_{sd} = \sum_{k\sigma} \varepsilon_{k\sigma} \hat{c}^{\dagger}_{k\sigma} \hat{c}_{k\sigma} + 2J \hat{\mathbf{S}} \cdot \hat{\mathbf{s}}, \tag{2.9}$$

where $\hat{\mathbf{S}} = \sum_{\sigma\sigma'} \hat{d}^{\dagger}_{\sigma} \tau_{\sigma\sigma'} \hat{d}_{\sigma'}$ denotes the spin of the electron on the impurity d-state, $\hat{\mathbf{s}} = \frac{1}{2} \sum_{kk'\sigma\sigma'} \hat{c}^{\dagger}_{k\sigma} \tau_{\sigma\sigma'} \hat{c}_{k'\sigma'}$ is the spin density of the itinerant electron band with τ being Pauli spin matrices. The interaction strength J is a function of the strength of the Coulomb interaction between the localized electrons, the atomic energy of the localized orbital, the energy of the conduction electrons and the hybridization between the impurity and the itinerant bands [50].

Magnetic correlations are often described by models of localized quantum spins, either in chains or, more generally, in higher-dimensional quantum spin lattices [48].

This is achieved by freezing the charge degrees of freedom and only allowing spin excitations to remain. A simple model used in the description of lattice spin systems is

$$\hat{H} = -\sum_{\langle i,j \rangle} (J_z \hat{S}_i^z \hat{S}_j^z + J_y \hat{S}_i^y \hat{S}_j^y + J_x \hat{S}_i^x \hat{S}_j^x), \tag{2.10}$$

where J_x, J_y and J_z are the components of the exchange coupling constant that defines the interaction between localized moments on atoms i and j. $\hat{S}_i^x$, $\hat{S}_i^y$ and $\hat{S}_i^z$ represent the components of the quantum mechanical spin vector, $\hat{\mathbf{S}}_i$ of the i-th atom and obeys the following commutation rule

$$[\hat{S}_j^x, \hat{S}_k^y] = i\delta_{jk}\epsilon^{xyz}\hat{S}_k^z, \tag{2.11}$$

typical of the quantum mechanical spins commutator algebra, $|\mathbf{S}| = S$. ϵ^{xyz} is the Levi-Civita tensor[4]. S may be either an integer or a half-integer. For example, $S = 1/2$ for a single electron while the total magnetic moment of electrons bound to an atom may be much larger.

It is possible to consider various limits of the equation (2.10) by varying its exchange parameters. A short overview of some of these limits, their corresponding Hamiltonian and model name is given in Table 2.1. These models are known to provide a good description of magnetic insulators like EuO or K_2CuF_4.

For the purpose of the research carried out in this thesis, we will consider only the Hubbard (Part I of this thesis) and Heisenberg (Part II of this thesis) models. Therefore in the next section we will discuss the Hubbard model in some details and we will introduce some of its most important features and common approximations.

[4] ϵ^{xyz} is defined by

$$\epsilon^{xyz} = \begin{cases} +1 & \text{if } (x,y,z) \text{ is } (1,2,3), (3,1,2), \text{ or } (2,3,1); \\ -1 & \text{if } (x,y,z) \text{ is } (1,3,2), (3,2,1), \text{ or } (2,1,3); \\ 0 & \text{otherwise: } x = y \text{ or } y = z \text{ or } z = x. \end{cases}$$

Limit	Hamiltonian	Model Name
$J_x = J_y = J_{xy}$	$\hat{H}_{xxz} = -J_{xy}\sum_{\langle i,j\rangle}(\hat{S}_i^y\hat{S}_j^y + \hat{S}_i^x\hat{S}_j^x) - J_z\sum_{\langle i,j\rangle}\hat{S}_i^z\hat{S}_j^z$	**XXZ model**
$J_x = J_y = J_{xy} >> J_z$	$\hat{H}_{xy} = -J_{xy}\sum_{\langle i,j\rangle}(\hat{S}_i^y\hat{S}_j^y + \hat{S}_i^x\hat{S}_j^x)$	**XY model**
$J_z >> J_y, J_x$	$\hat{H}_I = -J_z\sum_{\langle i,j\rangle}\hat{S}_i^z\hat{S}_j^z$	**Ising model**
$J_x = J_y = J_z = J$	$\hat{H}_H = -J\sum_{\langle i,j\rangle}\hat{\mathbf{S}}_i\hat{\mathbf{S}}_j$	**3D Heisenberg model**

Table 2.1: Short summary of the different limits of the equation (2.10). $\langle i,j\rangle$ denotes summation over neighbouring sites.

2.2 The Hubbard model

The Hubbard model plays a crucial role in the field of strongly correlated electron systems because it offers the chance of achieving qualitative insights into how the interactions between electrons can give rise to insulating, magnetic, and even novel superconducting phases in a solid. It was introduced independently by Hubbard [21], Gutzwiller [20] and Kanamori [22] as a model to include both the localized and band-like behaviour. It was originally devised to describe correlation effects for electrons in transition metal monoxides like FeO, NiO and CoO. These compounds are well-known antiferromagnetic insulators, but when treated by mean field methods they are predicted to be metallic.

Ever since its introduction, the Hubbard model has been adopted as a prototype for many systems involving strongly correlated electrons. In its most elementary form, the single orbital case, the Hubbard model could be taken to describe materials in which orbital degeneracy has been completely lifted by crystal field. Over the years, such a model has been used to explain and acquire insights into [19]

- the electronic properties of solids with narrow bands,
- the Mott metal-insulator transition (MIT),
- electronic properties of high-T_c superconductors like cuprates.

As written in the equation (2.5), the Hubbard model contains two terms: the first term which is usually referred to as the *kinetic energy term* contains band energy originating from both the kinetic energy and the atomic potential. It typically describes the hopping process of electrons between two nearest neighbour sites with magnitude t. The second term, the *potential energy term*, describes the electrostatic energy of a doubly occupied site (with an interaction strength U). If either t or U is set to zero, the Hubbard model has trivial solutions. However, if neither t nor U vanishes the model displays a variety of complex properties. While t is responsible for the delocalization of electrons, U keeps them apart so that the ratio U/t is the only parameter that determines the magnetic and electrical properties of any system described by the Hubbard model. By adjusting the U/t ratio, one effectively mimics the variation of external parameters like the pressure, the temperature, the material composition, etc.

From the derivation of U,

$$U = \int d\vec{x} \int d\vec{x}' |\phi_i(\vec{x})|^2 \frac{1}{|\vec{x} - \vec{x}'|} |\phi_i(\vec{x}')|^2, \tag{2.12}$$

one immediately realizes that it is always positive, i.e. it describes repulsive interaction between two electrons. However, at the model level, U can also be taken as negative. A negative-U, first of all, can be obtained formally by a canonical transformation which replaces $U > 0$ with $U < 0$ [6]. Secondly, one can always construct an effective Hamiltonian model (similar to the Bardeen-Cooper-Schrieffer - BCS - model Hamiltonian), which describes a net attractive electron-electron interaction due to processes not characterized in detail. This is usually referred to as the attractive Hubbard model (a review of the attractive Hubbard model can be found in reference [52]). Some superconductors like $Ba_{1-x}K_xBiO_3$ are described by the attractive Hubbard model, which is justified on the basis of the second interpretation. In this work, we will deal with the repulsive Hubbard model only ($U > 0$).

2.2.1 Important features of the Hubbard model

The Hubbard Hamiltonian can be solved exactly in two limiting cases:

- **Band-limit** ($U = 0$): In this limit, $\hat{H}_U$ can be exactly diagonalized (See Appendix A). This gives a band structure for which the electrons energy levels disperse in a cosine-like band, as shown in Figure 2.1a. In this case, the electrons do not feel each other (i.e. they are non-interacting) and hence they are delocalized for any value of the band filling. The system is metallic at any fractional filling.

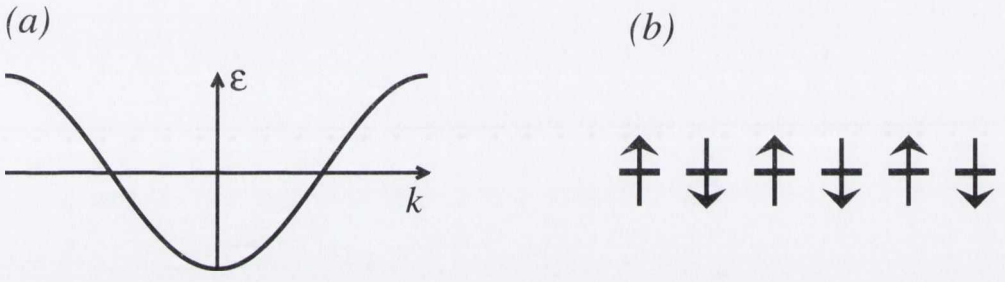

Figure 2.1: Two trivial solutions of the Hubbard model (a) Band-limit: cosine dispersion and always metallic if the band is not completely filled. (b) Atomic-limit: antiferromagnetic Mott-insulator

- **Atomic-limit** ($t = 0$): In the opposite limit, there will be only a collection of independent sites whose eigenvalues are trivial. Due to the energetically expensive price that one pays (by a value of U) for two electrons occupying the same site, the ground state configuration at half-filling ($n = \langle \hat{n} \rangle = 1$) consists of one electron per site. This uniform distribution of electrons, which remains stationary or localized as a result of their repulsive interaction, makes the system behaving as a perfect insulator. This is the so called Mott insulator and is schematically shown in Figure 2.1b. This limit is believed to be responsible for the physical and chemical properties of many $3d$ transition metal oxides such as CoO, antiferromagnetism in MnO, superconductivity in $La_{2-x}Ba_xCuO_4$ and

so on.

Evidently, there would be a MIT in between the above mentioned two limits at half-filling for some value of U/t. In other words, the system will change from being metallic for small U/t to insulating for large U/t. This is considered to be a very interesting feature of the Hubbard model, i.e. electron correlations can drive a metallic system into an insulating phase.

Having solved $\hat{H}_U$ for the two limiting cases, another common limit is the **Strong U limit ($t << U$)**. In this case, the doubly occupied states ($|\uparrow\downarrow\rangle$) are eliminated from the basis set used to represent the wavefunction solving $\hat{H}_U$. Perturbation theory can then be applied to expand the Hubbard model in powers of t/U up to the second order. The resulting model is the so-called t-J model whose Hamiltonian, after a canonical transformation of $\hat{H}_U$, is given by [48]

$$\hat{H}_{\mathrm{tJ}} = -t \sum_{\langle ij \rangle \sigma} (\hat{c}^{\dagger}_{i\sigma} \hat{c}_{j\sigma} + hc) + J \sum_{\langle ij \rangle} (\hat{\mathbf{S}}_i \hat{\mathbf{S}}_j - \frac{\hat{n}_i \hat{n}_j}{4}), \tag{2.13}$$

where $J = 4t^2/U$ and $\hat{\mathbf{S}}_m$ denotes an electron spin operator at site m, ($|\mathbf{S}| = 1/2$). This model is commonly used to explain superconductivity of doped cuprates ($A_{1-x}B_xCO_4$).

At half-filling, since there are no empty sites, the expression (2.13) reduces to

$$\hat{H}^{\frac{1}{2}}_{\mathrm{tJ}} = J \sum_{\langle ij \rangle} (\hat{\mathbf{S}}_i \hat{\mathbf{S}}_j - \frac{1}{4}). \tag{2.14}$$

The equation (2.14) shows that the Hubbard Hamiltonian at half-filling and for strong coupling transforms into a Heisenberg Hamiltonian with an anti-ferromagnetic exchange[5]. This limit reveals that aside from the MIT, an additional feature of the Hubbard model is that the insulating state is magnetic.

[5]Note that the J in equations (2.13) and (2.14) is different from that of the exchange term of equation (2.4). The exchange term has not been included into the Hubbard model whose limit of strong U led to equation (2.14).

Despite the simplicity of the Hubbard Hamiltonian, it is in general difficult to solve (apart from the limits discussed here). This difficulty arises from the fact that the kinetic and potential energies are diagonal in the momentum and real spaces respectively but they do not commute. In order to illustrate the complications arising when solving Hubbard model for arbitrary U/t, in the next section we calculate the spectrum of $\hat{H}_U$ for a two-site lattice.

2.2.2 Two-site Hubbard model

Since each site, n, can be described by four possible states $|n\rangle$ - vacant, singly occupied by either $\uparrow$ or $\downarrow$, or doubly occupied - there will be altogether 4^L multiparticle states, where L is the number of sites. In this basis, $\hat{H}_U$ becomes a $4^L \times 4^L$-matrix. It is possible to reduce the size of the matrix by invoking symmetries specific to the Hamiltonian or the boundary conditions. Examples of the symmetries include the most commonly used ones such as the number of particles and the S^z_{total}. One can also use sophisticated (in terms of implementation) symmetries such as translational invariance, spin inversion, reflections with respect to lattice axes and so on to further beat down the size of the matrix.

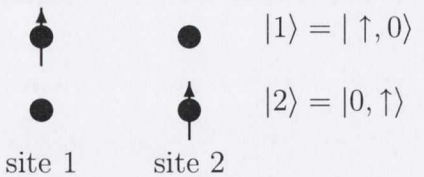

Figure 2.2: Two states retained in a two-site problem with one electron.

Let us start with the two-site one-electron case, a "toy" model for a simplified H_2^+ molecule. Since there is no Coulomb interaction, the second term in $\hat{H}_U$ is zero. We can then eliminate from the basis all the other states of the problem except the ones in which the electron is localized in one of the sites as shown in Figure 2.2. The

wavefunction can be expanded as

$$|\Psi\rangle = c_1|1\rangle + c_2|2\rangle, \tag{2.15}$$

where $|i\rangle$ and the c's represent an electron sitting at i-th site and normalization constants respectively. The Hamiltonian matrix is

$$[\hat{H}_U] = \begin{pmatrix} 0 & -t \\ -t & 0 \end{pmatrix},$$

and the eigenvectors and corresponding eigenvalues of the problem are

$$\begin{aligned} |A\rangle &= \frac{1}{\sqrt{2}}(|1\rangle - |2\rangle) = \frac{1}{\sqrt{2}} \begin{pmatrix} 1 \\ -1 \end{pmatrix}, \qquad \varepsilon_A = +t \\ |B\rangle &= \frac{1}{\sqrt{2}}(|1\rangle + |2\rangle) = \frac{1}{\sqrt{2}} \begin{pmatrix} 1 \\ 1 \end{pmatrix}, \qquad \varepsilon_B = -t. \end{aligned} \tag{2.16}$$

$|A\rangle$ and $|B\rangle$ are called the anti-bonding and bonding states respectively. Note that the bonding state is the ground state of the problem (here t is taken positive).

Let us now consider the case of two electrons, i.e. the neutral H_2 molecule. If we restrict our Hilbert space to the case $N_\uparrow = 1$ and $N_\downarrow = 1$ (singlet state i.e. $S^z = 0$), the wavefunction can be constructed as a linear combination of 4 states only (see Figure 2.3). Here $|0\rangle$ is the vacuum state and "$\cdot$" indicate that the particular site (either 1 or 2) is empty. The Hamiltonian matrix takes the form

$$[\hat{H}_U] = \begin{pmatrix} 0 & 0 & -t & -t \\ 0 & 0 & -t & -t \\ -t & -t & U & 0 \\ -t & -t & 0 & U \end{pmatrix},$$

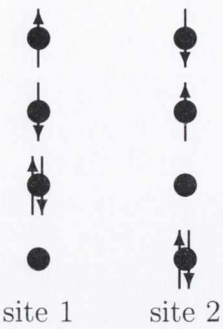

$$|1\rangle = |\uparrow,\downarrow\rangle = \hat{c}^{\dagger}_{2\downarrow}\hat{c}^{\dagger}_{1\uparrow}|0\rangle$$
$$|2\rangle = |\downarrow,\uparrow\rangle = \hat{c}^{\dagger}_{2\uparrow}\hat{c}^{\dagger}_{1\downarrow}|0\rangle$$
$$|3\rangle = |\uparrow\downarrow,\cdot\rangle = \hat{c}^{\dagger}_{1\downarrow}\hat{c}^{\dagger}_{1\uparrow}|0\rangle$$
$$|4\rangle = |\cdot,\uparrow\downarrow\rangle = \hat{c}^{\dagger}_{2\downarrow}\hat{c}^{\dagger}_{2\uparrow}|0\rangle$$

Figure 2.3: Four states retained in a two-site problem with two electrons.

which can be easily diagonalized. The eigenvalues and corresponding eigenvectors are

$$\begin{aligned}
\varepsilon_1 &= \frac{U}{2} - \frac{\sqrt{U^2+16t^2}}{2}, & |\Psi_1\rangle &= \{|1\rangle + |2\rangle\}\cos\theta + \{|3\rangle + |4\rangle\}\sin\theta \\
\varepsilon_2 &= \frac{U}{2} + \frac{\sqrt{U^2+16t^2}}{2}, & |\Psi_2\rangle &= -\{|1\rangle + |2\rangle\}\sin\theta + \{|3\rangle + |4\rangle\}\cos\theta \\
\varepsilon_3 &= 0, & |\Psi_3\rangle &= \frac{1}{\sqrt{2}}(|1\rangle - |2\rangle) \\
\varepsilon_4 &= U, & |\Psi_4\rangle &= \frac{1}{\sqrt{2}}(|3\rangle - |4\rangle), \\
\text{where} & & \tan\theta &= \frac{4t}{U+\sqrt{U^2+16t^2}}.
\end{aligned} \tag{2.17}$$

The ground state energy is therefore the one given by ε_1. Up till this point we have made use of the symmetries of the *Hamiltonian* itself to reduce the dimension of the matrix to be diagonalized i.e. conservation of S^z (equivalent to $[S^z, H_U] = 0$) reduces the matrix to a 4×4 matrix. We note that it is possible to use spatial symmetries by defining a new set of basis in terms of those written in equation (2.17) so that the 4×4 matrix can be further reduced to a 3×3 matrix which can then be manually diagonalized. We refer interested reader to reference [53] where this "toy" is dealt with.

Here we have solved the 4×4 Hubbard Hamiltonian by direct diagonalization. For larger systems (more sites), the Hilbert space associated to $\hat{H}_U$ grows very quickly. In general, the implementation of the Hubbard model involves creating many-body

wave-functions, represented by $|\Psi_\kappa\rangle$, which are formed as a product of creation operators:

$$|\Psi_\kappa\rangle = (\Pi_i^N \hat{c}_{i\sigma}^\dagger)|0\rangle, \tag{2.18}$$

where κ is the dimension of the Hilbert space. The $\hat{H}_U$ matrix elements can then be written as

$$H_{ij} = \langle\Psi_i|\hat{H}_U|\Psi_j\rangle. \tag{2.19}$$

For a L-site problem with $N_\uparrow$ and $N_\downarrow$ electrons, κ is given by

$$\kappa = \binom{L}{N_\uparrow} \cdot \binom{L}{N_\downarrow}, \quad \text{where,} \quad \binom{m}{n} = \frac{m!}{n!(m-n)!}. \tag{2.20}$$

In Table 2.2, we present the dimension of the Hilbert space (the number of basis functions one should use to expand $\hat{H}_U$) for a L-site system at half-filling. This is the filling for which the Hilbert space is the largest. In order to generate the table, we have only used symmetries associated to the number of electrons and that for which $S^z = 0$. The rapid growth of the Hilbert space as L and N increase makes the solution of $\hat{H}_U$ by exact diagonalization impossible. Of course, making use of other symmetries can only reduce the dimension by insignificant fraction. As a result, reasonable approximations are often employed to study the model. The most widely used approximation that exists is the mean field one.

2.2.3 Mean field approximation

The mean field approximation (MFA) assumes that the fluctuations of the site occupation, $n_{i\sigma}$, about its mean value are small and thus can be neglected. This makes the result not as accurate as that obtained by direct diagonalization but it has the advantage of giving rough estimates of average quantities. Within the MFA, the

L	$N_\uparrow$	$N_\downarrow$	Hilbert Space dimension
2	1	1	4
4	2	2	36
6	3	3	400
8	4	4	4,900
10	5	5	63,504
12	6	6	853,776
14	7	7	11,778,624
16	8	8	165,636,900
18	9	9	2,363,904,400
20	10	10	34,134,779,536

Table 2.2: Hilbert space dimension of the Hubbard model with L sites and $N_\uparrow$ and $N_\downarrow$ electrons.

second part of $\hat{H}_U$ can be rewritten by using the expansion

$$\hat{n}_{i\sigma} = \langle \hat{n}_{i\sigma} \rangle + (\hat{n}_{i\sigma} - \langle \hat{n}_{i\sigma} \rangle), \tag{2.21}$$

where $\langle \hat{n}_{i\sigma} \rangle$ is the expectation value of $\hat{n}_{i\sigma}$ so that

$$\begin{aligned} \hat{n}_{i\uparrow}\hat{n}_{i\downarrow} =& \hat{n}_{i\uparrow}\langle \hat{n}_{i\downarrow} \rangle + \langle \hat{n}_{i\uparrow} \rangle \hat{n}_{i\downarrow} - \langle \hat{n}_{i\uparrow} \rangle \langle \hat{n}_{i\downarrow} \rangle \\ &+ (\hat{n}_{i\uparrow} - \langle \hat{n}_{i\uparrow} \rangle)(\hat{n}_{i\downarrow} - \langle \hat{n}_{i\downarrow} \rangle). \end{aligned} \tag{2.22}$$

If the last term of equation (2.22) is neglected since it is of second order in the particle density fluctuations, $(\hat{n}_{i\sigma} - \langle \hat{n}_{i\sigma} \rangle)$, then the original Hubbard model can be replaced with the mean field Hamiltonian

$$\hat{H}_U^{MFA} = -t \sum_{\langle ij \rangle \sigma}^{L} (\hat{c}_{i\sigma}^\dagger \hat{c}_{j\sigma} + hc) + U \sum_{i}^{L} (\hat{n}_{i\uparrow}\langle \hat{n}_{i\downarrow} \rangle + \langle \hat{n}_{i\uparrow} \rangle \hat{n}_{i\downarrow} - \langle \hat{n}_{i\uparrow} \rangle \langle \hat{n}_{i\downarrow} \rangle). \tag{2.23}$$

The implication of this approximation is that, instead of considering each electron as interacting individually with all the other electrons, as in the case of original Hubbard model, the interaction can now be viewed as an effective or a 'mean field' one generated by all the electrons combined. The neglected term in equation (2.22)

contains the error of this approximation. Clearly, the mean field Hamiltonian includes only linear terms in the number operator, $\hat{n}_{i\sigma}$, which is much more simpler to diagonalize than the original Hubbard model.

The MFA is known to be a very good approximation in infinite dimensions but its performance is usually not as good for low-dimensional systems. As such, dimensionality plays a crucial role in providing a fully consistent treatment of the Hubbard model. Exact solutions of the Hubbard Hamiltonian are known in the one dimension and for infinite dimensional systems but for two and three dimensions $\hat{H}_U$ has not been solved exactly. Therefore, in next section we highlight theoretical frameworks to describe interacting quantum systems in different dimensions.

2.3 Fermi and Luttinger liquids

As pointed out in the introduction, correlation effects in fermionic systems are due to the Coulomb interaction. There are two basic concepts that are used for describing these interacting systems: the *Fermi liquid* and the *Luttinger liquid* [54]. It is not our intention to explain in details these concepts as that has been done in references [54, 55, 56] but we will briefly mention a few important aspects.

The Fermi liquid is a generalization of the non-interacting many-fermion system (Fermi gas) to its interacting counterpart, whose theoretical description (Fermi liquid theory [8]) is approximate but well understood [56]. The idea can be depicted by a picture of quasi-particles (elementary single-particle excitations) evolving from a Fermi gas on adiabatically switching on the Coulomb interaction. These quasi-particles can be labelled by the same quantum numbers as the excitations in the non-interacting gas and obey Fermi-Dirac statistics. This, therefore, establishes a one-to-one correspondence between such excitations and the "bare" particles ($U = 0$). There are three main effects that the electron-electron interaction brings to the Fermi liquid which modify the non-interacting electron picture: (1) Renormal-

ization of the kinematic parameters of the quasi-particles such as the effective mass (t in the lattice case), and the thermodynamic properties like specific heat and susceptibility; (2) it provides quasi-particles with a finite lifetime which goes to infinity close to the Fermi surface; (3) it induces oscillations in the Fermi liquid, which are called zero sound modes [57].

Despite the remarkable success of Fermi liquid theory in explaining the effects of the Coulomb interaction in an electron gas in high dimensions, the theory breaks down in 1D. From the topological point of view, it is not difficult to see that interaction has more drastic effects in 1D when compared to higher dimensions due to the restricted geometry in 1D (electrons can hardly avoid each other). Any electron that propagates in a 1D wire will push all its neighbours because of electron-electron interaction. In other words, the individual motion of electron is prohibited and only collective excitations are allowed. Even when the interaction between electrons is weak, 1D wires are still classified as strongly correlated due to effective reduced dimensionality which hinders single-particle motion. This is the key difference between one-dimensional and higher-dimensional systems. Also the physical properties of the one-dimensional electron gas are indeed significantly different from those of the free electron gas because of the non-Fermi liquid behaviour. This makes the ground state of the interacting system in 1D different from the free fermion gas. Such a new ground state is often referred to as the Luttinger liquid [10].

A Luttinger liquid is an important metallic phase that is not a Fermi liquid (to be more precise, the Fermi liquid state can only correspond to non-interacting fermions in 1D as any metallic state with interacting fermions must be a Luttinger liquid). Thus, the quasi-particles in this new state of matter are no longer fermionic in nature but are bosonic where the so-called collective excitations dominate. The Luttinger liquid collective excitations behave like the oscillations of a string, which are made up from the motions of the infinitely many small pieces of the string. Importantly, many

of the correlation effects of the Luttinger liquid (the quasi-particle spectrum) can be computed exactly [11, 45] so that it is possible to have direct access to physical properties of interest. Examples of systems where Luttinger liquid theory can be applied include fermionic metals like nanotubes, bosons in optical lattices and also spin chains [12].

2.4 Lieb-Wu equations for homogeneous one-dimensional Hubbard Model

Many properties of one-dimensional structures have been successfully studied through the Hubbard Hamiltonian of the equation (2.5) [16]. The Hamiltonian was exactly solved by Lieb and Wu using the Bethe Ansatz (BA). We now present an analytic solution for the Hubbard model, valid in the limit of infinite, homogeneous 1D systems. Let us consider the homogeneous form of the Hubbard Hamiltonian, $\hat{H}_U$, containing L lattice sites and N electrons. The Hamiltonian commutes with the spin-resolved total number operators:

$$\hat{N}_\sigma \equiv \sum_i \hat{c}^\dagger_{i\sigma}\hat{c}_{i\sigma} = \sum_i \hat{n}_{i\sigma}; \qquad \sigma = \uparrow, \downarrow \tag{2.24}$$

where $\hat{N} = \hat{N}_\uparrow + \hat{N}_\downarrow$. This implies that the conserved quantities (constants of motion) are the total number of electrons per site, n, (electron concentration or band filling) and the total magnetization per site, m. These are defined as

$$n = \frac{N}{L} \equiv \frac{1}{L}\sum_{i,\sigma}\langle \hat{c}^\dagger_{i\sigma}\hat{c}_{i\sigma}\rangle = n_\uparrow + n_\downarrow, \qquad m \equiv \frac{1}{L}\sum_{i,\sigma}\sigma\langle \hat{c}^\dagger_{i\sigma}\hat{c}_{i\sigma}\rangle = n_\uparrow - n_\downarrow. \tag{2.25}$$

$0 \leq n \leq 1$, $0 \leq m \leq n$ with $n_\uparrow = N_\uparrow/L$ and $n_\downarrow = N_\downarrow/L$. The electron concentration is related to that of the hole concentration, p, through relation $p = 1 - n$ so that

the limiting cases $n = 0$ and $n = 1$ corresponds to empty and half-filled bands respectively.

An elegant and quite general method for solving one-dimensional problems with correlation is based on the BA [58]. It was introduced by Hans Bethe who first used it to solve the Heisenberg model. This method relies on writing the exact wavefunction of the interacting system under study and then solving the associated Schrödinger equation. The idea is to make a plane-wave ansatz of the form

$$\Psi_N = \sum_P a(P) \exp\{i \sum_k \lambda_{P_k} x_k\}, \tag{2.26}$$

where the sum is over all permutations of the momenta $\{\lambda_k\}_{k=1,...,N}$. Here, $x_1, ..., x_N$ are the positions of the N particles in the system. The equation (2.26) is weighted by a prefactor $a(P)$ which depends on the permutation. By applying periodic boundary conditions to the wavefunction then one obtains the allowed quantum numbers as a set of coupled equations referred to as the Bethe equations. A comprehensive review on this subject can be found in reference [59]. The BA has been employed to tackle problems like the one-dimensional Bose gas [60], the Heisenberg XXZ magnet [61] and the Heisenberg XYZ chain [62].

In 1968, $\hat{H}_U$ was solved exactly in 1D by using this ansatz. The solution is expressed via the following Lieb-Wu equations [45]:

$$\begin{aligned} e^{ik_j L} &= \prod_{\beta=1}^{N_\downarrow} \frac{i \sin k_j - i\Lambda_\beta - U/4}{i \sin k_j - i\Lambda_\beta + U/4}, \quad j = 1, 2, ..., N \\ \prod_{j=1}^{N} \frac{i \sin k_j - i\Lambda_\alpha - U/4}{i \sin k_j - i\Lambda_\alpha + U/4} &= -\prod_{\beta=1}^{N_\downarrow} \frac{-i\Lambda_\beta + i\Lambda_\alpha + U/2}{-i\Lambda_\beta + i\Lambda_\alpha - U/2}, \quad \alpha = 1, 2, ..., N_\downarrow, \end{aligned} \tag{2.27}$$

where the two sets of variables $\{k_j\}$ and $\{\Lambda_\alpha\}$ are quantum numbers typically referred to as quasi-momentum and spin rapidities respectively [19]. They are calculated from the Lieb-Wu equations. By taking the logarithm of these equations one can derive

the following transcendental equations [45, 63, 64]:

$$\begin{aligned} Lk_j &= 2\pi I_j + 2\sum_{\beta=1}^{N_\downarrow} \tan^{-1}\left(\frac{\Lambda_\beta - \sin k_j}{U/4}\right) \\ 2\sum_{j=1}^{N} \tan^{-1}\left(\frac{\Lambda_\alpha - \sin k_j}{U/4}\right) &= 2\pi J_\alpha + 2\sum_{\beta=1}^{N_\downarrow} \tan^{-1}\left(\frac{\Lambda_\alpha - \Lambda_\beta}{U/2}\right), \end{aligned} \tag{2.28}$$

where $\{I_j\}$ and $\{J_\alpha\}$ are quantum numbers, which can be either integers or half-integers. The ground state energy is given by [45]

$$E = -2t\sum_{j=1}^{N} \cos k_j. \tag{2.29}$$

In the limit where $L \to \infty$ so that $n_\uparrow = N_\uparrow/L$ and $n_\downarrow = N_\downarrow/L$ are constant, it has been shown that the energy per site (energy density) of the system, e, for the repulsive case can be written as [65]

$$e = -2t\int_{-Q}^{Q} dk \cos k\rho(k), \tag{2.30}$$

for $n_\uparrow \geq n_\downarrow$. The function $\rho(k)$ is determined from the Fredholm coupled integral equations:

$$\begin{aligned} \rho(k) &= \frac{1}{2\pi} + \cos k \int_{-B}^{B} d\lambda \sigma(\lambda) K_1(\sin k - \lambda), \\ \sigma(\lambda) &= \int_{-Q}^{Q} dk \rho(k) K_1(\sin k - \lambda) - \int_{-B}^{B} d\lambda' \sigma(\lambda') K_2(\lambda - \lambda'), \end{aligned} \tag{2.31}$$

where

$$\begin{aligned} K_1(\sin k - \lambda) &\equiv \frac{1}{2\pi}\left[\frac{8U}{U^2 + 16(\sin k - \lambda)^2}\right], \\ K_2(\lambda - \lambda') &\equiv \frac{1}{2\pi}\left[\frac{4U}{U^2 + 4(\lambda - \lambda')^2}\right], \end{aligned} \tag{2.32}$$

with normalization conditions determining Q and B,

$$\begin{aligned}\int_{-Q}^{Q}\rho(k)dk =& N/L = n = n_\uparrow + n_\downarrow,\\ \int_{-B}^{B}\sigma(\lambda)d\lambda =& N_\downarrow/L = n_\downarrow = \frac{n-m}{2}.\end{aligned} \tag{2.33}$$

The parameters Q and B generally depend on n, m, U and t.

It is useful to know that by substituting $\rho(k)$ into (2.33), one can write

$$\int_{\pi}^{\pi} dk \cos k f(\sin k) = 2\int_{0}^{\pi} \cos k f(\sin k) = 0. \tag{2.34}$$

There $Q = \pi$ implies that the band is half-filled

$$\frac{N}{L} = \int_{\pi}^{\pi} dk\rho(k) = 1. \tag{2.35}$$

Also when $B = \infty$, by combining (2.31) and (2.33), one obtains

$$\int_{-\infty}^{\infty}\sigma(\lambda)d\lambda = \frac{1}{2}\int_{-Q}^{Q}\rho(k)dk = \frac{n}{2}, \tag{2.36}$$

i.e. the important result that the magnetization, m, of the ground state is zero.

At $Q = \pi$ and $B = \infty$, the coupled integral equations can be solved analytically to obtain the ground state energy density for the half-filled Hubbard chain as

$$e = -4t\int_{0}^{\infty} dx\frac{J_0(x)J_1(x)}{x[1+\exp(xU/2t)]}, \tag{2.37}$$

where J_0 and J_1 are the zero and the first order Bessel functions respectively. Lieb and Wu [45] indeed showed analytically that a system will always be in the insulating phase for $U > 0$ at half-filling in one dimension.

The BA method only allows us access to properties of the *homogeneous* Hubbard model. An addition of an extra term to the homogeneous model will break its in-

tegrability and thereby restricts the capability of BA techniques to describe many physically relevant quantum systems. Nevertheless, the integrability of the homogeneous case provides benchmarks for the development of approximate and numerical methods. Such numerically approximate method is the LDFT. In the next section, we will introduce the basic formalism of DFT, namely the Hohenberg-Kohn theorem and Kohn-Sham scheme, plus its approximate energy functionals. An extensive review of *ab initio* DFT can be found in reference [66].

2.5 Density functional theory

Most of the calculation methods in solid state physics and quantum chemistry aim at solving the time-independent, non-relativistic Schrödinger equation

$$\hat{H}\Phi_i(\vec{x}_1, \vec{x}_2, ..., \vec{x}_N, \vec{R}_1, \vec{R}_2, ..., \vec{R}_M) = E_i\Phi_i(\vec{x}_1, \vec{x}_2, ..., \vec{x}_N, \vec{R}_1, \vec{R}_2, ..., \vec{R}_M). \quad (2.38)$$

Here $\hat{H}$ is the Hamiltonian for a system consisting of M nuclei and N electrons which can be written as

$$\hat{H} = -\frac{1}{2}\sum_{i=1}^{N}\vec{\nabla}_i^2 - \frac{1}{2}\sum_{A=1}^{M}\frac{1}{M_A}\vec{\nabla}_A^2 - \sum_{i=1}^{N}\sum_{A=1}^{M}\frac{Z_A}{\vec{x}_{iA}} + \sum_{i=1}^{N}\sum_{j>i}^{N}\frac{1}{\vec{x}_{ij}} + \sum_{A=1}^{M}\sum_{B>A}^{M}\frac{Z_A Z_B}{\vec{R}_{AB}}, \quad (2.39)$$

and where the atomic units are used i.e. $\hbar = m_e = e = 4\pi\varepsilon_0 = 1$. A and B run over the M nuclei, while i and j over the N electrons in the system. The first and the second term describe the kinetic energy of the electrons and the nuclei respectively; the last three terms represent the attractive electrostatic interaction between the nuclei and the electrons, the repulsive potential due to electron-electron interaction and the repulsive potential due to the nucleus-nucleus interactions.

By using the Born-Oppenheimer approximation, the electrons can be considered to be moving in the field of static nuclei. The inertia of electrons is considered to

be negligible in comparison to that of the nuclei with the result that their nuclear kinetic energy is negligible and their potential energy is just a constant. Thus, the electronic part of the Hamiltonian can be written as

$$\begin{aligned}\hat{\mathcal{H}} &= -\frac{1}{2}\sum_{i=1}^{N}\vec{\nabla}_i^2 + \sum_{i=1}^{N}\sum_{j>i}^{N}\frac{1}{\vec{x}_{ij}} - \sum_{i=1}^{N}\sum_{A=1}^{M}\frac{Z_A}{\vec{x}_{iA}} \\ &= -\frac{1}{2}\sum_{i=1}^{N}\vec{\nabla}_i^2 + \sum_{i=1}^{N}\sum_{j>i}^{N}\frac{1}{\vec{x}_{ij}} + \sum_{i=1}^{N}v(\vec{x}_i) \\ &= \hat{\mathcal{T}} + \hat{\mathcal{U}} + \hat{\mathcal{V}},\end{aligned} \tag{2.40}$$

where the last term is the potential energy operator of the electrons in the external potential generated by the nuclei $v(\vec{x})$. The solution of the Schrödinger equation,

$$\hat{\mathcal{H}}|\Psi\rangle = E|\Psi\rangle, \tag{2.41}$$

gives the electronic many-body wavefunction $\Psi(\{\vec{x}_i\})$, where $\{\vec{x}_i\}$ are the electron coordinates and their spins, and electronic energy E.

In principle, equation (2.41) can be solved by expanding the wavefunction in a basis of Slater determinants, therefore converting it to a problem of diagonalizing matrices. The drawback of this approach is that the dimension of the Slater basis grows with the number of electrons as $N!$ thereby the scheme can only be used for very few electron systems. In addition, the true many-body wavefunction may not be representable as a single Slater determinant.

Before the advent of DFT, the Hartree-Fock approximation (HFA) was the standard approach used by solid state physicists and quantum chemists. The HFA uses a single Slater determinant that minimizes the total energy instead of the many-body wavefunction. However, this method lacks electron correlations, although it captures correctly the exchange. It describes electrons as independent of each other, interacting only via an effective field. This has made HFA to inaccurately describe metals as

insulators or semiconductors. A number of systematic improvements on this method have been developed over the years such as perturbation theory, or the configuration interaction (CI) scheme [67], but these are computationally expensive just like the ED, thereby only applicable to systems with a relatively small number of electrons.

Another route, which is considered to be the most successful approach in solving the Schrödinger equation for the many-body problem, is DFT. The main idea behind DFT can be briefly described as follows: since the Hamiltonian is parametrized by the external potential $v(\vec{x})$, the corresponding energy and many-body electronic wavefunction that satisfies the Schrödinger equation (2.41), can be considered as functionals of this external potential so that $\Psi = \Psi[v]$ and $E = E[v]$. The most important innovation of DFT is the replacement of the many-body wavefunction by the electronic density $n(\vec{x})$ of the system. This is

$$n(\vec{x}) = N \int ... \int |\Psi(\vec{x}, \vec{x}_1, \vec{x}_2, ..., \vec{x}_N)|^2 d\vec{x}_2 ... \vec{x}_N, \tag{2.42}$$

in which the density operator $\hat{n}(\vec{x})$ can be defined as

$$\hat{n}(\vec{x}) = \sum_{i}^{N} \delta(\vec{x} - \vec{x}_i). \tag{2.43}$$

By using the expression (2.43), the potential energy due to the external potential can be written as

$$\mathcal{V} = \langle \Psi | \hat{\mathcal{V}} | \Psi \rangle = \langle \Psi | \int \hat{n}(\vec{x}) v(\vec{x}) d\vec{x} | \Psi \rangle = \int n(\vec{x}) v(\vec{x}) d\vec{x}. \tag{2.44}$$

The Hohenberg-Kohn theorem, presented in the next section, states that there is a one to one correspondence between the external potential $v(\vec{x})$ and the ground state density $n(\vec{x})$. These two quantities can be considered as conjugate variables via a

Legendre transformation,

$$\frac{\delta E_0[v]}{\delta v(\vec{x})} = \left\langle \frac{\delta \Psi_0[v]}{\delta v(\vec{x})} | \hat{\mathcal{H}}_v | \Psi_0[v] \right\rangle + \left\langle \Psi_0[v] | \hat{\mathcal{H}}_v | \frac{\delta \Psi_0[v]}{\delta v(\vec{x})} \right\rangle + \left\langle \Psi_0[v] | \frac{\delta \hat{\mathcal{H}}_v}{\delta v(\vec{x})} | \Psi_0[v] \right\rangle$$
$$= E_0[v] \frac{\delta}{\delta v(\vec{x})} \langle \Psi_0[v] | \Psi_0[v] \rangle + \langle \Psi_0[v] | \hat{n}(\vec{x}) | \Psi_0[v] \rangle = n[v](\vec{x}), \tag{2.45}$$

where the wavefunction $\Psi_0[v]$ is normalized and the ground state energy of the Hamiltonian is E_0. The density can therefore be used as the only fundamental quantity by defining a Legendre transform

$$\mathcal{F}[n] = E_0[n] - \int n(\vec{x}) v(\vec{x}) d\vec{x} = \langle \Psi_0[v] | \hat{T} + \hat{\mathcal{U}} | \Psi_0[v] \rangle, \tag{2.46}$$

where $v(\vec{x})$ is a functional of $n(\vec{x})$. The proof that this functional is unique relies on the one-to-one mapping between the external potential and the ground state density. The functional $\mathcal{F}[n]$ is defined for the so-called v-representable densities, i.e., ground state densities associated to a Hamiltonian with external potential v. By differentiating this functional with respect to the electron density, one immediately obtains

$$\frac{\delta \mathcal{F}[n]}{\delta n(\vec{x})} = \int \frac{\delta E_0[v]}{\delta v(\vec{x}')} \frac{\delta v(\vec{x}')}{\delta n(\vec{x})} d\vec{x}' - \int n(\vec{x}') \frac{\delta v(\vec{x}')}{\delta n(\vec{x}')} d\vec{x}' - v(\vec{x}) = -v(\vec{x}). \tag{2.47}$$

2.5.1 Hohenberg-Kohn theorem

Central to DFT are the two theorems derived and proved by Hohenberg and Kohn (HK) in 1964 [31]. The first theorem establishes that the electron density n of a non-degenerate ground state uniquely determines the external potential $v(\vec{x})$ (up to an arbitrary constant), which acts over the many electron system. In other words, the electron density $n(\vec{x})$ determines the Hamiltonian operator and thus all the electronic properties of the ground state of the system. The implication of this first theorem is

that the total energy of a Coulombic many-electron system in an external potential can be written as

$$\begin{aligned} E[n] =& \langle \Psi[n] | \hat{\mathcal{H}} | \Psi[n] \rangle = \langle \Psi[n] | \hat{\mathcal{T}} + \hat{\mathcal{U}} + \hat{\mathcal{V}} | \Psi[n] \rangle \\ =& \langle \Psi[n] | \hat{\mathcal{T}} + \hat{\mathcal{U}} | \Psi[n] \rangle + \langle \Psi[n] | \hat{\mathcal{V}} | \Psi[n] \rangle = \mathcal{F}[n] + \int n(\vec{x}) v(\vec{x}) d\vec{x}, \end{aligned} \tag{2.48}$$

where the functional $\mathcal{F}[n]$ is independent of the external potential and thus is universal. This means that if one knows its exact form, any many-electron problem will be solved.

The second HK theorem states that the electron density which minimizes the energy functional is the exact ground state electron density, i.e.,

$$E_0[n] = \min_n \{ \mathcal{F}[n] + \int n(\vec{x}) v(\vec{x}) d\vec{x} \}, \tag{2.49}$$

where $E_0[n]$ is the ground state energy for the system in an external potential $v(\vec{x})$. This second theorem can be proved by variational principles. If the functional derivative of $\mathcal{F}[n] + \int n(\vec{x}) v(\vec{x}) d\vec{x}$ with respect to $n(\vec{x})$ exists and obeys the conservation of particle constraint, the theorem will require that the ground state density satisfies the Euler-Lagrange equations:

$$0 = \frac{\delta}{\delta n(\vec{x})} \left\{ \mathcal{F}[n] + \int n(\vec{x}) v(\vec{x}) d\vec{x} - \mu \left(\int d\vec{x} n(\vec{x}) - N \right) \right\}, \tag{2.50}$$

where the Lagrange multiplier μ ensures particle conservation, i.e. $\int d\vec{x} n(\vec{x}) = N$.

DFT reduces exactly the problem of an N interacting electron system to the determination of a 3-dimensional function $n(\vec{x})$ which minimizes a functional $E_0[n]$. However the exact form of $\mathcal{F}[n]$ is unknown. Therefore, the major challenge of DFT is to construct approximate forms of $\mathcal{F}[n]$.

It is instructive to note that a definition of functional was found, in parallel, by Levy [68] and Lieb [69] and it is usually known as the *Levy constrained-search formu-*

lation or *Levy-Lieb constrained-search formulation.* Here a constrained minimization is performed over the all the wavefunction which yield the trial density. This minimization is rarely used for practical implementation of DFT. The most commonly used scheme is one proposed again by Kohn, this time in collaboration with Sham [32].

2.5.2 The Kohn-Sham scheme

The idea is that of mapping a system of interacting electrons onto an auxiliary system of non-interacting ones with the same ground state electron density $n(\vec{x})$ and ground state energy E_0. The mapping forms the starting point for all modern day practical implementations of DFT.

Kohn and Sham (KS) introduced an auxiliary single-particle Hamiltonian, $\hat{\mathcal{H}}_s$, written in terms of an effective potential operator, $\hat{\mathcal{V}}_s$,

$$\hat{\mathcal{H}}_s = \hat{\mathcal{T}}_s + \hat{\mathcal{V}}_s, \tag{2.51}$$

whose ground state density is the same to that associated to the interacting Hamiltonian. If the effective potential, $v_s(\vec{x})$, exists, then its uniqueness is guaranteed by the first HK theorem. Thus, an energy functional, E_s similar to the one of the equation (2.48) and its Legendre transform, $\mathcal{F}_s$ can be written as

$$\begin{aligned} E_s[v_s] =& \langle \Psi_s[v_s] | \hat{\mathcal{T}}_s + \hat{\mathcal{V}}_s | \Psi_s[v_s] \rangle \\ \mathcal{F}_s[n] =& E_s - \int n(\vec{x}) v_s(\vec{x}) d\vec{x} = \langle \Psi_s[v_s] | \hat{\mathcal{T}}_s | \Psi_s[v_s] \rangle, \end{aligned} \tag{2.52}$$

with the functional derivatives

$$\begin{aligned} \frac{\delta E_s[v_s]}{\delta v_s(\vec{x})} =& n(\vec{x}), \\ \frac{\delta \mathcal{F}_s[n]}{\delta n(\vec{x})} =& - v_s(\vec{x}). \end{aligned} \tag{2.53}$$

The XC energy $E_{xc}[n(\vec{x})]$ can be formally defined by taking the difference between $\mathcal{F}_s[n]$ and $\mathcal{F}[n]$;

$$\begin{aligned}\mathcal{F}[n] - \mathcal{F}_s[n] =& \langle\Psi|\hat{T} + \hat{\mathcal{U}}|\Psi\rangle - \langle\Psi_s|\hat{T}_s|\Psi_s\rangle \\ =& \langle\Psi|\hat{T}|\Psi\rangle - \langle\Psi_s|\hat{T}_s|\Psi_s\rangle + \langle\Psi|\hat{\mathcal{U}}|\Psi\rangle \\ =& E_{xc}[n(\vec{x})] + E_H[n(\vec{x})],\end{aligned} \tag{2.54}$$

where the Hartree term $E_H[n(\vec{x})]$ is the classical Coulomb repulsion of the electron density given as

$$E_H[n(\vec{x})] = \frac{1}{2}\int \frac{n(\vec{x})n(\vec{x'})}{|\vec{x} - \vec{x'}|} d\vec{x}d\vec{x'}. \tag{2.55}$$

By taking the functional derivative of the expression (2.54) with respect to $n(\vec{x})$, the KS effective potential is obtained as

$$v_s(\vec{x}) = v(\vec{x}) + v_{xc}(\vec{x}) + v_H(\vec{x}), \tag{2.56}$$

where

$$\begin{aligned}v_H =& \int \frac{n(\vec{x'})}{|\vec{x} - \vec{x'}|} d\vec{x'} \\ v_{xc} =& \frac{\delta E_{xc} n(\vec{x})}{\delta n(\vec{x})}.\end{aligned} \tag{2.57}$$

Given the fact that the state $|\Psi_s\rangle$ is associated to a non-interacting particle system, it is possible to write it as a single Slater determinant formed by one-particle orbitals, ϕ_i, (the Kohn-Sham orbitals) which satisfy the self-consistent KS equations

$$\left[-\frac{1}{2}\nabla^2 + v_s(\vec{x})\right] \phi_i(\vec{x}) = \varepsilon_i \phi_i(\vec{x}), \tag{2.58}$$

where

$$n(\vec{x}) = \sum_i^N |\phi_i(\vec{x})|^2. \tag{2.59}$$

The states ϕ_i are ordered so that the energies ε_i are non-decreasing. For degenerate

eigenstates, fractional occupations f_i are to be used so that

$$n(\vec{x}) = \sum_{i}^{N} f_i |\phi_i(\vec{x})|^2. \tag{2.60}$$

Within the KS scheme, the XC energy contains several contributions. Firstly, it includes the difference between the true kinetic energy and the one of the non-interacting system calculated via the single-particle KS orbitals. Secondly it includes the error of approximating the many-body interaction with the classical Hartree interaction. Finally, it includes the fact that the true wavefunction may not be a single Slater determinant. Therefore all the many-body effects have now been incorporated into the XC functional. This term of the energy functional must be approximated since all others can be calculated exactly within the KS scheme.

Clearly the interacting problem is reduced to a set of non-interacting Schrödinger-like equations. The formulation of the KS equation is in principle exact. If the exact XC functional is known it is possible to obtain the exact ground state total energy and density of any interacting N-electron systems by solving the KS equations self-consistently. Given the fact that the exact form of XC term is unknown, the major challenge in DFT is therefore deriving suitable approximations for it.

2.5.3 Approximate energy functionals

The *local density approximation* (LDA) is the simplest approximation to E_{xc} and usually the basis of all approximate XC functionals. An homogeneous electron gas, in which electrons move on a positive background charge distribution such that the total ensemble is neutral, is adopted as the reference for this approximation. The XC energy functional of the real interacting system with the local density $n(\vec{x})$ is, at every point in space, replaced by the XC energy of the homogeneous electron gas

with the same density

$$E_{xc}^{LDA}[n] = \int n(\vec{x})\varepsilon_{xc}(n(\vec{x}))d\vec{x}. \tag{2.61}$$

Here, $\varepsilon_{xc}(n(\vec{x}))$ is the XC energy density (per particle) of the homogeneous electron gas. This quantity can be split into the exchange and correlation contributions,

$$\varepsilon_{xc}(n(\vec{x})) = \varepsilon_x(n(\vec{x})) + \varepsilon_c(n(\vec{x})). \tag{2.62}$$

The exchange part, $\varepsilon_x(n(\vec{x}))$, is the exchange energy of an homogeneous electron gas at a particular density and was originally derived by Bloch and Dirac [70]:

$$\varepsilon_x(n(\vec{x})) = -\frac{3}{4}\left(\frac{3n(\vec{x})}{\pi}\right)^{1/3}. \tag{2.63}$$

However no such explicit expression is known for the correlation part, $\varepsilon_c(n(\vec{x}))$. Nevertheless, data from highly accurate numerical methods, such as Quantum Monte-Carlo, for the homogeneous electrons are used to estimate ε_c.

The LDA has been successfully used in describing metallic systems and in general systems where the electron density is rather uniform, but has failed for systems with substantial electron density gradients. The failure of the LDA is also known to be related to its inability to satisfy some exact conditions. For instance, $\varepsilon_c[n(\vec{x})]$ does not scale properly at the high-density limit [71] and it does not display the derivative discontinuity at integer values of the occupation numbers [72].

The first simple extension to the LDA is the *generalized gradient approximation* (GGA). Here the XC functional is written not only as a function of the local density but also of the local gradient of the density:

$$E_{xc}^{GGA}[n] = \int n(\vec{x})\varepsilon_{xc}(n(\vec{x}), |\nabla n(\vec{x})|)d\vec{x}. \tag{2.64}$$

One way to further improve on the GGA functional is that of systematically including higher derivatives of $n(\vec{x})$ like $|\nabla^2 n(\vec{x})|$ or the kinetic energy density ($\tau(\vec{x}) = \frac{1}{2}\sum_i |\nabla\phi_i(\vec{x})|^2$) into the XC functional. This is the so-called *meta-GGAs*. However, the more ingredients one adds to the functional, the more expensive its computational cost becomes.

One major class of materials where the LDA/GGA is either not accurate enough or even fails dramatically is that of strongly correlated compounds like transition metal oxides. Insufficient cancellation of the self-interaction error (SIE) is the prominent reason for this failure. Functionals which attempt to rectify this error are usually referred to as *hybrid functionals*. The SIE originates from the spurious Coulomb interaction of an electron with itself, which is inherent to the LDA/GGA functionals. HF methods, in the unrestricted or spin polarized form, are SIE free and so can be mixed with GGA functional as proposed by Becke [73] (this is the spirit of the hybrid functionals).

Approaches, which use either direct subtraction of the SIE, conventionally called *self-interaction correction* (SIC) [74] or those that mix portions of HF exchange with the local approximation (LDA/GGA) of DFT perform better in describing various properties of insulating solids (where GGA normally fails) and strongly correlated materials like NiO. It is important to note that both methods based on non-local exchange or SIC are computationally demanding and thus their application to the solid state remains rather limited. An alternative scheme that provides good estimates of physical properties for systems where LDA/GGA fails and at the same time is not numerically expensive has been implemented in a localized atomic orbital code for large-scaling is the *atomic*-SIC (ASIC) scheme [75, 76]. It has been used to investigate exchange parameters in strongly correlated materials [77] and its performance is reported in the second part of this thesis.

The LDA+U approach [78, 79, 80] is another scheme employed to study strongly

correlated materials. It is based on the Hubbard model with a U parameter representing the screened electron-electron interaction. This is added to the LDA Hamiltonian and treated in the HFA thus correcting for the SIE. The U parameter is usually fitted in order to reproduce certain properties like the lattice spacing, band gap, etc of the material under consideration. It has proven to give a reasonable description of the electronic and magnetic properties of strongly correlated materials like transition metal and rare-earth oxides.

2.5.4 Spin-polarized DFT

So far, the electrons are assumed to be unpolarized where the total z-component of spin s_z per electron is zero. The generalization of DFT to a system of unpaired electrons has also been developed. Here, both the electron density $n(\vec{x})$ and the spin density $m(\vec{x})$ are the fundamental quantities of the theory. These are defined as

$$n(\vec{x}) = n_\uparrow(\vec{x}) + n_\downarrow(\vec{x}), \tag{2.65}$$

and

$$m(\vec{x}) = n_\uparrow(\vec{x}) - n_\downarrow(\vec{x}). \tag{2.66}$$

The XC functional now becomes different for the two spin species σ (either $\uparrow$ or $\downarrow$), leading to a set of spin-polarized KS equations,

$$\begin{aligned} \left[-\frac{1}{2}\nabla^2 + v_s^\uparrow[n,m](\vec{x})\right]\phi_i^\uparrow &= \varepsilon_i^\uparrow \phi_i^\uparrow \\ \left[-\frac{1}{2}\nabla^2 + v_s^\downarrow[n,m](\vec{x})\right]\phi_i^\downarrow &= \varepsilon_i^\downarrow \phi_i^\downarrow, \end{aligned} \tag{2.67}$$

where $v_{xc}^\sigma[n,m](\vec{x}) := \frac{\delta E_{xc}[n,m]}{\delta n_\sigma}(\vec{x})$ for which in general $v_{xc}^\uparrow[n,m](\vec{x}) \neq v_{xc}^\downarrow[n,m](\vec{x})$. This gives two sets of KS orbitals, one for each spin. The KS equations are then solved by using similar procedures to that of the non-spin polarized case.

Chapter 3

Numerical Quantum Many-body Tools

Several numerical methods have been developed and used to study strongly correlated quantum systems. This chapter gives a description of four methods usually employed to investigate their ground state properties. The first and the most direct method is Exact Diagonalization (ED). It allows the access to all the properties of a quantum system but at a high computational price. Due to the exponential increase of the memory required for a calculation with the system size, the applicability of ED is limited to small systems. The advantage of this method is, of course, its exact (within the model under investigation) and systematic character, since the lowest eigenstates and eigenvalues of any microscopic Hamiltonian can be computed without any approximation or intrinsic numerical limitations. Thus, ED results are free of any method uncertainty and stand as the benchmark for other numerical approaches.

The next two methods that will be discussed are the Numerical Renormalization Group (NRG) and the Density Matrix Renormalization Group (DMRG) schemes. NRG was originally developed to investigate the Kondo problem. Although it had enjoyed a huge success in solving the Kondo problem, when NRG is applied to other effective Hamiltonians like the Hubbard and Heisenberg models, it performs poorly.

The DMRG method was developed later to overcome the inadequacies of the NRG method. It possesses an accuracy comparable to ED and has been widely used to investigate one-dimensional and quasi one-dimensional quantum systems. DMRG, however, is not also free of drawbacks, and it performs best with open boundary conditions.

Finally, due to the inherent limitations in the applicability of both the ED and DMRG schemes, it is pertinent to explore alternative methods which can overcome some of these restrictions. One of such method is the DFT on a lattice. In the last section of this chapter, we introduce the Hubbard LDFT and the approximations used for constructing the XC functional.

3.1 Exact Diagonalization: Lanczos method

Exact Diagonalization (ED) simply involves diagonalizing the full interacting Hamiltonian to determine all its eigenvalues and eigenvectors. For the Hubbard Hamiltonian, $\hat{H}_U$, of L-sites, we have already seen that the Hilbert space contains 4^L elements. Since there is no term in the Hamiltonian that flips the spin, there is a sub-Hilbert space with fixed spin up and down electron number, $N_\uparrow$ and $N_\downarrow$, where the Hamiltonian is block diagonal and the calculation can be restricted to these subspaces. This then reduces the dimension of the Hilbert space to $\binom{L}{N_\uparrow}\cdot\binom{L}{N_\downarrow}$.

Another way to further reduce the dimension of the Hilbert space of an interacting Hamiltonian is to remove unnecessary states from its basis. This is, for example, the case for the t-J model where the doubly occupied states, higher in energy, are eradicated from the basis describing $\hat{H}_U$. Despite the reduction in the basis set that one can achieve by using symmetries, there is still a limit to the system size that can be handled by ED. This is essentially due to the fact that the basis set scales exponentially with L.

In condensed matter systems, low-energy properties are usually the subject of

one's main interest so that only the low-lying eigenstates are required. By using iterative diagonalization procedures it is then possible to increase by a few more sites the system size tractable with ED with results accurate to almost machine precision. The iterative diagonalization method allows one to calculate ground state properties as well as it provides access to a few low-lying excited states. A very powerful algorithm for iterative ED is the *Lanczos method* [81]. Detailed reviews on this method can be found in reference [82]. The spirit of the algorithm will be briefly explained here and we follow the description of reference [83].

It is possible to derive the Lanczos method from different points of view. The most popular perspective to construct the method is the reduction of an $n \times n$ symmetric matrix, H, to tridiagonal form by means of a three-term recurrence formula. Given a unit-norm initial vector, $|v_1\rangle$, the following recursive relation

$$\beta_{j+1}|v_{j+1}\rangle = H|v_j\rangle - \alpha_j|v_j\rangle - \beta_j|v_{j-1}\rangle \tag{3.1}$$

generates an orthonormal set of Lanczos vectors, $|v_j\rangle$, and the tridiagonal matrix defined as

$$H_T = \begin{pmatrix} \alpha_1 & \beta_2 & 0 & & & \\ \beta_2 & \alpha_2 & \beta_3 & 0 & & \\ 0 & \beta_3 & \alpha_3 & \beta_4 & \ddots & \\ & 0 & \beta_4 & \alpha_4 & \ddots & 0 \\ & & \ddots & \ddots & \ddots & \beta_n \\ & & & 0 & \beta_n & \alpha_n \end{pmatrix}. \tag{3.2}$$

In the equation 3.1, $\alpha_j = \langle v_j|H|v_j\rangle$, $\beta_{j+1} = \langle v_{j+1}|H|v_j\rangle$ and $\beta_1 = 0$. It can be shown that the vector $|v_{n+1}\rangle$ is zero, and that the following relation holds

$$HV - VH_T = 0, \tag{3.3}$$

where $V = [v_1, v_2, ..., v_n]$. In other words, the Lanczos recursion computes a tridiagonal matrix, H_T, which is orthogonally similar to H. An equivalent expression for β_{j+1} is $\beta_{j+1} = ||H|v_j\rangle - \alpha_j|v_j\rangle - \beta_j|v_{j-1}\rangle||$. It is often used in practice because it offers numerical stability [84]. This block diagonal matrix can then be easily diagonalized with standard library routines that one can find in LAPACK [85].

The Lanczos method is memory efficient since only the three vectors, $|v_{j-1}\rangle$, $|v_j\rangle$, and $|v_{j+1}\rangle$ need to be stored at once. Another important advantage of the Lanczos method is that accurate enough information about the ground state can be obtained with a small number, n, typically of the order of one hundred or less. With modern computers, it is possible to obtain the ground state properties of up to 20 sites using various symmetries present in the Hubbard model.

3.2 The Numerical Renormalization Group method

Historically, the idea of renormalization in solid state physics can be traced back to the 60's and the work done by Kadanoff [86], who formulates scaling relations for critical exponents by using a blocking procedure for spin clusters. Even though Kadanoff's spin blocking method was not really rigorous, it gave the basic idea of a renormalization procedure i.e. that of reducing the number of degrees of freedom of a problem without changing the form of the Hamiltonian but by changing its coupling constants. By repeating the blocking scheme process, a model numerically easy to solve because of the reduced degrees of freedom, which describes the physics of the original model, is obtained. In other words, some degrees of freedom are integrated out in order to produce a simpler model possessing the same physics.

The Numerical Renormalization Group (NRG) method developed by Wilson [87] is a very successful and systematic implementation of the renormalization concept. Wilson's contribution to this field earned him the Nobel prize in Physics in 1982 "for his theory for critical phenomena in connection with phase transition". The NRG is

a non-perturbative renormalization group (RG) approach to the quantum impurity problem [87, 88], which was first applied to the Kondo problem described by the equation (2.9). Systems controlled by this model usually exhibit anomalous transport properties. For example, the electrical resistance, instead of decreasing monotonically with temperature, shows a minimum at a temperature, T_K (the Kondo temperature), characteristic of the system. T_K depends non-analytically ($\ln T_K \propto 1/J$) on the spin exchange coupling, J, between the impurity and the conduction band (CB) of the host (for a detailed explanation see reference [50]). In what follows, we will introduce the basic concepts of the method as applied to the Kondo model.

3.2.1 Wilson's NRG applied to the Kondo Hamiltonian

Let us recall that the Kondo model for a spin S interacting locally with a non-interacting conduction electron sea can be written as

$$\hat{H}_{Kondo} = \sum_{k\sigma} \varepsilon_{k\sigma} \hat{c}^{\dagger}_{k\sigma} \hat{c}_{k\sigma} + J\vec{S} \cdot \sum_{\sigma\sigma'} \hat{c}^{\dagger}_{\sigma} \vec{\tau}_{\sigma\sigma'} \hat{c}_{\sigma'}, \tag{3.4}$$

where J is the Kondo coupling, $\hat{c}^{\dagger}_{\sigma}$ creates a conduction electron of spin σ at the impurity site and $\vec{\tau}$ is the Pauli matrix vector. Since the CB contains a lot of redundant information, Wilson's ingenious idea was to discretize its local density of states (DOS), $\varrho(w)$, logarithmically via a discretization parameter, λ, ($\lambda > 1$). Thus, he approximately mapped the Hamiltonian (3.4) to a semi-infinite chain:

$$\hat{H}^{Wilson}_{Kondo} = J\vec{S} \cdot \sum_{\sigma\sigma'} \hat{c}^{\dagger}_{0,\sigma} \vec{\tau}_{\sigma\sigma'} \hat{c}_{0,\sigma'} + \sum_{n=0}^{\infty} \sum_{\sigma} \xi_n \hat{c}^{\dagger}_{n,\sigma} \hat{c}_{n,\sigma} + \sum_{n=0}^{\infty} \sum_{\sigma} t_n (\hat{c}^{\dagger}_{n,\sigma} \hat{c}_{n+1,\sigma} + hc). \tag{3.5}$$

In the equation (3.5), the local spin, S, interact only with the fermion $\hat{c}^{\dagger}_{0,\sigma}$ at the end of the Wilson's chain while the on-site energies, ξ_n and the hopping parameters, t_n are solely functions of $\varrho(w)$. The parameters ξ_n and t_n can be numerically obtained

in a recursive manner [87]. However, for a flat and symmetric DOS where $\varrho(w) = 1/2D$ (D being the half-band width of CB), the t_n's have analytical expressions ($t_n \sim \lambda^{-n/2}$) and $\xi_n = 0$ [87]. The longer the chain becomes, the better the description of the infinite chain.

With the preceding observation, Wilson then solved the equation (3.5) iteratively by introducing the operator;

$$\hat{H}_n \equiv J\vec{S} \cdot \sum_{\sigma\sigma'} \hat{c}^{\dagger}_{0,\sigma} \vec{\tau}_{\sigma\sigma'} \hat{c}_{0,\sigma'} + \sum_{m=0}^{n} \sum_{\sigma} \xi_m \hat{c}^{\dagger}_{m,\sigma} \hat{c}_{m,\sigma} + \sum_{m=0}^{n} \sum_{\sigma} t_m (\hat{c}^{\dagger}_{m,\sigma} \hat{c}_{m+1,\sigma} + hc), \quad (3.6)$$

with the associated recursion relation

$$\hat{H}_{n+1} = \hat{H}_n + \hat{\zeta}_{n,n+1} + \hat{\mathcal{H}}_{n+1}, \quad (3.7)$$

where $\hat{\zeta}_{n,n+1} = t_n \sum_{\sigma} (\hat{c}^{\dagger}_{n,\sigma} \hat{c}_{n+1,\sigma} + hc)$ and $\hat{\mathcal{H}}_{n+1} = \xi_{n+1} \sum_{\sigma} \hat{c}^{\dagger}_{n+1,\sigma} \hat{c}_{n+1,\sigma}$ (see Figure 3.1). The procedure progresses by constructing from the low-energy eigenstates $|u\rangle_n$ of the operator H_n approximate eigenstates $|\tilde{u}\rangle_{n+1}$ of the operator H_{n+1}.

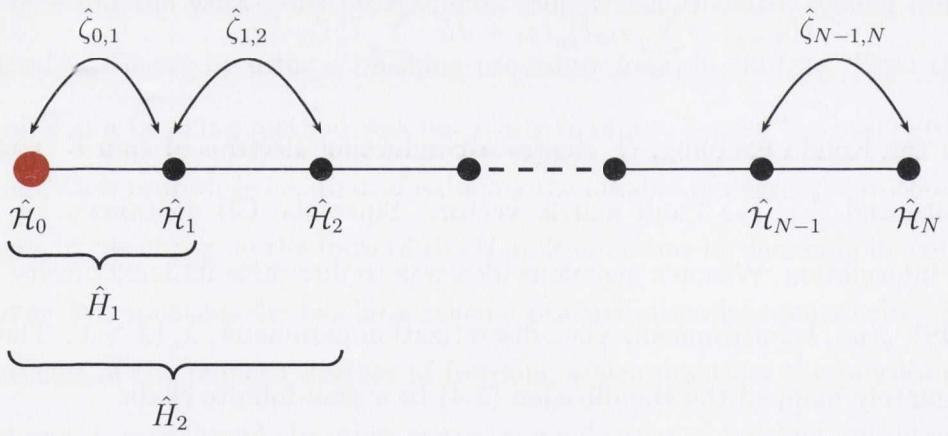

Figure 3.1: Schematic representation of Wilson's iterative procedure of the Hamiltonian H_n as sites are added. Wilson's chain of length N. The impurity is at the first site represented by a bigger red circle. The impurity Hamiltonian $\hat{\mathcal{H}}_0$ is the same as $\hat{H}_0$.

By using the above procedure, Wilson described the full crossover from a free

impurity spin at high temperatures to a screened spin at low temperatures in a non-perturbative manner [87], thereby solving the Kondo problem. Ever since the method was introduced in the original seminal paper [87], Wilson's NRG has become one of the principal tool in the field of quantum impurity physics (see for example reference [89] for its application to the Anderson impurity model).

3.2.2 Failure of NRG for one-dimensional lattice model

Motivated by the successful application of the NRG method to the Kondo problem, attempts were made to employ the technique to study other quantum lattice models such as the Hubbard and the Heisenberg Hamiltonian in 1D. However, rather poor performances were observed in the computation of the static properties like the ground state energy. In the first instance, there is significant difference between the Kondo Hamiltonian and 1D quantum lattice models setting the pace for the observed failure. The NRG tackled the Kondo problem by rewriting the Hamiltonian in a special form consisting of a chain with the impurity at one end and an exponentially decreasing hopping along the chain. On the other hand, the coupling remains unchanged between adjacent site all along the chain for the cases of 1D quantum lattice models.

In addition to the difference in the structure of the Hamiltonians, failure of NRG has been attributed to its difficulty in terms of boundary conditions. In order to illustrate this particular inadequacy, the NRG has been used to study the case of a non-interacting particle on a chain by White and Noack [90].

Let us consider a chain of length, L, with fixed boundary conditions so that the eigenfunction of a particle in the chain vanishes at both ends. If the chain is constructed from two chains of length, $L/2$, at an earlier stage in the NRG iteration, the ground state wavefunctions of the two half-chains have nodes at their ends. It is clear then that by using the ground state solutions of the two half-chains cannot

obtain a wavefunction with finite amplitude at $L/2$ for the ground state of the full system (of size L), as shown in Figure 3.2. Therefore, a refined treatment of the blocks' boundaries (in the present case, the two half-chains) making up the entire system is vital in formulating a reliable and accurate RG procedure.

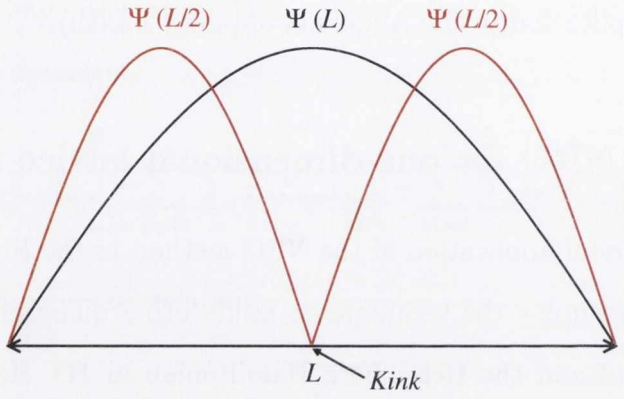

Figure 3.2 Figure illustrating that the ground state wavefunction of a large system (chain of length L shown in black) is not at all well represented by the tensor product of the ground state wavefunctions of its smaller systems (two half-chains of length $L/2$ shown in red).

White and Noack [90] solved the boundary conditions problem in the non-interacting case by using two types of techniques. The first one combines low lying eigenstates of several different block Hamiltonians with different boundary conditions (e.g. fixed and free, or periodic and anti-periodic) to form the new truncated basis. This is the so-called combination of boundary conditions (CBC) algorithm, which performs well by simulating a sufficiently general set of boundary conditions for the blocks. However, the CBC approach turns out to be unsuccessful for interacting systems like a Hesenberg 1D model. The reason for this failure is due to the difficulty in obtaining a set of kept states that comply with a wide range of boundary behaviour associated with different particles.

The second technique introduced in order to obviate to the NRG boundary conditions problem is called the superblock method. It requires a diagonalization of a large system (superblock) comprising of smaller systems (sub-blocks). The truncated

basis for any of the sub-blocks is then chosen by projecting the eigenfunctions of the superblock onto that sub-block. The idea is that, the projection will provide the conditions at the boundaries that the sub-block would see as part of the superblock. The RG proposed by White [27] is based on selecting the most desirable way of carrying out this projection. This will be discussed in the next section.

3.3 The Density Matrix Renormalization Group method

The Density Matrix Renormalization Group DMRG is one of the most commonly used numerical tools for studying the ground state properties of one-dimensional quantum models. The method was first introduced by White in 1992 [27]. The key idea of the DMRG scheme is that instead of keeping the lowest-lying eigenstates of a Hamiltonian associated to a sub-block, one keeps the most significant eigenstates of the sub-block's *density matrix*, obtained from diagonalizing the Hamiltonian of a larger section (superblock), which include the sub-block. Next, we will outline how this density matrix projection is carried out by following reference [28].

3.3.1 Density matrix projection

Given a large system, obtained as the combination of two sub-systems in contact, the concept of density matrix in statistical mechanics gives information on which states of the two sub-systems contribute the most to the ground state of the large one. We label an entire system as the *superblock* consisting of two interacting blocks, a *system block* and an *environment block* as shown in Figure 3.3. Let us assume that the superblock has been diagonalized to obtain a particular state, $|\psi\rangle$, e.g the ground state. Let $|i\rangle$ be the complete set of states of the system block and $|j\rangle$ the states of the environment block (see Figure 3.3). Then the state of the superblock $|\psi\rangle$ can be

expanded as

$$|\psi\rangle = \sum_{i,j} \psi_{ij} |i\rangle \otimes |j\rangle. \tag{3.8}$$

The reduced density matrix for the system block is defined as

$$\rho_{ii'} \equiv \sum_{j=1}^{N_j} \psi^*_{ij} \psi_{i'j}, \tag{3.9}$$

so that normalization ensures $\mathrm{Tr}\hat{\rho} = 1$. The density matrix has all the information needed from the wavefunction $|\psi\rangle$, to calculate any quantity within the system block. For instance, if an operator $\hat{A}$ acts on the system block, then

$$\langle \hat{A} \rangle = \sum_{ii'} A_{ii'} \rho_{ii'} = \mathrm{Tr}\hat{\rho}\hat{A}. \tag{3.10}$$

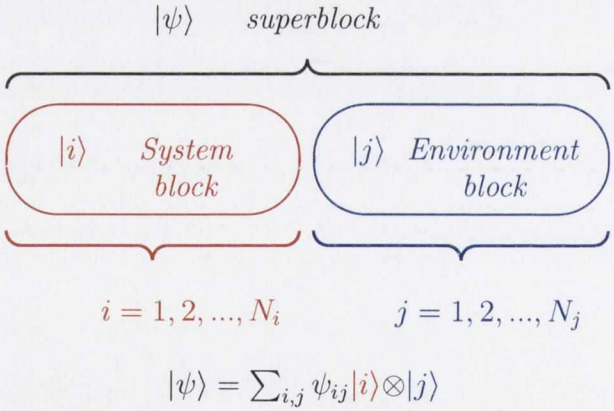

Figure 3.3: Sketch of the superblock containing a system block and an environment block.

The main task is to find a procedure that will produce a set of states of the system block, say, $|u^\alpha\rangle = \sum_i u^\alpha_i |i\rangle$, and $\alpha = 1, 2, ..., m$ which are optimal to represent $|\psi\rangle$. To be more precise, one aims at a possible approximate expansion (with the highest

accuracy) for $|\psi\rangle$ of the form

$$|\psi\rangle \approx |\tilde{\psi}\rangle = \sum_{\alpha,j} a_{\alpha j} |u^{\alpha}\rangle |j\rangle. \tag{3.11}$$

In other words, one wishes to minimize the error

$$S = ||\psi\rangle - |\tilde{\psi}\rangle|^2, \tag{3.12}$$

with respect to all $a_{\alpha j}$ and $|u^{\alpha}\rangle$ subject to the constraint that $\langle u^{\alpha}|u^{\alpha'}\rangle = \delta_{\alpha\alpha'}$, since $|u^{\alpha}\rangle$ forms a complete orthonormal basis. By defining $v_j^{\alpha} = \langle j|v^{\alpha}\rangle = N_{\alpha} a_{\alpha,j}$, with N_{α} chosen to set $\sum_j |v_j^{\alpha}|^2 = 1$, the error becomes,

$$S = \sum_{ij} [\psi_{ij} - \sum_{\alpha=1}^{m} a_{\alpha} u_i^{\alpha} v_j^{\alpha}]^2, \tag{3.13}$$

such that it is minimized over all u^{α}, v^{α} and a^{α}, given a specified value of m. The average of operator $\hat{A}$ of the equation (3.10) can then be written in terms of the eigenvalues w_{α} and eigenvectors $|u^{\alpha}\rangle$ of the density matrix

$$\langle \hat{A} \rangle = \sum_{\alpha} w_{\alpha} \langle u^{\alpha}|\hat{A}|u^{\alpha}\rangle. \tag{3.14}$$

Each w_{α} is the probability of the system block of being in the state $|u^{\alpha}\rangle$. The sum of all the density matrix eigenvalues goes to one and the deviation of this sum from unity measures the accuracy of the truncation to m states.

The solution to the above minimization problem can be mirrored to the singular value decomposition from linear algebra:

$$\psi = UMV^t, \tag{3.15}$$

where U and M are $N_i \times N_i$ matrices, V is an $N_i \times N_j$ matrix, U is orthogonal, V is

column-orthogonal, and the diagonal matrix M contains singular values of ψ. With this decomposition, it is possible to obtain the reduced density matrix [28, 91] such that the optimal system block states $|u^{\alpha}\rangle$ are the ones corresponding to the largest eigenvalues w_{α}. A rapid decay of the density matrix eigenvalues is important for the truncation procedure.

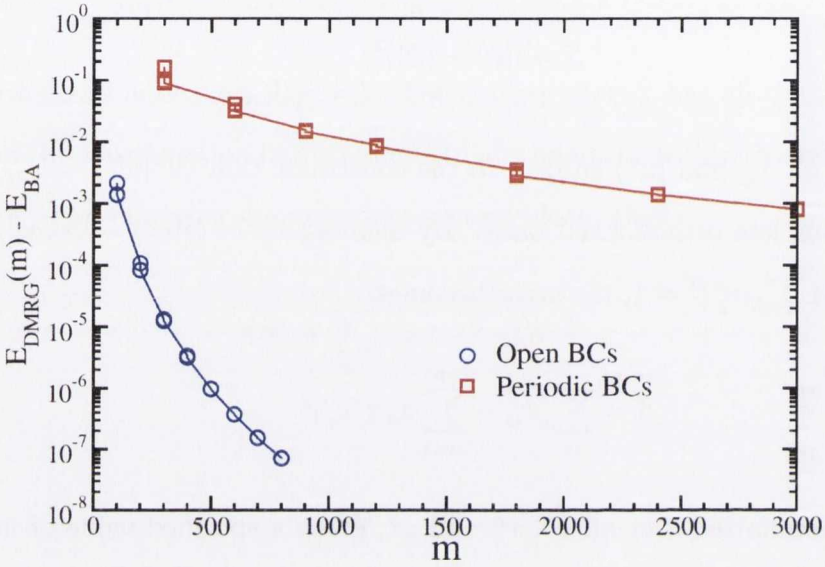

Figure 3.4: Error in the ground state energy calculated with the DMRG scheme as a function of the number m of density-matrix eigenstates kept for the 1D Hubbard Hamiltonian comprising of 100-site at half-filling and $U/t = 3$ with open (circles) and periodic (squares) boundary conditions (Taken from [92]).

Quite generally, the convergence of the deviation of the sum of the eigenvalues from unity with respect to m for periodic boundary conditions is much slower than for open boundary conditions. Thus, it is usually better to treat with the DMRG scheme systems with open boundary conditions than with periodic systems. As an example, the truncation error in the ground state energy for a 100-site Hubbard chain at half-filling and $U/t = 3$ is shown in Figure 3.4. For open boundary conditions (a favorable case for DMRG) the error decreases very rapidly with m until it reaches an order of 10^{-7} with $m = 500$ in 7 minutes on a 3 GHz Pentium 4 machine utilizing 400 MB memory. On the other hand, for periodic boundary conditions (a less favorable

case) the error decreases slowly with m and is still significant for the largest number of density-matrix eigenstates considered $m = 3000$ after 13 hours on a 3.4 GHz Xeon machine utilizing 6.5 GB memory.

3.3.2 DMRG algorithms

The DMRG algorithm consists of three main components:

1. Determination of the superblock configuration.
2. Decision on how to add new degrees of freedom.
3. Choosing the superblock eigenstate(s) from which the density matrix will be constructed. For ground state properties, only one eigenstate (the ground state) is used to form the density matrix. The state used in constructing the block density matrix is usually referred to as "target state".

A typical superblock configuration used in most DMRG calculations is as follows:

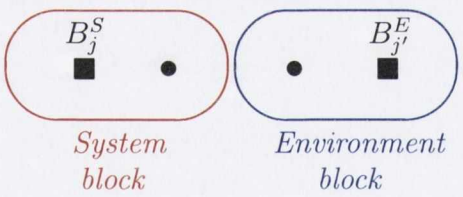

The system block contains a single site represented by the black circle (•) and a block, B_j^S, comprising of j sites represented by the black square (■). Similarly, the environment block contains a single site and a block, $B_{j'}^E$, comprising of j' sites. The total number L for the above superblock is therefore $L = j + j' + 2$. This set-up of the superblock is used at two slightly different stages of the DMRG algorithm. The first stage is the *infinite-system algorithm* and the second one is the *finite-system algorithm*. A detailed review on these algorithms can be found in [28, 93] but they will be briefly highlighted here.

The infinite-system algorithm

The infinite-system algorithm is usually the starting point of the DMRG scheme. It is used to iteratively grow the system size in real space, keeping a given number of the most important states represented as m. The iteration is usually terminated when a satisfactory system size is reached. Schematically the algorithm can be described as follows:

1. Start with a superblock configuration $B_j^S \bullet \bullet B_j^E$ so that the number of sites in the system block is the same as the environment block. Represent B_j^S and B_j^E by listing the quantum numbers (e.g. S^z and N) of their states and set up matrices for the block Hamiltonians and other operators in that basis.

2. Build the Hamiltonian matrix in sparse matrix form for the superblock. For instance, if each site is described by n states, the superblock will be described by n^L basis functions. (For instance, $n = 4$ and 2 for the Hubbard and the $S = 1/2$ Heisenberg model, respectively).

3. By using the Lanczos method (or other similar elaborate diagonalization procedures like Lanczos-Davidson algorithm [97]) diagonalize the superblock to find the target state, usually just the ground state. At this stage, it is possible to measure the expectation value of any operator by using the ground state wavefunction, $|\psi\rangle$.

4. Form the reduced density matrix for the system block by using the target state, i.e.

$$|\psi\rangle = \sum_{i,k} \psi_{ik} |i\rangle \otimes |k\rangle, \tag{3.16}$$

where i and k label the set of basis states on the system block ($B_j^S \bullet$) and environment block ($\bullet B_j^E$) respectively. As usual, the reduced density matrix

for the system block can be obtained by tracing over the degrees of freedom within the environment block i.e.

$$\rho = \sum_{k} \psi_{ik} \psi_{i'k}. \tag{3.17}$$

5. Diagonalize ρ to obtain the eigenvectors u_α with the largest eigenvalues w_α, $\alpha = 1, 2, ..., m$. Discard the remaining eigenvalues and eigenvectors.

6. Construct system block Hamiltonian, say $H_{B^S_{j+1}}$, and any other operator in the new system block, and transform them to the reduced density matrix eigenbasis as $H'_{B^S_{j+1}} = O H_{B^S_{j+1}} O$ where $O = (u_1, u_2, ..., u_m)$. The new environment block is formed by reflecting the system block. Also, new operators at the edges of the superblock are rotated by using the same transformation.

7. Start a new iteration by adding a site to the previous system and environment blocks. The superblock configuration is now $B^S_{j+1} \bullet \bullet B^E_{j+1}$.

8. Repeat again from step 2 by replacing L with $L + 2$ (i.e. enlarging the superblock by two sites).

The superblock size grows by two sites at each iteration step. The iterations are continued until a desired system size is obtained.

Finite-system algorithm

The infinite-system algorithm is only a "warm-up" procedure for the decisive finite-system algorithm. In other words, the infinite-system algorithm builds up a chain of length, say $L_{\max}$ (for convenience, $L_{\max}$ is assumed to be even), and finds an approximate ground state. The finite-system algorithm is then designed to investigate the properties of the fixed system size, with better accuracy. The algorithm *sweeps* from one side of the lattice to the other many times until a desired convergence is reached.

Usually, the convergence criterion is a comparison of the ground state energies in successive sweeps.

The finite-system algorithm consists of the following procedures:

1. The first step involves beginning with a superblock configuration $B_1^S \bullet \bullet B_1^E$, with B_1^S and B_1^E representing single site. Then, one uses the infinite-system algorithm to grow the superblock until $L_{\max}$ is reached (with a superblock configuration $B^S_{L_{\max}/2-1} \bullet \bullet B^E_{L_{\max}/2-1}$).

2. Next is the so-called "sweep procedure", used to enhance the convergence. It is a process which enlarges the system block by one site while at the same time reduces the environment block by one in order to keep the length of the superblock fixed. In other words, the superblock configuration goes from $B^S_{L_{\max}/2-1} \bullet \bullet B^E_{L_{\max}/2-1}$ to $B^S_{L_{\max}/2} \bullet \bullet B^E_{L_{\max}/2-2}$. One continues to increase the system block until it reaches $L_{\max} - 3$, with a superblock configuration $B^S_{L_{\max}-3} \bullet \bullet B_1^E$. In contrast to the infinite-system algorithm that does not require the block B_j^S after the formation of B_{j+1}^S, all the $L_{\max} - 3$ blocks and the operators on them are stored. These blocks are labelled by their size. At each step, the reduced density matrix is calculated by tracing out the degrees of freedom of the environment block.

3. In the next half of what is referred to as the *first* sweep, the growth direction is reversed. This implies interchanging the role of the two blocks, i.e. the old system blocks are now the environment blocks for the opposite growth direction and the former environment blocks are the new system blocks. These latter are enlarged by one site prior to projection. In essence, the superblock configuration from the last step ($B^S_{L_{\max}-3} \bullet \bullet B_1^E$) keeps changing until it reaches $B_1^S \bullet \bullet B^E_{L_{\max}-3}$. At each stage of the iteration, the new blocks formed are written to disk for use during the next sweep.

4. The second sweep starts with a superblock configuration $B_2^S \bullet \bullet B_{L_{\max}-4}^E$ and similar procedures of steps 2 and 3 are carried out for a complete sweep.

5. These sweeps are continued until the ground state energies in successive sweeps satisfy a pre-determined tolerance. Every repeated sweep gives a block wave function of better quality so that two or three sweeps are usually sufficient to reach convergence in the energy output.

In order to measure physical quantities in the DMRG framework, the expectation values of operators are calculated within a state or between states of the superblock, which are obtained in the iterative diagonalization step. This measurement is usually straightforward provided that the necessary operators are available in the appropriate basis. If we are interested in a local observable $\hat{A}_l$ for all site l such as the site occupation n_l, the single site expectation value of the operator is given by

$$\langle\psi|\hat{A}_l|\psi\rangle = \sum_{i,i'j} \psi_{ij}^* [\hat{A}_l]_{ii'} \psi_{i'j}. \tag{3.18}$$

where $|\psi\rangle$ is a state of the superblock and the matrix representation $[\hat{A}_l]_{ii'}$ is constructed when the site l is added to the system block, and must be transformed at each subsequent step so that it is available in the basis $|i\rangle$.

Developments in DMRG such as *dynamical* DMRG and *time-dependent* DMRG have not been discussed since they are beyond the scope of this thesis. For details on these extensions of the basis DMRG, we refer the reader to dedicated reviews [28, 93] and to the references therein.

3.4 DFT on lattice

From the preceding sections, we have seen that numerical solutions to the Hubbard Hamiltonian are either accessible to small system sizes or computationally expensive.

Over the last decades there have been a variety of elaborate many-body techniques designed to study the problem [94]. The application of DFT, which is exact in principle but limited by the approximations involved in defining the XC functional, as a technique to study many-body lattice model has gained attention in the last few years. The main reason for this is that it provides an alternative approach to study this model in order to gain insights into the physics of correlated electron systems.

The DFT concepts have been extended to lattice models [29, 30]. The underlying requirement for LDFT is the reformulation of the HK theorems and the KS equations, which were developed for the *ab initio* Hamiltonian and not for model Hamiltonians. In LDFT, the local site occupation, n_i, becomes the theory central quantity, and it plays the same role as the electron density $n(\vec{x})$ in *ab initio* DFT. It is defined as

$$n_i = \langle \Psi | \hat{n}_i | \Psi \rangle, \tag{3.19}$$

where $|\Psi\rangle$ is a generic many-body wavefunction (spin has been dropped here for simplicity).

The HK version of the LDFT demonstrates that it is possible to express all the quantities that can be obtained from the ground-state wavefunction as a function of site occupations [29, 30]. In particular:

1. The ground state energy and any other ground state observables are unique function of the site occupation.

2. The site occupation that minimizes the total energy functional is the exact ground state site occupation.

In other words, the ground state energy is obtained by minimizing the energy functional,

$$E(\{n_i\}) = \mathcal{F}(\{n_i\}) + \sum_i n_i v_{ext}^i, \tag{3.20}$$

where $\mathcal{F}(\{n_i\})$ is a *universal functional*[1] of all the site occupations $\{n_i\}$ and v^i_{ext} is a site dependent external potential. The $\mathcal{F}(\{n_i\})$ is written as

$$\mathcal{F}(\{n_i\}) = \langle\Psi|\hat{T} + \hat{\mathcal{H}}_{int}|\Psi\rangle, \tag{3.21}$$

where $\hat{T}$ and $\hat{\mathcal{H}}_{int}$ are the kinetic and interaction part of a lattice Hamiltonian respectively. If the exact form of $\mathcal{F}(\{n_i\})$ is known then, the ground state energy and site occupation could be obtained by minimizing the energy function with respect to n_i to produce the condition

$$\frac{\delta\mathcal{F}(\{n_i\})}{\delta n_i} + v^i_{ext} = \mu. \tag{3.22}$$

The constant, μ, is the Langrange multiplier enforcing particle number conservation (exactly as in standard DFT).

Just as in *ab initio* DFT, by reformulating the interacting many-body lattice problem as one for non-interacting particles, possessing same ground state density and total energy, one constructs a practical implementation of LDFT. Here the non-interacting Hamiltonian is of the form

$$\hat{\mathcal{H}}^i_s = \hat{T}^i_s + \sum_i \hat{n}_i v^i_s, \tag{3.23}$$

where $\hat{T}^i_s$ and v^i_s are respectively the non-interacting kinetic energy and local KS effective single particle potential, uniquely determined by the ground state site occupation n_i. The KS orbitals satisfy the single-particle Schrödinger like equation,

$$\hat{\mathcal{H}}^i_s \phi^{(\alpha)}_i = \varepsilon^{(\alpha)}_i \phi^{(\alpha)}_i, \tag{3.24}$$

[1] Universal functional means that the functional is independent of the external potential v^i_{ext} and for this particular case of 1D Hubbard Hamiltonian, it is a U dependent functional.

with the ground state occupation constructed from the occupied orbitals as

$$n_i = \sum_{\alpha,occ} f^{(\alpha)} |\phi_i^{(\alpha)}|^2, \tag{3.25}$$

where $f^{(\alpha)}$ are the occupation numbers, which satisfy $\sum_\alpha f^{(\alpha)} = N$ with N being the total number of electrons.

The single-particle functional is

$$\mathcal{F}_s(\{n_i\}) = E_s(\{n_i\}) - \sum_i \hat{n}_i v_s^i, \tag{3.26}$$

so that $\delta\mathcal{F}_s/\delta n = -v_s$. The XC energy, E_{xc}, can be defined as the difference between the interacting and the single-particle functionals,

$$\mathcal{F}(\{n_i\}) - \mathcal{F}_s(\{n_i\}) = E_{xc}(\{n_i\}) + E_H(\{n_i\}), \tag{3.27}$$

where E_H is the Hartree energy. By performing a functional derivative with respect to the site occupation, one obtains the effective KS potential as

$$v_s^i = v_{xc}^i + v_H^i + v_{ext}^i, \tag{3.28}$$

where v_H^i and v_{xc}^i are the Hartree and XC potential respectively,

$$\begin{aligned} v_{xc}^i &= \frac{\delta E_{xc}}{\delta n_i} \\ v_H^i &= \frac{\delta E_H}{\delta n_i}. \end{aligned} \tag{3.29}$$

Therefore the original functional minimization problem of DFT is mapped onto the diagonalization of single-particle Hamiltonian augmented with self-consistent solu-

tion of the effective KS potential. The KS ground state energy is then written as

$$E_{KS} = \sum_{\alpha,occ} f^{(\alpha)}\varepsilon^{(\alpha)} + E_{xc}(\{n_i\}) - E_H(\{n_i\}) - \sum_i v^i_{xc} n_i, \tag{3.30}$$

where the first term is the sum of the single-particle energies and the other terms are corrections for *double counting*.

It is also possible to calculate the concentration of the local pairs (or the doubly occupied sites) d which a measure of the pairing correlations. It is defined by

$$d \equiv \frac{1}{L}\sum_i \langle \hat{n}_{i\uparrow}\hat{n}_{i\downarrow}\rangle. \tag{3.31}$$

From equation (2.5), this quantity measures the derivative of the energy with respect to U, i.e.

$$d = \frac{\partial\langle \hat{H}_U\rangle}{L\partial U} = \frac{\partial E}{\partial U}, \tag{3.32}$$

where $E \equiv \langle \hat{H}_U\rangle/L$

Even though the KS formalism is exact and so much more easier to solve than the original many-body problem, the crucial task is now that of finding a suitable practical approximation for v^i_{xc}. Most LDFT employs the LDA-like density functional, where the ground state energy of the inhomogeneous system is approximated by the energy density of the homogeneous system at the same density. The remaining part of this chapter describes the one-dimensional homogeneous Hubbard model and the various approximate local functionals that can be constructed.

As this junction, we will like to remark, as already pointed out in references [39, 95], that the exchange interactions have been effectively eliminated in the 1D Hubbard model of equation (2.5) by restricting the model to one orbital per site. In order to relate the present description to the standard *ab initio* DFT formulation, E_{xc} and v_{xc} are conventionally referred to as XC energy and XC potential but it is

understood that the exchange contribution to these quantities is exactly zero. Also, attempts to correct for self-interaction errors in the XC energy for the model have been proposed by Capelle [36] and is a work in progress [96]. We, however, have not implemented the self-interaction corrections in this work.

3.5 Approximate functional: Bethe-ansatz local density approximation

3.5.1 Spin-polarized solution

Within the spin-polarized LDFT described above for a repulsive U, the fundamental quantities are the site occupation, n_i, and the site magnetization , m_i. We then define the site occupation for spin σ as

$$n_{i\sigma} = \sum_{\alpha,occ} f^{(\alpha)} |\phi_{i\sigma}^{(\alpha)}|^2, \tag{3.33}$$

and $n_i = n_{i\uparrow} + n_{i\downarrow}$ and $m_i = n_{i\uparrow} - n_{i\downarrow}$. The spin-dependent site occupation, $n_{i\sigma}$, can be calculated via the self-consistent solution of KS *like* equations;

$$\sum_{j=1}^{L} [-t_{ij} + v_s^{i\sigma}\delta_{ij}]\phi_{j\sigma}^{(\alpha)} = \varepsilon_{i\sigma}^{(\alpha)}\phi_{i\sigma}^{(\alpha)}. \tag{3.34}$$

The effective KS potential is written as $v_s^{i\sigma} = v_H^{i\bar{\sigma}} + v_{xc}^{i\sigma} + v_{ext}^{i\sigma}$, where $v_H^{i\sigma}$ is the Hartree potential $v_{ext}^{i\sigma}$ is the external potential and $v_{xc}^{i\sigma}$ is the derivative of the XC energy evaluated at $n_{i\sigma}$. $\sum_{\alpha,occ} f^{(\alpha)} = N$, N being the total number of electrons in the system.

The local spin density approximation (LSDA) for the XC potential is given by

$$v_{xc}^{i\sigma}|_{LSDA} = v_{xc,\sigma}^{hom}(n, m, t, U)|_{n\to n_i, m\to m_i}, \tag{3.35}$$

where the XC potential $v_{xc,\sigma}^{hom}(n,m,t,U)$ is that of the homogeneous Hubbard model. This is defined by

$$v_{xc,\sigma}^{hom}(n,m,t,U) = \frac{\partial}{\partial n_\sigma}\left[e(n,m,t,U) - e(n,m,t,U=0) - e_H(n,m,U)\right], \quad (3.36)$$

where $e(n,m,t,U)$ is the ground state energy per site of the 1D homogeneous Hubbard model with respect to t, U, $n = n_\uparrow + n_\downarrow$ and $m = n_\uparrow - n_\downarrow$ where $n_\uparrow = N_\uparrow/L$, $n_\downarrow = N_\downarrow/L$. The Hartree energy is given by

$$e_H(n,m,U) = \frac{1}{4}U(n+m)(n-m). \quad (3.37)$$

Finally, $e(n,m,t,U)$ can be obtained by using the BA solutions given in equation (2.30). The ground state energy per site for $U = 0$ is

$$e(n,m,t,U=0) = -\frac{4t}{\pi}\sin\left(\frac{n\pi}{2}\right)\cos\left(\frac{m\pi}{2}\right). \quad (3.38)$$

Direct numerical procedures can therefore be used to obtain $v_{xc,\sigma}^{hom}(n,m,t,U)$ as described in details in Appendix B following the references [39, 99]. Equations (2.31)-(2.33) and those in the Appendix B determine $v_{xc,\sigma}^{hom}(n,m,t,U)$ for the case of $n \leq 1$. Then, by using the particle-hole symmetry relation [45, 98], we can obtain the energy density from $n > 1$ as

$$e(n_\uparrow, n_\downarrow, U) = -(1-n)U + e(1-n_\uparrow, 1-n_\downarrow, U), \quad (3.39)$$

then $v_{xc,\sigma}^{hom}(n>1,m,t,U) = -v_{xc,\sigma}^{hom}(2-n,-m,t,U)$.

We have numerically implemented equations (2.31)-(2.33) and those in the Appendix B to produce the spin-polarized XC potentials of the one-dimensional homogeneous Hubbard model for both the majority spin and minority spin as shown in Figures 3.5(a) and 3.5(b) respectively. These figures clearly reveal that the poten-

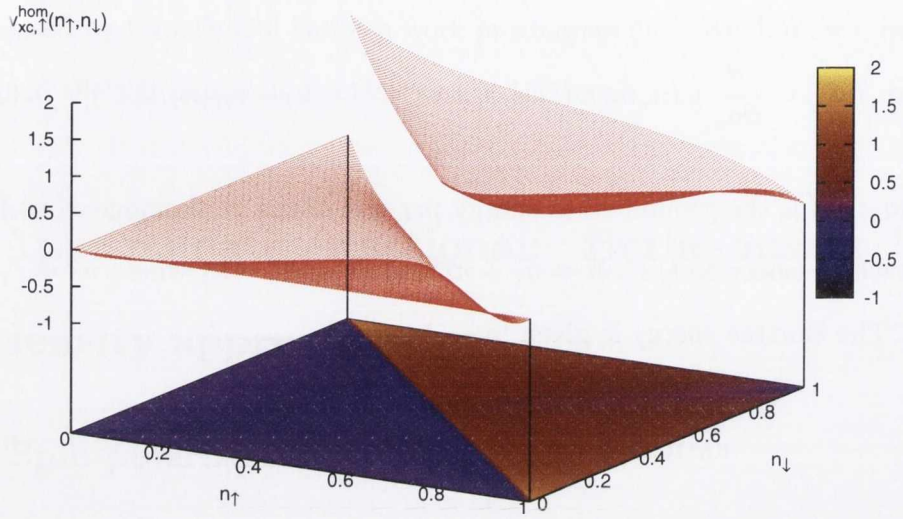

(a) Majority spin XC potential, $v^{hom}_{xc,\uparrow}(n_\uparrow, n_\downarrow)$.

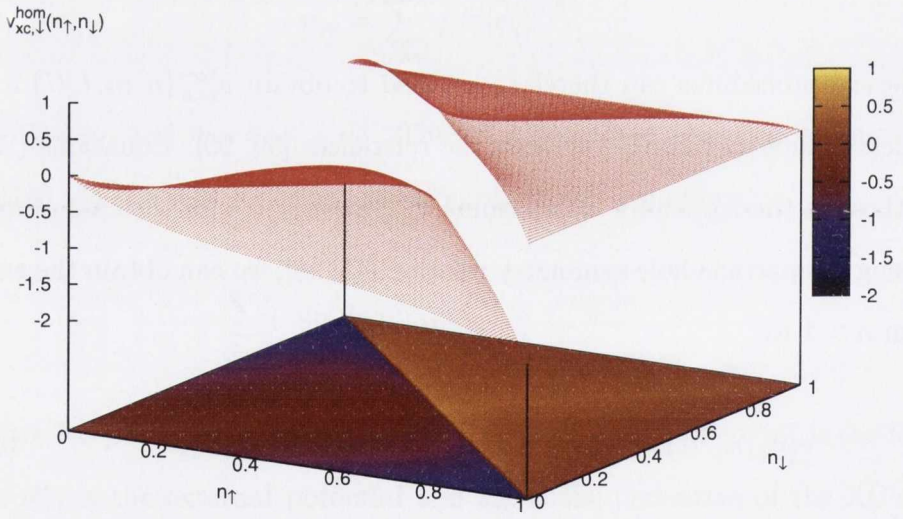

(b) Minority spin XC potential, $v^{hom}_{xc,\downarrow}(n_\uparrow, n_\downarrow)$.

Figure 3.: The spin-polarized XC potentials of one-dimensional homogeneous Hubbard model for $U/t = 4$ (The lower plot is a contour (colour) plot of the upper profile).

tials have discontinuity in the derivative at half-filling ($n = 1$, $N = L$). This reflects the fact that the underlying homogeneous 1D Hubbard model has a metal-insulation transition for $n = 1$. Such a discontinuity in the derivative of the potential, as in standard *ab initio* DFT, is responsible for the opening of the energy gap. This discontinuity is expected to be an added advantage over other LDA potentials in estimating the ground state properties of strongly correlated systems.

3.5.2 Non spin-polarized solution

For the non-spin polarized case, i.e. for spin symmetric systems with equal number of spin-up and spin-down electrons ($N_\uparrow = N_\Downarrow = N/2$), the ground state magnetization is zero, and the fundamental quantity of the theory is simply the site occupation, n_i.

$$n_i = \sum_{\alpha,occ} f^{(\alpha)} |\phi_i^{(\alpha)}|^2. \tag{3.40}$$

This is obtained via the self-consistent KS equations

$$\sum_{j=1}^{L} [-t_{ij} + v_s^i \delta_{ij}] \phi_j^{(\alpha)} = \varepsilon_i^{(\alpha)} \phi_i^{(\alpha)}. \tag{3.41}$$

where $v_s^i = v_H^i + v_{xc}^i + v_{ext}^i$. The LDA for the XC potential is simply

$$v_{xc}^i|_{LDA} = v_{xc}^{hom}(n, t, U)|_{n \to n_i}, \tag{3.42}$$

where the XC potential $v_{xc}^{hom}(n, t, U)$ of the homogeneous Hubbard model is deined by

$$v_{xc}^{hom}(n, t, U) = \frac{\partial}{\partial n}[e(n, t, U) - e(n, t, U = 0) - e_H(n, U)], \tag{3.43}$$

and $e(n, t, U)$ is the ground state energy per site of the 1D homogeneous Hubbard model with respect to $n = N/L$, t and U. Finally, $e_H(n, U) = Un^2/4$ is the Hartree

energy. The $e(n,t,U)$ can be obtained by using the BA solution and can be implemented in two ways:

1. BALDA/LSOC [2] - An analytical parameterization proposed by Lima *et. al.* [35, 36].

2. BALDA/FN - This one employs a direct numerical solution of the coupled Bethe Ansatz integral equations [39]. (FN = fully numerical)

BALDA/LSOC

In the limits $U = 0$ and $U \to \infty$, $e(n,t,U)$ is analytical and can be expressed as (for the less than half-filled case, $n < 1$) [65]

$$e(n,t,U=0) = -\frac{4t}{\pi}\sin\left(\frac{n\pi}{2}\right) \tag{3.44}$$

and

$$e(n,t,U\to\infty) = -\frac{2t}{\pi}\sin\left(n\pi\right). \tag{3.45}$$

At half-filling ($n = 1$) and any interaction U,

$$e(n,t,U) = -4t\int_0^\infty dx \frac{J_0(x)J_1(x)}{x[1+\exp(xU/2t)]}, \tag{3.46}$$

where J_0 and J_1 are zero and first order Bessel functions respectively.

Based on the similarity of equations (3.44) and (3.45), Lima *et al.* [36] proposed a functional of the form

$$e(n,t,U) = -\frac{2t\beta}{\pi}\sin\left(\frac{n\pi}{\beta}\right), \tag{3.47}$$

where β is a parameter which depends on U and t and it is fixed by requiring that

[2] LSOC is after the name of Lima, Silva, Oliviera and Capelle, who proposed the approximation.

equation (3.47) recovers the correct limit of half-filling ($n = 1$), i.e.

$$-\frac{2t\beta}{\pi}\sin\left(\frac{\pi}{\beta}\right) = -4t\int_0^\infty dx \frac{J_0(x)J_1(x)}{x[1+\exp(xU/2t)]}. \tag{3.48}$$

For any value of U and t which define a fixed Hamiltonian, the transcendal equation (3.48) can be computed easily for β and has exactly one solution in the physical interval ($U = 0, U \to \infty$), corresponding to the interval ($\beta = 1, \beta = 2$). This calculation takes place outside the KS self-consistent DFT loop (i.e. the XC potential is calculated up-front for any U/t).

For the more than half-filled case, due to the particle-hole transformation [45, 98],

$$e(n > 1, t, U) = e(2 - n, t, U) + U(n - 1). \tag{3.49}$$

$$v_{xc}^{hom}(n, t, U) = t\mu\left[2\cos\frac{k\pi}{\beta} - 2\cos\frac{k\pi}{2} + \frac{kU}{2}\right], \tag{3.50}$$

where $k = 1 - |n - 1|$, and μ =sgn$(n - 1)$.

BALDA/FN

The alternative route for constructing the XC potential is that of employing a direct numerical solution of the coupled BA integral equations. This is done by observing that $v_{xc}^{hom}(n, t, U)$ satisfies [39, 99]

$$v_{xc}^{hom}(n, t, U) = -2t\int_{-Q}^{Q} dk\rho_n(k)\cos k - 4tQ_n\rho(Q)\cos Q + \Delta v_{KH} \tag{3.51}$$

where $\Delta v_{KH} = 2t\cos(n\pi/2) - Un/2$, $\rho_n(k) \equiv \partial\rho(k)/\partial n$ and $\sigma_n(\lambda) \equiv \partial\sigma(\lambda)/\partial n$ satisfying the integral equations in Appendix A for $\zeta = n$. Equations (2.31)-(2.33), (3.51) and those in Appendix A determine $v_{xc}^{hom}(n, t, U)$ and due to symmetry $v_{xc}^{hom}(n > 1, t, U) = -v_{xc}^{hom}(2 - n, t, U)$.

In this work, we have implemented both numerical procedures within BALDA to

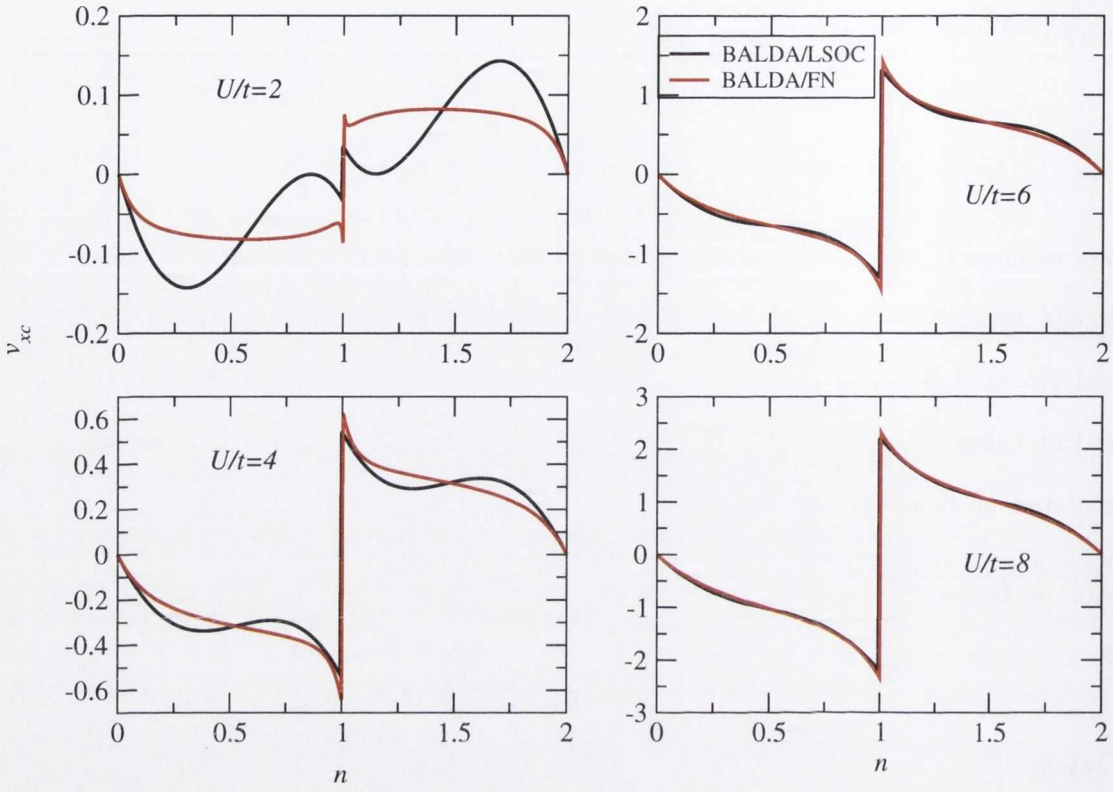

Figure 3.6: The non spin-polarized XC potential of one-dimensional Hubbard model as a function of density for different values of U/t using BALDA/LSOC and BALDA/FN

obtain the XC potential. In the case of BALDA/LSOC, $\beta = 1.51432, 1.31593, 1.22182$ and 1.16951 for $U/t = 2, 4, 6$ and 8 respectively. In the Figure 3.6, the XC potentials as a function of filling for the two schemes are shown for different U/t values. Similar to the spin-polarized XC potentials, they also manifest discontinuity at $n = 1$. We also observe that the two parameterizations always coincide by construction at $n = 0$ and $n = 2$ but that their agreement over the entire n range depends on the value of U. In particular one can report a progressively good agreement as U/t increases. This is not a surprise since the BALDA/LSOC potential is constructed to exactly reproduce the $U \to \infty$ limit.

Finally, there are still noticeable differences in the XC potentials obtained from the BALDA/LSOC and BALDA/FN at weak interaction strength, perhaps reflecting the weakness of the parameterization of LSOC in this regime as we will show later.

As an example of the inherent weakness present in the BALDA/LSOC at small interaction strength, one can show that the gap in the XC potential at $n = 1$ is [34]

$$\Delta_{\text{hom}}^{\text{BALDA/LSOC}}(U)/t = U + 4\cos\left(\frac{\pi}{\beta(U)}\right). \tag{3.52}$$

We plot in Figure 3.7 $\Delta_{\text{hom}}^{\text{BALDA/LSOC}}(U)/t$ as a function of U. On the same Figure, the gap obtained numerically for the BALDA/FN is shown. From the plot, the gap is negative for very weak interaction strengths revealing already signature of some shortcoming of the BALDA/LSOC in this regime. On the contrary, the gap in the BALDA/FN is always positive as expected.

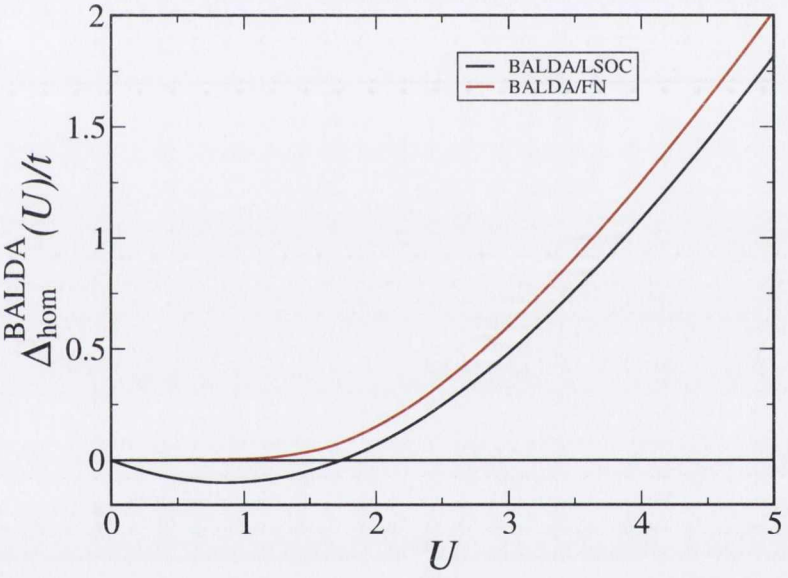

Figure 3.7: The gap of the homogeneous XC potential at half-filling as a function of U within the BALDA/LSOC.

Chapter 4

Application of LDFT-BALDA to ground state and linear response properties.

4.1 Ground state total energy comparison

We begin this chapter with a discussion on the ground state energy of the one-dimensional homogeneous and inhomogeneous Hubbard models. In particular, we employ the LDFT-BALDA and compare results for the two approximations to the XC potential described in the previous chapter. In order to establish the accuracy of these approximations, we further compare results with those obtained with ED and DMRG. Note that throughout this work we always stay away from the half-filling case, where the derivative discontinuity of the potential makes the LDFT convergence problematic.

4.1.1 Homogeneous Hubbard Model

Here we compute the ground state total energy per site, E_0/L, of a finite chain described by $\hat{H}_U$ with L sites and containing N electrons. The system sizes considered

here are restricted to those manageable by ED and are non-spin polarized. Given our computational resources, we only consider system sizes in the range of $3 \leq L \leq 14$ and $2 \leq N \leq 10$. First, we use BALDA functionals to calculate E_0/L and compare their results with ED. The comparison of the BALDA calculations with those obtained by ED is done by calculating the relative error between them,

$$\Delta = \frac{|E_0^{ED} - E_0^{BALDA}|}{|E_0^{ED}|} \times 100\%. \tag{4.1}$$

Similar comparison has already been reported in the literature for close to and at quarter filing [36] but we have extensively considered wide range of system sizes.

In the upper panels of Figure 4.1(a), we display the E_0/L contour plots as a function of L and N for open boundary conditions (OBC) and $U/t = 4$ for both BALDA functionals. In the lower panels are their corresponding contour plots for Δ. We note that the results obtained for both of these functionals match quite well the ED ones. We obtain discrepancies of less than 5% over the range of combinations of L and N considered, except those very close to the MIT where difficulties arise for convergence in the self-consistent KS equations. The contour profile for Δ shows that BALDA/FN suffers large deviation when compared with ED for small lattice sites. The reason for this is the full numerical *exact* thermodynamic limit built into the construction of the potential, in contrast to the BALDA/LSOC which interpolates some known analytical limits. However, as the system size increases BALDA/FN gives a reasonably close values to that of ED over most combinations investigated.

Next, we investigate the ability of the two approximations to XC at differentiating between different boundary conditions. In the upper panels of Figure 4.1(b), we present the E_0/L contour plots as a function of L and N for periodic boundary conditions (PBC) and $U/t = 4$ for both BALDA functionals. It is clear that the upper panels of 4.1(a) and those of Figure 4.1(b) are distinctively different for both functionals. The lower panels of 4.1(b) are their corresponding Δ contour plots

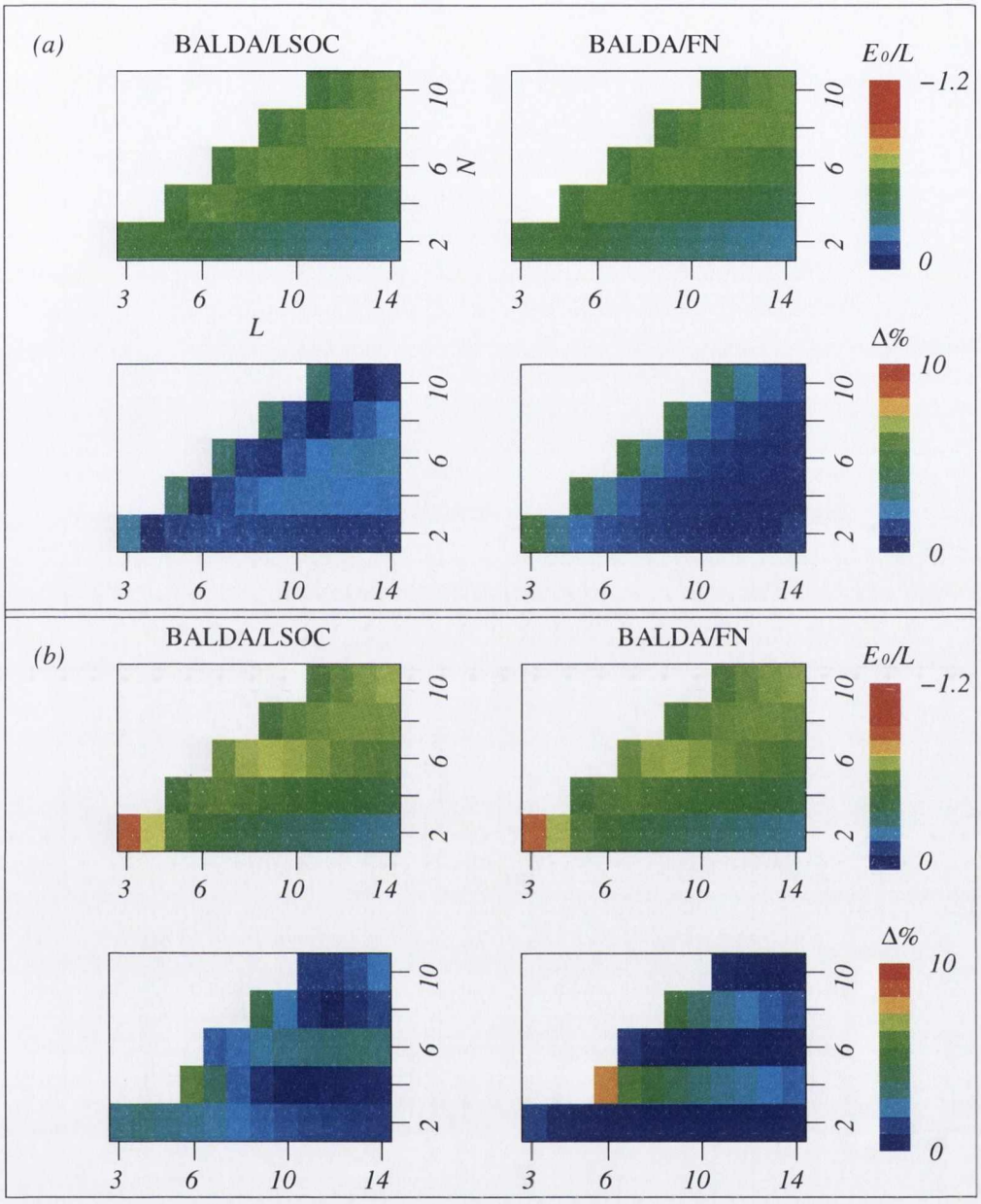

Figure 4.1: Contour plots of total energy per site, E_0/L, and percentage deviation, Δ, from the ED with respect to L sites and N electrons for $U/t = 4$ with different boundary conditions (a) Open boundary condition (OBC) and (b) Periodic boundary condition (PBC) (see tables D.1 and D.2 for data set)

which shows deviations of not more than 6% in the spectra. This unambiguously indicates that LDFT within BALDA is a suitable technique applicable to both OBC and PBC without any limitation. Thus, unlike the DMRG method, it can tackle problems involving PBC with reasonable accuracy. This property will be very useful

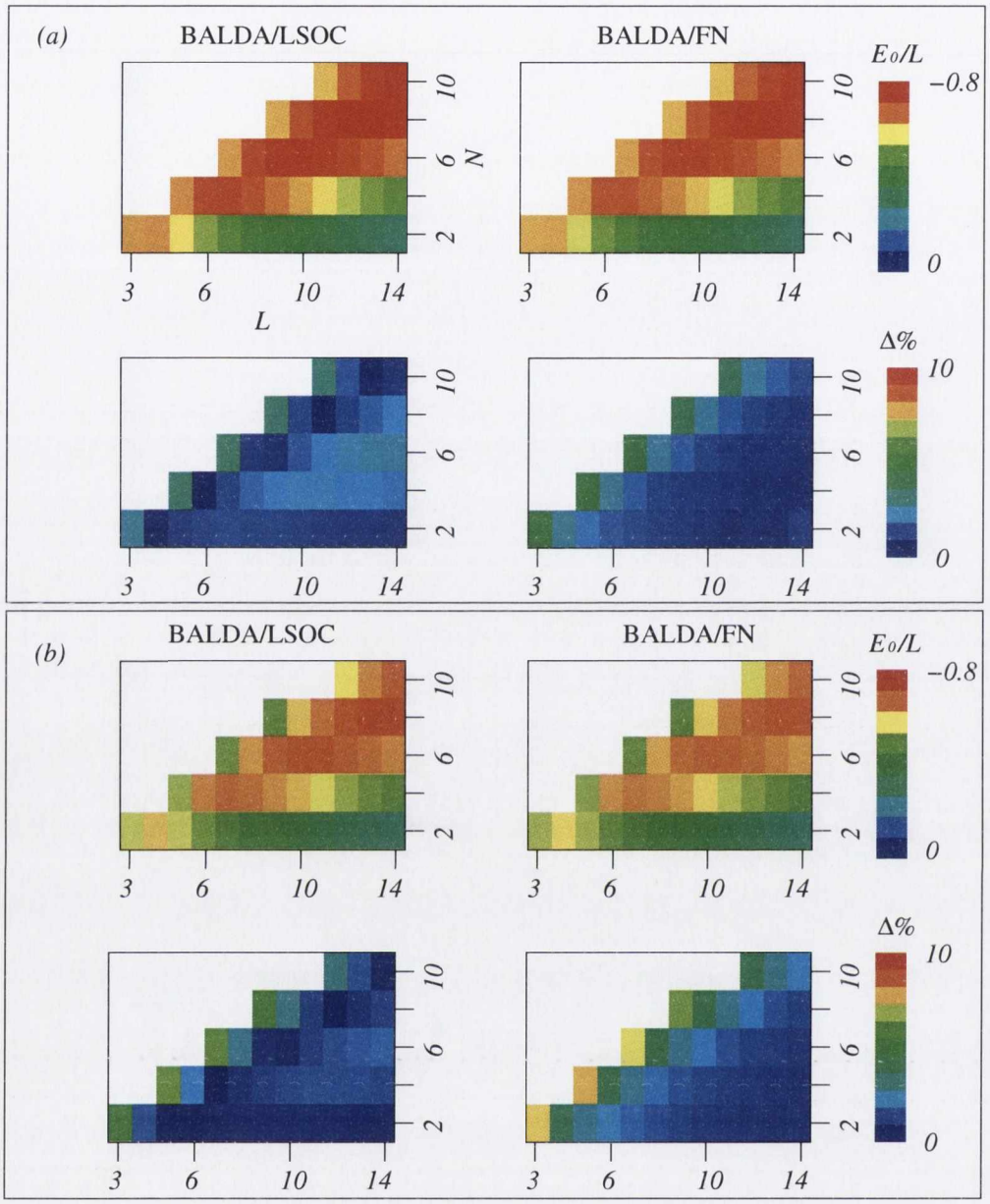

Figure 4.2: Contour plots of total energy per site, E_0/L, and percentage deviation, Δ, from the ED with respect to L sites and N electrons for open boundary condition but different U/t (a) $U/t = 4$ and (b) $U/t = 6$ (see tables D.1 and D.3 for data set).

in the next chapter where we will study mesoscopic Hubbard rings penetrated by an external magnetic flux with LDFT.

Further, we look at the capability of BALDA approximations to LDFT to capture the effects of electron-electron interactions. We observe an increase in E_0/L as

the interaction strength increases from $U/t = 4$ [upper panels of Figure 4.2(a)] to $U/t = 6$ [upper panels of Figure 4.2(b)] for both BALDA/LSOC and BALDA/FN[1]. For the Hubbard Hamiltonian, an increase in U/t will raise the total ground state energy, an effect reliably captured by both functionals with errors of much less than 8% in a wide range of parameter space [lower panels of Figures 4.2(a) and 4.2(b)]. Again, the deviation of the calculated values for E_0/L from the exact results reduces as the system size increases with BALDA/FN consistently following this pattern. This clearly demonstrates that both approximations to Hubbard LDFT are able to describe the effects of electron-electron interaction properly.

Finally, it is very illuminating to consider the computational advantage of the LDFT within BALDA over ED. As an example, a calculation of E_0/L for $L = 20$ and $N = 10$ with OBC and $U/t = 4$ on our Core(TM)2 Quad 2.66 GHz machine takes about sixty minutes in computational time and requires 3GB computer memory with ED. Meanwhile same calculation done by BALDA for both flavours on the same machine only takes less than one minute and utilizes less than 10MB computer memory. This shows that the computational resources needed by BALDA are of orders of magnitude smaller than those of ED thus highlighting the computational efficiency of these functionals. Therefore BALDA can be used to compute total energy and energy related properties of large system sizes which would have been computationally expensive and sometimes impossible to access using other well established numerical techniques.

[1]Note the difference in the scale used for figures 4.1 and 4.2.

4.1.2 Inhomogeneous Hubbard model

Here, we consider the one-dimensional Hubbard model with various degrees and patterns of inhomogeneity. The Hamiltonian is now

$$\hat{H}_{U_i}^{v_i} = -t \sum_{\langle ij \rangle \sigma} (\hat{c}_{i\sigma}^{\dagger} \hat{c}_{j\sigma} + hc) + \sum_{i} U_i \hat{n}_{i\uparrow} \hat{n}_{i\downarrow} + \sum_{i\sigma} v_i \hat{c}_{i\sigma}^{\dagger} \hat{c}_{i\sigma}, \tag{4.2}$$

and spatial variations are introduced in the on-site Coulomb interactions, U_i, and/or on-site energies, v_i. Inhomogeneity can be the result of in-equivalent sites in the natural unit cell, modulation of system parameters in artificial heterostructures, or self-consistent modulations in local system properties due to formation of charge-ordered states [100]. Interestingly, such superlattices have been recognized to exhibit complex ground states and transport properties [100, 101, 102].

In view of this, we calculate the ground state energies of various superlattices which consist of a repeated pattern of L_u interacting sites with repulsive interaction U and L_0 non-interacting ($U = 0$) sites. We focus on the case $v_i = 0$. Table 4.1 shows results for a 200-site system with OBC, different number of electrons and different correlation strength obtained by DMRG, BALDA/LSOC and BALDA/FN while taking $L_u = L_0 = 10$ (thus this superlattice has 10 bi-layers). We have already explained in Chapter 2 that the most commonly used method to obtain numerically the ground state energies for large systems with an accuracy comparable to ED is the DMRG [28, 93]. It usually performs best with open boundary conditions and its computational demands depend on the number of states kept in the calculation. Our DMRG calculations are performed by employing the widely used Algorithms and Libraries for Physics Simulations (ALPS) [103] package for strongly correlated quantum mechanical systems. The DMRG results are obtained by retaining dominant density matrix eigenvectors such that the truncation error is of the order of $\mathcal{O}(10^{-10})$. From the table, it is easy to see that the LDFT-BALDA results are in

N	METHOD	U			
		1	2	4	6
50	DMRG	-96.312	-95.892	-95.562	-95.433
	LSOC	-96.879(0.59)	-96.549(0.69)	-96.134(0.60)	-95.910(0.50)
	FN	-96.330(0.02)	-95.939(0.05)	-95.647(0.09)	-95.535(0.11)
80	DMRG	-146.449	-144.893	-143.464	-142.837
	LSOC	-147.667(0.83)	-146.397(1.04)	-144.830(0.95)	-143.998(0.81)
	FN	-146.468(0.01)	-144.954(0.04)	-143.599(0.09)	-143.021(0.13)
100	DMRG	-174.864	-172.034	-169.132	-167.779
	LSOC	-176.423(0.89)	-174.032(1.16)	-171.029(1.12)	-169.426(0.98)
	FN	-174.881(0.01)	-172.089(0.03)	-169.290(0.09)	-168.021(0.14)
120	DMRG	-198.310	-193.843	-189.083	-186.745
	LSOC	-200.056(0.88)	-196.114(1.17)	-191.254(1.15)	-188.647(1.02)
	FN	-198.330(0.01)	-193.905(0.03)	-189.232(0.08)	-186.974(0.12)
150	DMRG	-222.992	-215.192	-206.314	-201.841
	LSOC	-224.612(0.73)	-217.366(1.01)	-208.487(1.05)	-203.811(0.98)
	FN	-223.013(0.01)	-215.260(0.03)	-206.500(0.09)	-202.113(0.14)
180	DMRG	-233.675	-221.654	-207.641	-200.438
	LSOC	-234.703(0.44)	-223.132(0.67)	-209.255(0.78)	-201.992(0.78)
	FN	-233.695(0.01)	-221.725(0.03)	-207.819(0.09)	-200.679(0.12)
200	DMRG	-232.523	-217.379	-199.114	-189.695
	LSOC	-233.030(0.22)	-218.234(0.39)	-200.210(0.55)	-190.960(0.67)
	FN	-232.548(0.01)	-217.445(0.03)	-199.305(0.10)	-189.973(0.15)

Table 4.1: Table showing total energy, E_0/t, for different U and N with OBC obtained by DMRG, BALDA/LSOC and BALDA/FN. $L = 200$ and $L_u = L_0 = 10$. The percentage deviation, Δ, from the DMRG is given in the parenthesis.

very good agreement with the DMRG ones. The relative errors of both the BALDA functionals from the DMRG results are shown in parenthesis and are always of the order of 1%. The accuracy of BALDA/FN is again particularly good over the entire range of U and N investigated.

In table 4.2, we report results for similar calculations performed on a 100-site chain with increased modulation strength, $L_u = L_0 = 2$. The agreement for energies computed with the local functionals are within 2% from the DMRG values within our parameter space. Clearly the performance of LDFT-BALDA for slowly modulated lattices is slighly better but generally the qualitative agreement is impressive. This is consistent with similar calculations done by using only the BALDA-LSOC functional

N	METHOD	U			
		1	2	4	6
20	DMRG	-38.889	-38.689	-38.484	-38.380
	LSOC	-39.127(0.61)	-39.013(0.84)	-38.846(0.94)	-38.745(0.95)
	FN	-38.912(0.06)	-38.753(0.17)	-38.615(0.34)	-38.557(0.46)
40	DMRG	-73.036	-72.149	-71.191	-70.693
	LSOC	-73.684(0.89)	-73.039(1.23)	-72.227(1.46)	-71.786(1.55)
	FN	-73.084(0.07)	-72.307(0.22)	-71.589(0.56)	-71.275(0.82)
60	DMRG	-99.010	-96.912	-94.678	-93.558
	LSOC	-99.906(0.91)	-98.139(1.27)	-96.037(1.44)	-94.941(1.48)
	FN	-99.057(0.05)	-97.064(0.16)	-95.068(0.41)	-94.148(0.63)
80	DMRG	-113.813	-109.384	-104.282	-101.629
	LSOC	-114.609(0.70)	-110.562(1.08)	-105.738(1.40)	-103.248(1.59)
	FN	-113.865(0.05)	-109.558(0.16)	-104.773(0.47)	-102.413(0.77)
100	DMRG	-115.948	-108.571	-100.272	-96.222
	LSOC	-116.289(0.29)	-109.365(0.73)	-101.703(1.43)	-97.997(1.85)
	FN	-116.016(0.06)	-108.839(0.25)	-101.038(0.76)	-97.337(1.16)

Table 4.2: Table showing total energy, E_0/t, for different U and N with 0BC obtained by DMRG, BALDA/LSOC and BALDA/FN. $L = 100$ and $L_u = L_0 = 2$. The percentage deviation, Δ, from the DMRG is given in the parenthesis.

by Silva *et al.* [37].

Finally, in the same spirit of a typical density profile of a superlattice investigated in reference [37], we show in Figure 4.3 the site occupation profile of a 80-site chain at quarter filling with $L_u = 3$, $L_0 = 2$ and $U/t = 4$ for the LDFT-BALDA methods and DMRG. From the graph, we see that the results of both functionals reproduce quite well, both in qualitative and quantitative terms, those of DMRG. We observe a deviation of not more than 3% and 1% for the BALDA/LSOC and BALDA/FN respectively from the DMRG calculations around the centre of the chain. These deviations are slightly higher at the edges since they are cases where LDA fails badly.

To summarize this section, we have employed the two approximations to the XC potential of the LDFT to investigate the energetics of homogeneous and inhomogeneous Hubbard models. We compared results from these approximations with those

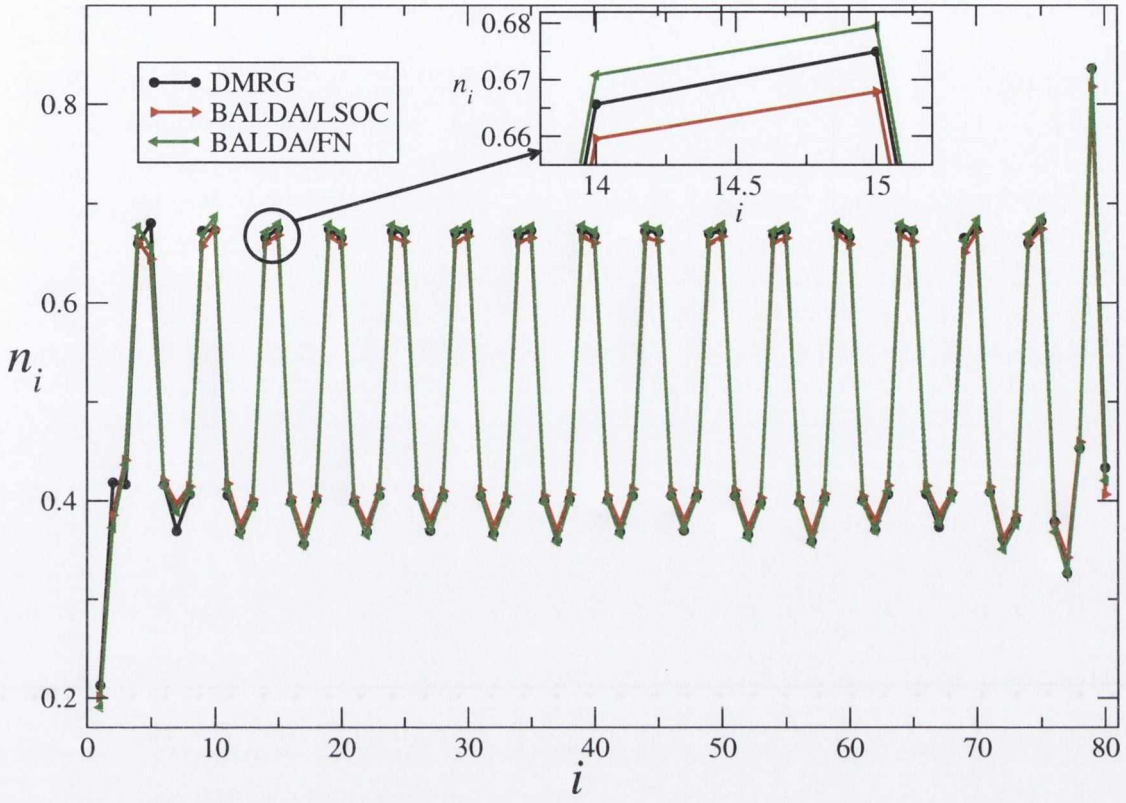

Figure 4.3: Density profile of $L = 80$ at quarter filling with $L_u = 3$, $L_0 = 2$ and $U/t = 4$. The inset shows a magnification of site occupation for $14th$ and $15th$ sites. The lines are a guide for the eye.

obtained with ED and DMRG over extensive range of parameters. We observed that there is a substantial agreement between the numerically exact schemes and LDFT-BALDA. Also, the computational efforts, both in time and memory, of the LDFT-BALDA are orders of magnitude less than ED and DMRG. Of particular note is that effects such as the role of electron-electron interactions, boundary conditions and diverse range of inhomogeneity are well reproduced by LDFT-BALDA. Hence, we propose its application to linear response properties like polarizability.

4.2 Polarizabilities

Generally, the constituent atoms of a material under the influence of an external electric field develop an oscillating separation of charges that tend to counteract the

field. This field make the material to undergo distortion and then becomes polarized with an induced dipole moment. The molecular composition of the material acts as a dipole with dipole moment p_i so that the polarization (dipole moment vector per unit volume), P, is given as

$$P = \sum_i p_i, \tag{4.3}$$

where i is over the dipoles in the unit volume. The strength of the external field, E, determines the induced polarization in a material. For a weak field,

$$P = \chi E, \tag{4.4}$$

where χ is the polarizability of the medium.

In relation to an atom or molecule, the electric field distorts their electron distribution so that the molecular polarization is also proportional to the external field with a constant of proportionality, α, corresponding to the polarizability an atom or molecule. The polarizability of a system depends on the number of charges present in it so that for atoms or molecules polarizability increases with their size. It is one of the fundamental electronic properties used by the experimentalists to characterize the nature of different materials and it is a field of growing interest for researchers [104, 105]. For example, Ishihara *et. al.* [46] have studied electron covalency contributions to electronic polarizability in important transition metal oxides (TMO) and dielectric compounds using the Hubbard model. In particular, for one-dimensional systems where quantum confinement as a result of reduced dimensionality can lead to enhanced linear and non-linear susceptibilities of these systems, as compared to their three-dimensional counterparts. Rojo and Mahan have studied the response of interacting fermionic systems to an electric field in small 1D systems using ED [47]. The knowledge of this property is critical for the development of different class of strongly correlated materials in low dimensional systems.

We calculate the electrical polarizability of linear chains with the finite difference method, i.e. as numerical derivative of calculations performed at different external electric fields. An external electric field enters into the problem by adding to the Hubbard Hamiltonian $\hat{H}_{\mathrm{U}}$ the term

$$\hat{H}_{\mathcal{E}} = e\mathcal{E}\hat{x} = e\mathcal{E}\sum_{i=1}^{L}(i-\bar{x})c_i^{\dagger}c_i\,, \tag{4.5}$$

where $\bar{x} = \frac{1}{2}(L+1)$ is the middle site position of the chain, e is the electronic charge ($e = -1$) and $\mathcal{E}$ is the electric field intensity (the electric field is applied along the chain). Note that in equation (4.5), $\hat{x}$ is not a unit vector but an operator. In general the electrical dipole, P, induced by an external electric field can be calculated simply as the expectation value of the dipole operator over the ground state wave-function $|\Psi_0(\mathcal{E})\rangle$ (note that this is a general definition so that $|\Psi_0(\mathcal{E})\rangle$ is not necessarily the Kohn-Sham ground-state wave-function), i.e.

$$P = e\langle\Psi_0(\mathcal{E})|\sum_{i=1}^{L}(i-\bar{x})c_i^{\dagger}c_i|\Psi_0(\mathcal{E})\rangle = \frac{\mathrm{d}E_0(\mathcal{E})}{\mathrm{d}\mathcal{E}}, \tag{4.6}$$

where E_0 is the ground state energy. For small fields P can be Taylor expanded about $\mathcal{E} = 0$ so that the linear polarizability, α, is defined as

$$P \sim \alpha\mathcal{E} + \gamma\mathcal{E}^3 + \mathcal{O}(\mathcal{E}^5)\,, \qquad \alpha = \frac{\mathrm{d}^2E_0(\mathcal{E})}{\mathrm{d}\mathcal{E}^2}\,. \tag{4.7}$$

Our calculation then simply proceeds with evaluating $E_0(\mathcal{E})$ for different values of $\mathcal{E}$ and then by fitting the first derivatives with respect to the field to the equation (4.7), as indicated in reference [47]. We have also performed a number of numerical tests and verified that the polarizabilities calculated from the site occupation [intermediate formula in equation (4.6)] essentially coincides with those obtained from the total energy. We note that our finite difference scheme is not accurate enough for

calculating the hyper-polarizability, γ, which then is not investigated here.

As we have shown in the last section and have also been already extensively reported that BALDA-LDFT gives a substantially good agreement with exact calculations in terms of ground state total energy [34, 35]. The polarizability however offers a more stringent test for the theory since it involves derivative of E_0. Hence it is important to compare the various approximations with exact results. For small

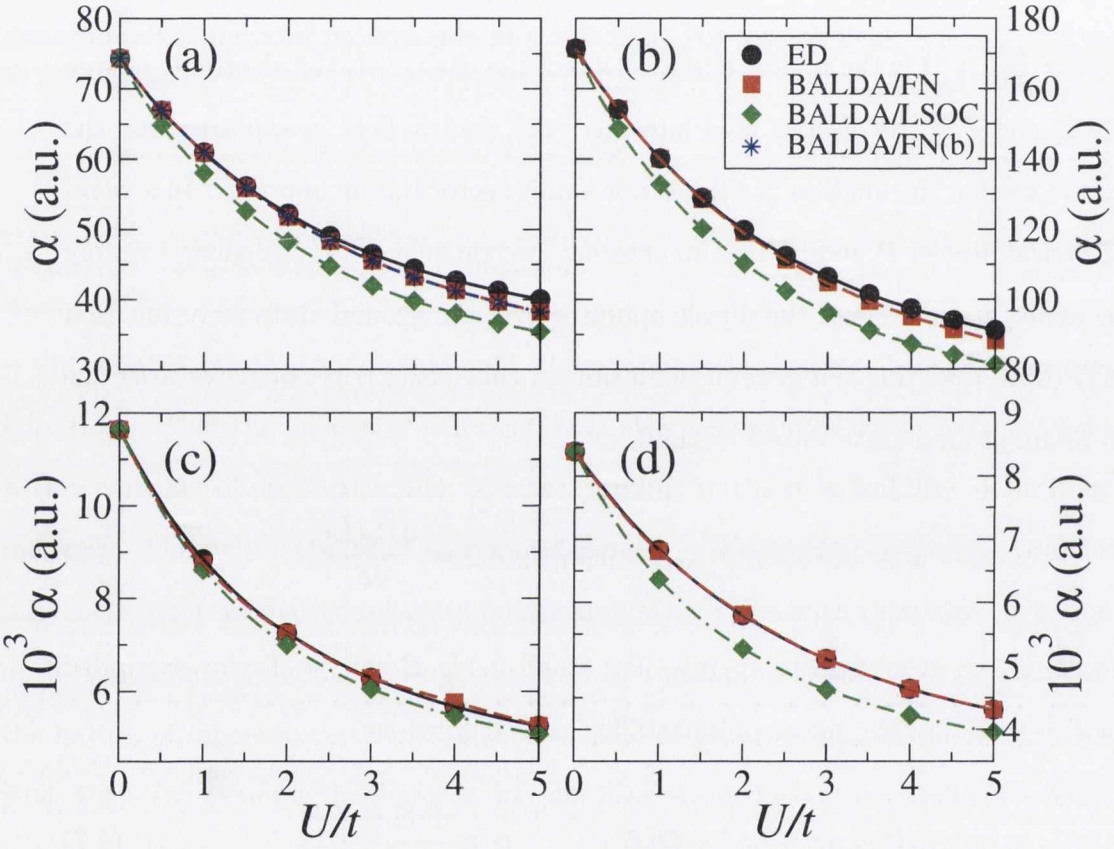

Figure 4.4: Linear polarizability, α, as a function of the Coulomb repulsion U/t. Results are presented for BALDA/LSOC and BALDA/FN and they are compared with those obtained with either exact diagonalization (ED) or DMRG calculations. In the various panels we show: (a) $L = 12$ at quarter filling ($n = 1/2$), (b) $L = 16$ at quarter filling, (c) $L = 60$ and $N = 20$, and (d) $L = 60$ at quarter filling.

chains, $L < 18$, these are obtained by simply performing ED. However for the longer chains ED is no longer feasible and we employ instead the DMRG scheme [28, 93]. The DMRG results are obtained by using a cutoff of $m = 350$, i.e. by retaining the

dominant 350 density matrix eigenvectors.

Let us start our analysis by looking at the polarizability as a function of the energy scale U/t. Representable results for quarter-filling, $n = 1/2$, and for $n = 1/3$ are presented in the various panels of Figure 4.4. As a test of our numerical accuracy in the panel (a) of the figure we also report results obtained by calculating α from the site occupation instead then from the total energy (these calculations are labeled with "BALDA/FN(b)"). One can then observe that the two methods return practically indistinguishable polarizabilities.

In general we find that the polarizability decreases monotonically with increasing the on-site repulsion U. This is indeed an expected result since an increase in on-site repulsion means a suppression of charge fluctuations and consequently a reduction of α. Away from $U = 0$ the dependence of α on U/t can be fitted with

$$\alpha(U/t; L, n) = \alpha_0(L, n) \left(\frac{U}{t}\right)^{-\xi(L,n)} , \tag{4.8}$$

where all the parameters have a dependence on the length of the chain and on the band filling. The results of such a fitting procedure are reported in table 4.3. Note that in the fit we did not impose any constraints and we have included only points with $U/t \geq 1$.

From the fit and from Figure 4.4 one can immediately note that both the BALDA flavors of the exchange and correlation functional reproduce rather well the exact results, in good agreement with previously published calculations [142]. The agreement is particularly good for the FN functional, which matches the ED/DMRG results almost perfectly over the entire range of U/t's and filling investigated. A quantitative assessment of goodness of the BALDA results is provided in Figure 4.5 where the relative error, δ, from the reference exact calculations is presented. In general, and as expected, we find that the error grows with U/t, i.e. with the system departing from the non-interacting case. However, there is also a saturation of the error as the

Method	L	N	n	α_0	ξ
ED	12	6	1/2	59.69	0.23
BALDA/LSOC				62.06	0.27
BALDA/FN				59.50	0.25
ED	16	8	1/2	142.88	0.27
BALDA/LSOC				135.07	0.31
BALDA/FN				143.56	0.30
DMRG	60	30	1/2	8939.5	0.32
BALDA/LSOC				8673.1	0.33
BALDA/FN				8837.8	0.31
DMRG	60	20	1/3	6931.6	0.29
BALDA/LSOC				6401.0	0.30
BALDA/FN				6920.7	0.29

Table 4.3: Scaling parameters for $\alpha(U/t; L)$ as obtained by fitting the data of Fig. 4.4 to the expression of equation (4.8). Note that the fit has been obtained without any constraints and by including data only for $U/t \geq 1$.

interaction strength increases, reflecting the fact that both the BALDA potential are exact in the limit of $U \to \infty$. As a further consequence of the $U \to \infty$ limit, we also observe that the relative error between BALDA/LSOC and BALDA/FN reduces as U grows.

Another important aspect is the computational advantage of LDFT-BALDA over ED. For example, in the calculations each data point for $L = 12$ takes about 6 hours in computational time and requires 200MB computer memory while that of $L = 16$ takes about 8 hours in computational time and requires 3GB in computer memory with ED. Meanwhile calculations done by BALDA for both flavours take only few seconds thus highlighting the computational efficiency of these methods.

Given the accuracy of the BALDA/FN scheme we have decided to use the same to investigate in greater detail the scaling properties of $\alpha(U/t; L)$. First we look at the scaling as a function of the interaction strength U/t. In this case we always consider a chain containing $L = 60$ sites for which the deviation from the DMRG results is never larger than 2%. Furthermore this is a length which allows us to explore a rather

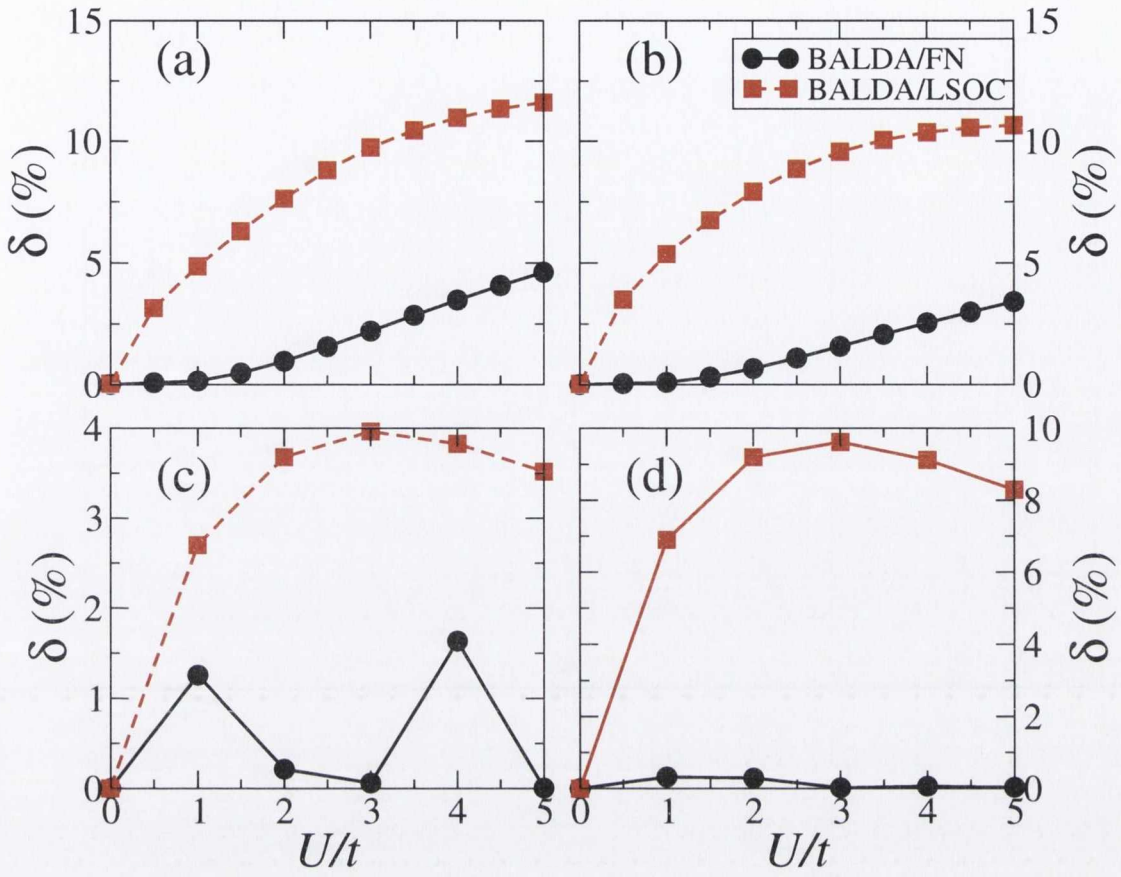

Figure 4.5: Relative error between BALDA calculated polarizabilities and those obtained with exact methods (either ED or DMRG). In the panels we show: (a) $L = 12$ at quarter filling ($n = 1/2$), (b) $L = 16$ at quarter filling, (c) $L = 60$ and $N = 20$, and (d) $L = 60$ at quarter filling.

large range of electron filling, so that it allows us to gain a complete understanding of the scaling properties. Our results are presented in Figure 4.6 where we show α as a function of U/t for different filling factors, we list the values of ξ obtained by fitting the actual data for $U/t \geq 1$ to the expression in equation (4.8) and we provide (inset) the dependence of ξ on n.

In general the fit to our data is excellent, suggesting the validity of the exponential scaling of the polarizability with the interaction strength (away from half filling). In particular we find that ξ decreases monotonically with n for $n > 0.2$ but it increases for smaller values. This means that $\xi(n)$ has a maximum just before $n = 0.2$, which appears rather sharp (see inset of Figure 4.6). We are at present uncertain about the

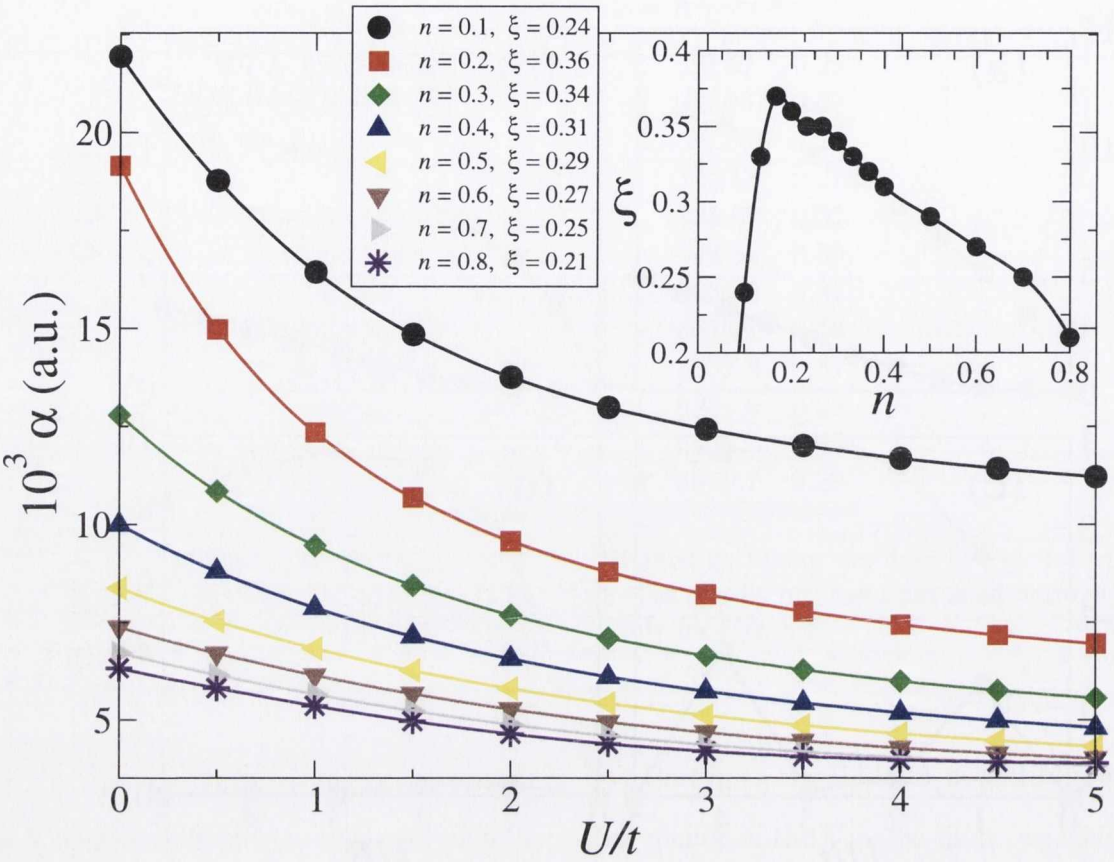

Figure 4.6: Polarizability as a function of U/t for a chain of 60 sites and various filling factors, n. The Figure legend reports the fitted values for the exponent ξ [see equation (4.8)]. The symbols represents the calculated data while the solid lines are just to guide the eyes. In the inset we present the exponent ξ as a function of the filling factor n.

precise origin of such a non-monotonic behavior. However, as we will see in details later on, we notice that the response of the exchange and correlation potential to the external electric field has an anomaly for small U and n. We believe that such an anomaly might be the cause of the non-monotonic behaviour of ξ.

Next we turn our attention to the scaling of α with the chain length. In Figure 4.7 we present $\alpha(L)$ for two different filling factors ($n = 1/3$ and $1/2$) and different values of U/t. Data are plotted both in linear and logarithmic scale, from which a clear power-law dependence of α on L emerges. A fit to our data provides the

following scaling

$$\alpha(U/t; L) = \alpha_1 L^{\gamma} . \tag{4.9}$$

Importantly this time we find essentially no dependence of both α_1 and γ on either U/t or n. The fit reveals a value for the exponent of $\gamma \sim 3$ (the range is from $\gamma = 2.93$ to $\gamma = 2.98$). This is what expected for free electrons in 1D [47], and it is substantially different from the predicted linear scaling at $n = 1$. Our results thus confirm that away from $n = 1$ the electrostatic response of the Hubbard model is similar to that of the non-interacting electron gas. Going in more details we find a rather small monotonic dependence of γ on U/t. This however depends also on n since for $n = 1/3$ we find that γ reduces as U/t is increased (from 2.98 for $U/t = 0.5$ to 2.93 for $U/t = 100$), while the opposite behavior is found for $n = 1/2$ ($\gamma = 2.94$ for $U/t = 0.5$ and 2.96 for $U/t = 100$).

4.3 Response of the BALDA potential to the external field

In *ab initio* DFT the failures of local and semi-local XC functionals in reproducing accurate linear polarizabilities are related to the incorrect response of the XC potential to the external electric field [106, 107], which in turn originates from the presence of the self-interaction error [108, 109]. In particular for *ab initio* DFT the exact XC potential should be opposite to the external one, while the LDA/GGA (generalized gradient approximation, GGA) returns a potential which responds in the same direction. In order to investigate the same feature for the case of the Hubbard model LDFT we calculate the potential response

$$\Delta v_{\mathrm{xc}} = v_{\mathrm{xc}}^{\mathcal{E}}(n_i) - v_{\mathrm{xc}}^{\mathcal{E}=0}(n_i) , \tag{4.10}$$

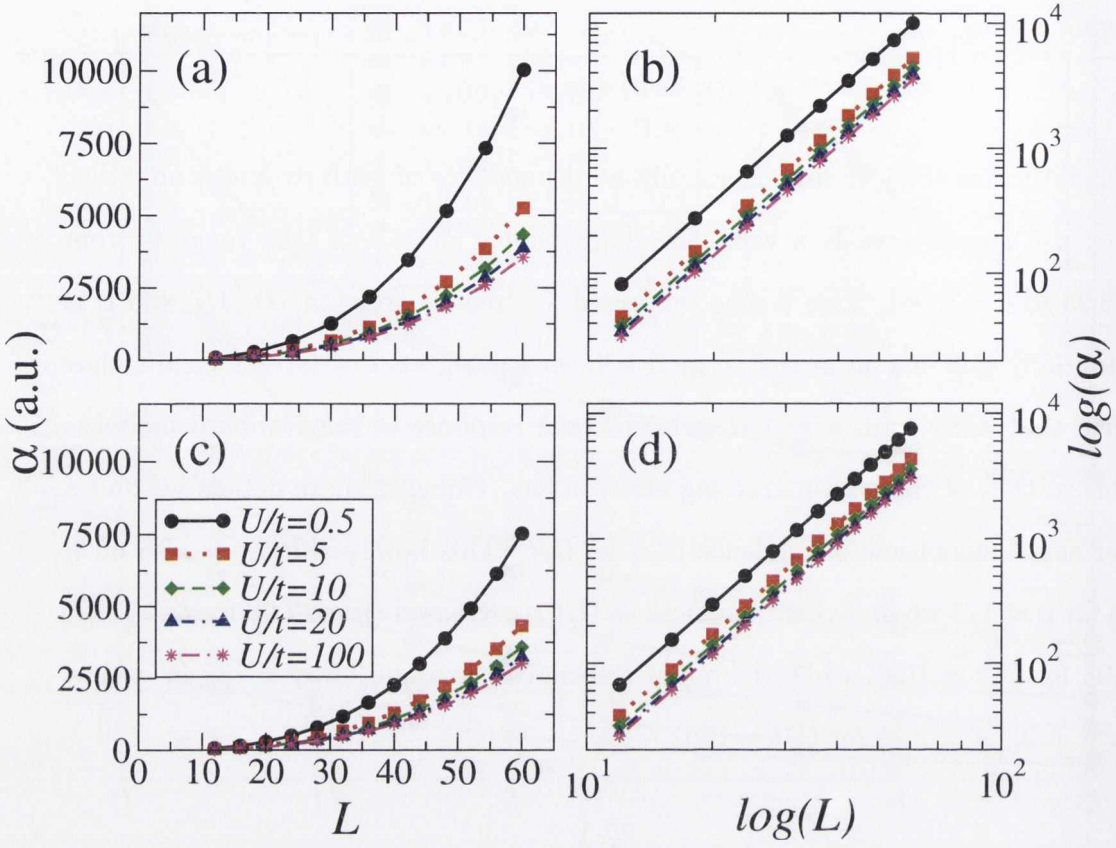

Figure 4.7: Scaling of the polarizability as a function of the chain length, L. Panel (a) and (b) are for $n = 1/3$ while (c) and (d) for $n = 1/2$. Note the linear dependence of the $\alpha(L)$ curve when plotted on a log-log scale, proving the relation $\alpha(L) = \alpha_1 L^\gamma$

where $v_{\rm xc}^{\mathcal{E}}(n_i)$ is the exchange and correlation potential at site i in the presence of an electric field $\mathcal{E}$. Also in this case we adopt the finite difference method and we use $\mathcal{E} = 0.01$, after having checked that the trends remain unchanged irrespectively of the field strength.

In order to provide a benchmark for our calculations we also need to evaluate the potential response for the exact Hubbard model. We construct the exact potential by reverse engineering, a strategy introduced first by Almbladh and Pedroza [110] and by von Barth [111] and then applied to both static and time dependent LDFT by Verdozzi [42]. This consists in minimizing about the Kohn-Sham potential the

functional $\mathcal{F}$ (in reality here this is just a function) defined as

$$\mathcal{F}[v_{\rm xc}] = \sum_{i}^{L} (n_i^{\rm KS} - n_i^{\rm exact})^2, \tag{4.11}$$

where $n_i^{\rm exact}$ is the exact site occupation at site i as obtained by either ED or the DMRG method, while $n_i^{\rm KS}$ is the Kohn-Sham one. For clarification purpose, the reverse engineering idea emanated from Almbladh and Pedroza [110] and von Barth [111] but they did it in a way different from the equation (4.11).

Our results are summarized in Figures 4.8 and 4.9, where we show $\Delta v_{\rm xc}$ as a function of the site index for a 60 site chain occupied respectively with 10 ($n = 1/6$) and 30 ($n = 1/2$) electrons. The external electrostatic potential here decreases as the site number increases, i.e. it has a negative slope. Results are presented for DMRG, BALDA/LSOC and BALDA/FN and for different values of U/t.

In general and in contrast with *ab initio* DFT, we find that the response of the exact Hubbard-LDFT XC potential is in *the same direction* of the external perturbation for both the filling factors investigated and regardless of the magnitude of U/t. The response however becomes larger as U/t is increased (the slope of $\Delta v_{\rm xc}$ is more pronounced), a direct consequence of the fact that for large U's small deviations from an homogeneous charge distribution produce large fluctuations in the potential. Such a behaviour is well reproduced by both the BALDA functionals, with the BALDA/FN scheme performing marginally better than the BALDA/LSOC one, and reflecting the same trend already observed for the polarizabilities.

There is however one anomaly in the potential response for the BALDA/LSOC functional, namely at $n = 1/2$ and for small U/t (respectively 2 and 4) the potential response is actually opposite (positive slope) to that of the DMRG benchmark. This means that in these particular range of filling and interaction strength the BALDA/LSOC potential erroneously opposes to the external perturbation. The

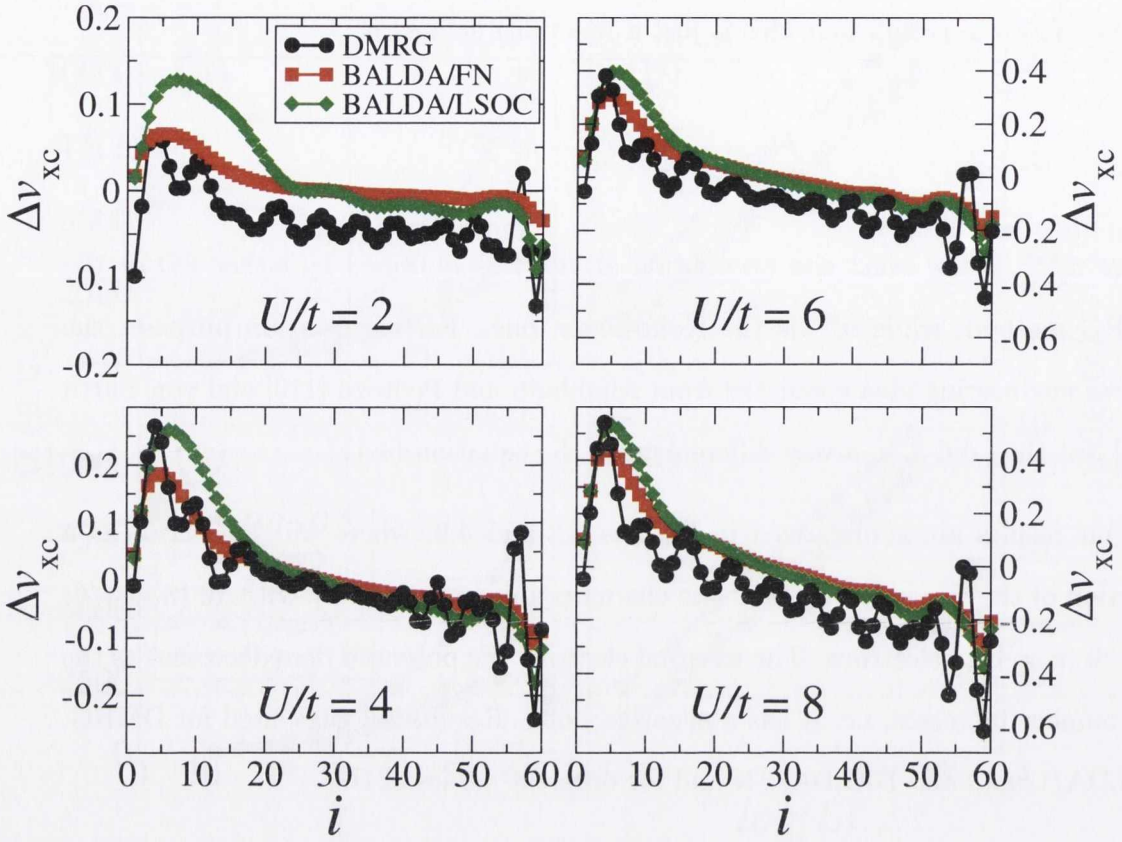

Figure 4.8: The difference, Δv_{xc}, between the XC potential calculated at finite electric field and in absence of the field as a function of the site index. Results are presented for a 60 site chain with $N = 10$ ($n = 1/6$). The dots are the calculated data while the lines are a guide to the eye. The external potential has a negative slope.

anomaly originates from the particular shape of the BALDA/LSOC potential as a function of n for small U/t (see Figure 3.6). In fact, v^i_{xc} for BALDA/LSOC has a minimum for both $U/t = 2$ and $U/t = 4$ at around $n = 1/4$, which means that its slope changes sign when the occupation sweeps across $n = 1/4$. Therefore for those critical interaction strengths the response is expected to be along the same direction of the external potential for $n < 1/4$ and for $3/4 \lesssim n \leq 1$ and opposite to it for $1/4 < n \lesssim 3/4$ (at $n \sim 3/4$ there is a second change in slope).

In the case of the BALDA/FN functional such an anomaly is in general not expected, except for small U/t and n close to the discontinuity at $n = 1$ (see Figure 3.6). This, however, is in the range of occupation not investigated here. Nevertheless we

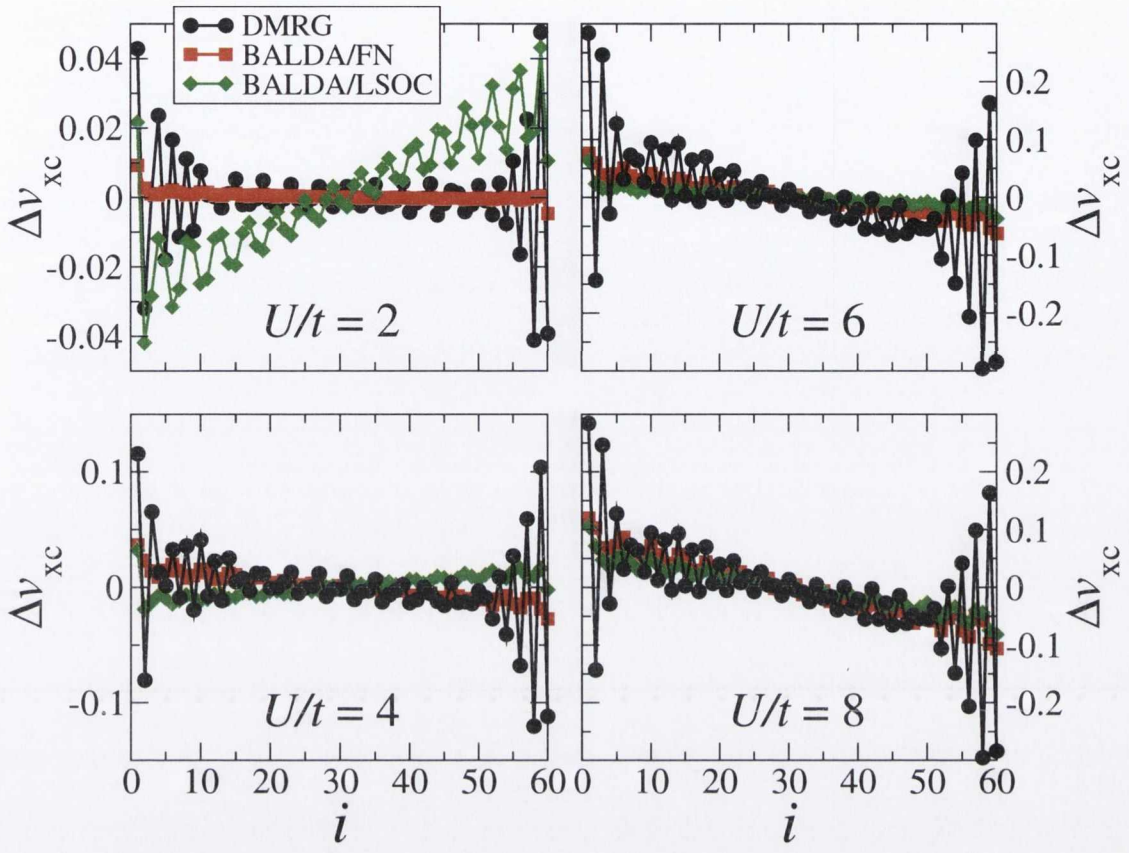

Figure 4.9: The difference, $\Delta v_{\rm xc}$, between the XC potential calculated at finite electric field and in absence of the field as a function of the site index. Results are presented for a 60 site chain with $N = 30$ ($n = 1/2$). The dots are the calculated data while the lines are a guide to the eye. The external potential has a negative slope.

note that for $n = 1/2$ and $U/t = 2$ the BALDA/FN $v_{\rm xc}$ is almost flat. This feature is promptly mirrored in the potential response of Figure 4.9, which also shows an almost flat $\Delta v_{\rm xc}$, although still with the correct negative slope.

Given the good agreement for both the polarizability and the potential response between the exact results and those obtained with the BALDA (in particular with the FN flavour), one can conclude that the local approximation to the Hubbard-LDFT functional is adequate. Still it is interesting to assess whether the remaining discrepancies have to do with the particular local parameterization of $E_{\rm XC}[\{n_i\}]$, or with the fact that the exact XC functional may be intrinsically non-local. In order to answer to this question we have set a numerical test. We consider a 60 site chain

with $n = 1/2$ (this should be long enough to resemble the infinite limit) and we introduce a local perturbation in half of the chain. This is in the form of a reduction of the on-site energy of the first 30 sites by δ. We then calculate the deviation of the XC potential per site, $\delta v/L$, as a function of the deviation of the total energy δE_0. These two quantities are defined respectively as

$$\frac{\delta v}{L} = \frac{1}{L}\sum_{i=1}^{L} |v_{\rm XC}^{\delta}(n_i) - v_{\rm XC}^{\delta=0}(n_i)| \,, \quad \delta E_0 = E_0(\delta) - E_0(0) \,, \tag{4.12}$$

with $v_{\rm XC}^{\delta}$ and $E_0(\delta)$ respectively the XC potential at site i and the total energy calculated for $\delta \neq 0$. One then expects for a local potential that $\delta v \to 0$ as $\delta E_0 \to 0$.

Our results are presented in figure 4.10. These have been obtained for a relatively small $U/t = 2$ by varying δ in the range $0 \leq \delta \leq 0.1$ in steps of 10^{-5} (this range is used only for small δ, while a coarse mesh is employed for large δ). Interestingly we note that, after a steady decrease of $\delta v/L$ with reducing δE_0, the deviation of the potential starts to fluctuate independently on the size of δE_0. We have carefully checked that such fluctuations are well within our numerical accuracy, so that they should be attributed to the breakdown of the local approximation.

In order to rule out possible local effects we have evaluated $\delta v/L$ by: i) summing over all the site in the chains (Case A in figure 4.10), ii) summing only over the first three sites in the left-hand side of the chain and the last three in the right-hand side (Case B), iii) summing over the first three sites on each side adjacent to the potential discontinuity (Case C). We find the rather remarkable result that, although for large δE_0 the three methods give a rather different $\delta v/L$, they provide the same deviation as the total energy differences approaches zero.

We then conclude that part of the failure of BALDA/FN in describing the polarizability of finite 1D chains must be ascribed to the violation of the local approxima-

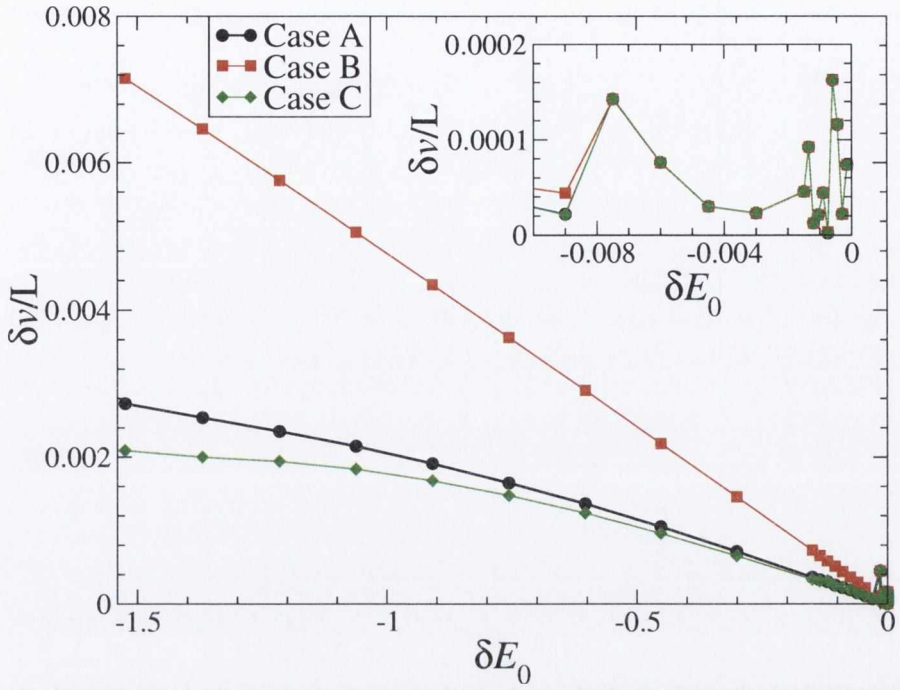

Figure 4.10: Variation of the XC potential per site, $\delta v/L$, as a function of the variation of the total energy, δE_0, for a 60 site chain in which the first 30 sites have an on-site energy lower by δ with respect to the remaining 30. The variation are calculated with respect to the homogeneous case. Three methods have been adopted to evaluate $\delta v/L$: Case A, summing over all the site in the chains; Case B, summing only over the first three sites in the left-hand side of the chain and the last three in the right-hand side; Case C, summing over the first three sites on each side adjacent to the potential discontinuity. The inset shows a magnification of the data for small δE_0.

tion. We note that this feature does not seem to be specific of the one-dimensional case and that a similar numerical test has been already provided in three-dimensions [112].

4.4 Summary

In this chapter, we report a systematic study of the energetics and the electrical response properties of one-dimensional metals described by the Hubbard model. This is solved within LDFT and local approximations of the exchange and correlation functional. Whenever possible the calculations are compared with exact results ob-

tained either by exact diagonalization or with the density matrix renormalization group approach. Our calculations indicate that the ground state energies extracted are in very good agreement with the ones computed by ED and DMRG over a broad range of parameters and are applicable to both the PBC and OBC. In general we find that BALDA functionals perform rather well in describing the electrical polarizability of finite one-dimensional chains. The agreement with exact results is particularly good in the case of numerically evaluated functionals. A similar good agreement is found for the exchange and correlation potential response. In this case we obtain the interesting result that the potential response is always along the same direction of the perturbing potential, in contrast to what happens in *ab initio* DFT. Furthermore for small electron filling and weak Coulombic interaction the commonly used LSOC parameterization is qualitatively incorrect due to a spurious minimum in the potential as a function of the site occupation.

We expect our results to be largely maintained even in the presence of impurities, i.e. when the external potential (the on-site energy) is not uniform across the chains. In this case deviations between the exact results and LDFT are expected for small U/t, where the potential has a qualitative incorrect response and for any U/t at an average site occupation close to half-filling, where the potential derivative discontinuity appears.

Finally we provide a numerical test of the breakdown of the local approximation being the source of the remaining errors.

Chapter 5

Current-lattice density functional theory for the one-dimensional Hubbard model

5.1 Introduction

Quantum dots, routinely made by electrostatically confining a two-dimensional electron gas [113], have been extensively studied in recent years [17]. The interest in these low-dimensional structures stems from the fact that their physics is controlled by quantum effects. Furthermore, while sharing many similarities with real atoms, quantum dots manifest intriguing low-energy quantum phenomena specific to them. This is because their properties can be influenced by external factors such as the geometry, the shape of the confining potential and the application of external fields, which are not accessible in real atoms. Research in the past has been motivated by the possibility of developing novel quantum dot based devices in both the fields of quantum cryptography/computing [114] and spintronics [115], as well as by the simple curiosity of exploring the properties of many-electron systems in reduced dimensions.

Quantum rings represent a particular class of quantum dots [116, 117], where electrons are confined in circular regions [118, 119]. The circular geometry can sustain an electrical current, which in turn can be induced by threading a magnetic flux across the ring itself. Such a magnetic flux produces exciting effects like Ahanorov-Bohm (AB) oscillations [120, 121] and persistent currents [122]. The effects were anticipated as early as the late 1960s [123, 124]. In one dimension the persistent current has been thoroughly studied [122, 125]. This, as well as many other physical properties of the ring, are a periodic function of the magnetic flux quantum, $\Phi_0 = hc/e$ (h is the Planck's constant, c the speed of light and e the electron's charge).

A number of earlier theoretical studies [126, 127, 128, 129, 130] on persistent current focused on unveiling the role of electron correlations and disorder over the electron transport. This is justified by the fact that electronic correlation in one-dimension (1D) always leads to non-fermionic low-energy quasiparticle excitations. In fact, even in the presence of weak interaction, 1D fermions behave differently from a Fermi liquid and their ground state is generally referred to as Luttinger liquid. This possesses specific collective excitations [131].

There are two theoretical frameworks commonly used to study finite 1D rings [132]. The first is based on the continuum model, where electrons move in a uniform neutralizing positive background and they interact via standard Coulomb repulsion ($e^2/4\pi\varepsilon_0 r$, ε_0 is the vacuum permittivity). The second is populated by lattice models, where the electronic structure is written in a tight-binding form and electron-electron interaction is commonly described at the level of Hubbard Hamiltonian [21]. In both frameworks Exact Diagonalization (ED) has been the preferential solving strategy for small systems (small number of sites and electrons) [129, 133]. Additional methods used to study quantum rings include, for the lattice models, Bethe Ansatz (BA) [58, 45], renormalization group (RG) [134] and density matrix renormalization group (DMRG) [135]. In contrast the continuum model has been tackled

with self-consistent Hartree Fock techniques [136], Bosonization schemes [137], conformal field theory [138], current-spin density functional theory [139] and quantum monte carlo (QMC) [140].

Many of the methods developed for solving lattice models for interacting electrons suffer from a number of intrinsic limitations connected to either the large computational overheads or to the need of using a drastically restricted Hilbert space. Density functional theory (DFT) can be a natural solution to these limitations. In Chapter 4, we have demonstrated that LDFT within the local approximation is a powerful and efficient scheme. Such a scheme was applied successfully to a wide range of situations [35, 37, 38, 39, 40, 41, 141].

LDFT can be further extended to include the action of a vector potential, i.e. it can be used to tackle problems where a magnetic flux is relevant. This effectively corresponds to the construction of current-lattice DFT (CLDFT). Such an extension of LDFT was proposed recently for one-dimensional spinless fermions with nearest-neighbor interaction [142] and it is here adapted to the repulsive Hubbard model. The newly constructed functional is then used to investigate total energies, persistent current and Drude weight of a mesoscopic repulsive Hubbard ring threaded by a magnetic flux.

We begin the chapter by reviewing the concepts of persistent current and Drude weight in a one-dimensional mesoscopic systems. We then outline analytical solutions of the Schrödinger equation of a ring in a magnetic flux, neglecting electron-electron interactions and spin. Next we review the tight binding approach of a ring with a vector potential both for the non-interacting and interacting cases in the lattice models. The BA technique is summarized for the homogeneous Hubbard ring and how this can be used to obtain charge stiffness. Finally, the theoretical foundations leading to the construction of CLDFT and to its LDA are reviewed. Our results for both homogeneous and defective rings are presented, highlighting the main capabilities

and limitations of our scheme.

5.2 Persistent current and charge stiffness of a 1D mesoscopic system

In mesoscopic physics, the interesting phenomenon of persistent current is displayed by a metallic ring threaded by AB magnetic flux. A schematic representation of the system is shown in Figure 5.1. In general, an electron passing through a ring structure but not entering the region of the magnetic flux moves round the ring without any (classical) force during its motion. The quantum wave representing the state of the electron is, however, affected by the magnetic field threading around the ring. The electron's wavefunction, Ψ, experiences a phase shift as a result of the enclosed field, Φ, so that by a gauge transformation the magnetic field is eliminated from the Hamiltonian leading to a modification of its boundary condition:

$$\Psi(\Phi + 2\pi) = \Psi(\Phi)e^{i2\pi\Phi/\Phi_0}, \tag{5.1}$$

Φ_0 is usually set to unity. This is the so-called twisted boundary condition responsible for the oscillation of both thermodynamic and kinetic properties with the magnetic flux. At absolute temperature ($T = 0$), the persistent current, j, can be measured as the response of the ground state energy, E_0, to the finite AB flux for a finite system on a ring of length L. It is usually calculated from the expression [144],

$$j = L\frac{\partial E_0(\Phi)}{\partial \Phi}. \tag{5.2}$$

Due to the twisted boundary condition, the ground state energy has a periodicity of 2π in Φ, i.e.

$$E_0(\Phi + 2\pi) = E_0(\Phi) = E_0(-\Phi). \tag{5.3}$$

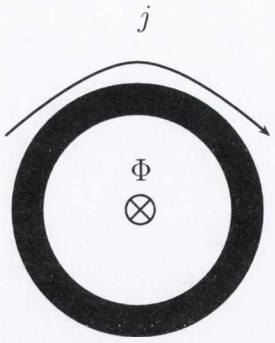

Figure 5.1: Schematic representation of one-dimensional ring threaded by a magnetic flux Φ. A persistent current j is generated in the ring.

The energy shift in the ground state can be written, using perturbation theory, as [145, 146]

$$E_0(\Phi) - E_0(0) \equiv D\Phi^2/L + O(\Phi^4), \tag{5.4}$$

where

$$D \equiv \frac{L}{2}\frac{\partial^2 E_0(\Phi)}{\partial \Phi^2}|_{\Phi=0} \tag{5.5}$$

is called the stiffness constant or the Drude weight [151]. For small values of the flux, D and j are related as

$$j = 2D\Phi. \tag{5.6}$$

The inclusion of higher order terms in equation (5.4) will be crucial when the energy shift is comparable to the mean energy level spacing in the spectrum of the many-body system. In particular, for a finite 1D metallic system, the gaps are of the order of $\mathcal{O}(1/L)$ and thus non-quadratic corrections occur when Φ is $\mathcal{O}(1)$. Therefore level crossing would occur and perturbation theory would break down for Φ of order π [146, 148].

There are 2 degrees of freedom possible when the AB flux is spin dependent in a system. In the case where up spin and down spin AB flux are equal i.e. $\Phi_\uparrow = \Phi_\downarrow = \Phi_c$, the shift in energy gives the charge stiffness, D_c. For zero magnetization ($m = 0$), the other possibility is when $\Phi_\uparrow = -\Phi_\downarrow = \Phi_s/2$ in which the energy shift gives the

spin stiffness, D_s. Charge and spin current can therefore be written as

$$\begin{aligned} j_\upsilon &= 2D_\upsilon \Phi_\upsilon, \\ D_\upsilon &= \frac{L}{2}\frac{\partial^2 E_0(\Phi_\upsilon)}{\partial \Phi_\upsilon^2}|_{\Phi_\upsilon=0}, \end{aligned} \tag{5.7}$$

$\upsilon = c, s$.

In this work, we will only consider the former case. This is because D_c defines the magnitude of the real part of optical conductivity, $\sigma_1(w)$, in the long wavelength limit [145, 148]. For finite systems, the real part of the conductivity is usually separated as the sum of a zero frequency delta peak and a finite frequency regular part. D_c is the weight of the zero frequency delta peak:

$$\sigma_1(w) = 2\pi D_c \delta(w) + \sigma_1^{\text{reg}}(w), \tag{5.8}$$

where $\hbar = e = c = 1$ and $\sigma_1^{\text{reg}}(w)$ is the "regular" part of the conductivity.

5.3 The Hamiltonian of a quantum ring with a vector potential

The non-interacting one-dimensional (spinless) electron gas on a ring is a system whose equation of motion has a known analytical solution. Its Schrödinger equation is written as

$$\frac{\hat{p}^2}{2m}\psi_n(x) = \varepsilon_n \psi_n(x). \tag{5.9}$$

Using PBC, i.e $\psi(x) = \psi(x + L)$, the solutions are plane waves with wave vectors $k_n = \frac{p_n}{\hbar}$ given by

$$k_n = (\frac{2\pi}{L})n \tag{5.10}$$

where n is an integer.

In the presence of a vector potential, A, the momentum operator, $\hat{p} \rightarrow \hat{p} + \frac{e}{c}\hat{A}$ and A is related to a constant magnetic field, B, perpendicular to the ring as follows:

$$A = \frac{Br}{2} = \frac{BL}{4\pi}. \tag{5.11}$$

L ($2\pi r$) is the length of the ring and r is its radius. The magnetic flux is given as

$$\Phi = \int Adl = AL = \frac{BL^2}{4\pi}, \tag{5.12}$$

so that

$$k_n = (\frac{2\pi}{L})n + \frac{e}{\hbar c}A = \frac{2\pi}{L}(n + \frac{\Phi}{\Phi_0}). \tag{5.13}$$

The energy levels $\varepsilon_n = \hbar^2 k_n^2/2m$ are therefore a set of translated parabolas which are periodic in Φ with period $\Phi_0 = hc/e$.

In general a vector potential, $\vec{A}$, enters into a lattice model via Peierls substitution [149, 150], where the matrix elements of the $\vec{A}$-dependent Hamiltonian, $H(\vec{r}, \vec{p} + \frac{e}{c}\vec{A})$, can be written in terms of those for $\vec{A} = 0$ as

$$\langle \vec{R}'|H(\vec{r}, \vec{p} + \frac{e}{c}\vec{A})|\vec{R}\rangle = \langle \vec{R}'|H(\vec{r}, \vec{p})|\vec{R}\rangle \mathrm{e}^{-\frac{ie}{\hbar c}\int_{\vec{R}}^{\vec{R}'} \vec{A}\cdot \mathrm{d}\vec{s}}, \tag{5.14}$$

where $|\vec{R}\rangle$ is the generic orbital located at the position $\vec{R}$ and belonging to the basis set (orthogonal) used to construct the tight-binding Hamiltonian.

When Peierls substitution is applied, the kinetic energy $\hat{T}$ is modified. This takes the form

$$\hat{T} = -t \sum_{\sigma,\, l=1}^{L-1} (e^{-i\Phi_{\sigma l}/L}\, \hat{c}^{\dagger}_{\sigma,\, l+1}\hat{c}_{\sigma,\, l} + hc)\,, \tag{5.15}$$

where we have considered a system comprising L atomic sites. In equation (5.15) $\hat{c}^{\dagger}_{\sigma,\, l}$ ($\hat{c}_{\sigma,\, l}$) is the creation (annihilation) operator for an electron of spin σ ($\sigma = \uparrow, \downarrow$) at the l-site, t is the hopping integral and $\Phi_{\sigma l}$ is the phase associated to the l-th bond,

which effectively describes the action of $\vec{A}$.

The inclusion of the interaction term defines the homogeneous 1D Hubbard Hamiltonian:

$$\hat{H}_U^{\Phi} = \hat{T} + \hat{U}, \tag{5.16}$$

where the Coulomb repulsion term is $\hat{U} = U \sum_{l=1}^{L} \hat{n}_{\uparrow l} \hat{n}_{\downarrow l}$, with U being the Coulomb repulsion energy and $\hat{n}_{\sigma l} = \hat{c}_{\sigma l}^{\dagger} \hat{c}_{\sigma l}$. In order to extract transport properties, the functional form of the ground state energy as a function of the flux is investigated. We then study this functional form using the BA technique and CLDFT. In this work, we do not use the DMRG scheme because it is well known that DMRG performs poorly for periodic boundary conditions [28, 93].

5.3.1 BA technique for a homogeneous Hubbard ring with a magnetic flux

The addition of Φ_σ to $\hat{H}_U$ of equation (2.5) does not affect its integrability via the BA equations. Here the flux can be gauged out of the Hamiltonian so that the solution to the Schrödinger equation in the presence of the flux with periodic boundary condition is the same as that in the absence of the flux but with a twisted boundary condition for the wavefunctions [152], i.e.

$$\Psi(x_1, x_2, ..., x_i + L, ...) = e^{i\Phi_\sigma} \Psi(x_1, x_2, ..., x_i, ...). \tag{5.17}$$

The solutions to $\hat{H}_U^{\Phi}$ using the BA for any given Φ_σ are similar to the transcendental equations of (2.28) with additions of appropriate Φ_σ [148]:

$$Lk_j = 2\pi I_j + \Phi_\uparrow + 2 \sum_{\beta=1}^{M} \tan^{-1}\left(\frac{\lambda_\beta - \sin k_j}{U/4}\right), \tag{5.18}$$

$$2\sum_{j=1}^{N}\tan^{-1}(\frac{\lambda_\alpha - \sin k_j}{U/4}) = 2\pi J_\alpha + \Phi_\downarrow - \Phi_\uparrow + 2\sum_{\beta=1}^{M}\tan^{-1}(\frac{\lambda_\alpha - \lambda_\beta}{U/2}), \tag{5.19}$$

where M is the number of spin down electrons and N is the number of electrons. The quantum numbers $\{I_j\}$ and $\{J_\alpha\}$ are connected with charge and spin degrees of freedom respectively [45] and are integers or half-odd integers depending on the parity of N and M. For example, at zero magnetic field they have the following form: when $N = 2K$ (an even number), then

$$\begin{aligned} I_1, ..., I_{2K} &= -K, -(K-1), ..., -1, 0, 1, ..., K-1 \\ J_1, ..., J_M &= -\frac{1}{2}(M-1), ..., -\frac{1}{2}, \frac{1}{2}, ..., \frac{1}{2}(M-1) \end{aligned} \tag{5.20}$$

where M is also an even number; and

$$\begin{aligned} I_1, ..., I_{2K} &= -K + \frac{1}{2}, ..., -\frac{1}{2}, \frac{1}{2}, ..., K - \frac{1}{2} \\ J_1, ..., J_M &= -\frac{1}{2}(M-1), ..., -1, 0, 1, ..., \frac{1}{2}(M-1) \end{aligned} \tag{5.21}$$

where M is also an odd number. If $N = 2K + 1$ (an odd number) then

$$\begin{aligned} I_1, ..., I_{2K+1} &= -K, ..., -1, 0, 1, ..., K \\ J_1, ..., J_M &= -\frac{1}{2}M, ..., -1, 0, 1, ..., \frac{1}{2}M - 1 \end{aligned} \tag{5.22}$$

when M is an even number, and

$$\begin{aligned} I_1, ..., I_N &= -\frac{1}{2}N, ..., -\frac{1}{2}, \frac{1}{2}, ..., \frac{1}{2}N \\ J_1, ..., J_M &= -\frac{1}{2}M, ..., -\frac{1}{2}, \frac{1}{2}, ..., \frac{1}{2}M \end{aligned} \tag{5.23}$$

when M is an odd number. However, in the presence of magnetic flux these numbers can be shifted by an integer. The optimal set is determined from the minimum of the total energy of N electrons with M down spins [153]. The ground state energy,

E_0, is therefore given by

$$E_0(\Phi) = -2t \sum_{j=1}^{N} \cos k_j. \tag{5.24}$$

In the thermodynamic limit, many physical properties of the Hubbard model in 1D can be solved by using the quasi-particle dispersions of the BA formalism [19, 154]. This was first described by Frahm and Korepin [154] where they expressed the integral equations for these dispersions as

$$\begin{aligned} \varepsilon_c^{QP}(k) =& \varepsilon_c^{(0)}(k) + \int_{-B}^{B} d\lambda \varepsilon_s^{QP}(\lambda) K_1(\sin k - \lambda), \\ \varepsilon_s^{QP}(\lambda) = \varepsilon_s^{(0)}(\lambda) &+ \int_{-Q}^{Q} dk \cos(k) \varepsilon_c^{QP}(k) K_1(\sin k - \lambda) - \int_{-B}^{B} d\lambda' \varepsilon_s^{QP}(\lambda') K_2(\lambda - \lambda'), \end{aligned} \tag{5.25}$$

where the bare energies $\varepsilon_{c,s}^{(0)}(k)$ are

$$\begin{aligned} \varepsilon_c^{(0)}(k) =& -\mu - 2t\cos(k), \\ \varepsilon_s^{(0)}(k) =& 0 \end{aligned} \tag{5.26}$$

and μ is the chemical potential while $K_1(\sin k - \lambda)$ and $K_2(\lambda - \lambda')$ are as defined in (2.32). In order to fix the values of B and Q for any filling,

$$\begin{aligned} \varepsilon_c^{QP}(-Q) =& \varepsilon_c^{QP}(Q) \\ \varepsilon_s^{QP}(-B) =& \varepsilon_s^{QP}(B), \end{aligned} \tag{5.27}$$

and the chemical potential is determined from the condition

$$\max_{\{k\}}[\varepsilon_c^{QP}(k)] = 0. \tag{5.28}$$

The ground state energy can be calculated from the dispersion using

$$\frac{E_0 - \mu N}{L} = \int_{-Q}^{Q} \frac{dk}{2\pi} \varepsilon_c^{QP}(k) \tag{5.29}$$

Also, the velocity of the charge excitation is given by

$$v_c = \frac{1}{2\pi\rho(Q)}\{\varepsilon_c^{QP}\}'(Q) \tag{5.30}$$

where

$$\{\varepsilon_c^{QP}\}'(Q) = \frac{\partial\varepsilon_c^{QP}}{\partial k}|_{k=Q}, \tag{5.31}$$

and $\rho(k)$ is defined by (2.31).

In order to describe transport properties, a useful quantity called the dressed charge function, $\xi_c(k)$, [19, 154] is needed. It is defined via the following coupled integral equations:

$$\begin{aligned} \xi_c(k) =& 1 + \int_{-B}^{B} d\lambda \xi_s(\lambda) K_1(\sin k - \lambda), \\ \xi_s(\lambda) =& \int_{-Q}^{Q} dk \cos(k) \xi_c(k) K_1(\sin k - \lambda) - \int_{-B}^{B} d\lambda' \xi_s(\lambda') K_2(\lambda - \lambda'). \end{aligned} \tag{5.32}$$

For instance, the charge stiffness, D_c, can be written [155] as

$$D_c = \frac{1}{2\pi}[\xi_c(Q)]^2 v_c. \tag{5.33}$$

This equation will be used to construct the XC potential within the CLDFT framework in the following section.

5.3.2 Current-lattice density functional theory

We begin by outlining a general theoretical foundation of the current-density functional theory (CDFT) and then describe its lattice counterpart for a one-dimensional homogeneous Hubbard model.

In the presence of an external vector potential $\vec{A}(\vec{x})$ (related to an external magnetic field by $\vec{B}(\vec{x}) = \vec{\nabla} \times \vec{A}(\vec{x})$), the non-relativistic Hamiltonian for N electrons

contains both linear and quadratic terms of the potential i.e.

$$\hat{H} = \sum_{i}^{N} \left[\frac{1}{2} \left\{ -\vec{\nabla}_i + \vec{A}(\vec{x}) \right\}^2 + v(\vec{x}_i) \right] + \sum_{j>i}^{N} \frac{1}{\vec{x}_{ij}}. \tag{5.34}$$

Equation (5.34) is gauge-invariant i.e. if $\vec{A}(\vec{x})$ is changed to $\vec{A}(\vec{x}) + \nabla\Lambda(\vec{x})$, where $\Lambda(\vec{x})$ is an arbitrary smooth function of position and simultaneously multiply the wavefunction by a phase factor $exp[-i\sum_i \Lambda(\vec{x}_i)]$, then all the physically observable properties of the system would remain unchanged [156]. This is intuitively valid because the transformation does not alter the magnitude of the magnetic field. Due to this additional potential, there is an additional density introduced in the *ab initio* DFT, namely the paramagnetic current density $\vec{j}_p(\vec{x})$. The main idea of CDFT is therefore to use the expectation values of the charge density and paramagnetic current density as the fundamental quantities.

It has been shown by Vignale and Rasolt [157, 158] that it is possible to extend Hohenberg-Kohn (HK) theorems and establish a one-to-one mapping between the potentials $v(\vec{x}_i)$ and $\vec{A}(\vec{x})$ and the ground state densities $n(\vec{x})$ and $\vec{j}_p(\vec{x})$ respectively. Thus, the ground state densities uniquely determine the ground state wavefunction of the system. Consequently, any observable of a system in its ground-state is a functional of the these densities. It is then possible to define an energy functional

$$E[n, \vec{j}_p] = \mathcal{F}[n, \vec{j}_p] + \int d\vec{x} n(\vec{x}) \left[v(\vec{x}) + \frac{1}{2}\vec{A}^2(\vec{x}) \right] + \int d\vec{x} \vec{j}_p \vec{A}(\vec{x}), \tag{5.35}$$

where the universal functional $\mathcal{F}[n(\vec{x}), \vec{j}_p(\vec{x})]$ is given as

$$\mathcal{F}[n, \vec{j}_p] = \min_{n, \vec{j}_p} \langle \Psi | \hat{\mathcal{T}} + \hat{\mathcal{U}} | \Psi \rangle, \tag{5.36}$$

where $\hat{\mathcal{T}}$ and $\hat{\mathcal{U}}$ are as defined by equation (2.40).

Equally important is the fact that the standard Kohn-Sham construction can

be also employed for CDFT, so that the many-body problem can be mapped onto a fictitious single-particle one, with the two sharing the same ground state n and $\vec{j}_p$ [157, 158]. The XC energy functional can be written in terms of an auxiliary single-particle universal functional $\mathcal{F}_s[n(\vec{x}), \vec{j}_p(\vec{x})]$ as follows:

$$E_{xc} \equiv \mathcal{F}[n(\vec{x}), \vec{j}_p] - \mathcal{F}_s[n(\vec{x}), \vec{j}_p(\vec{x})] - E_H[n(\vec{x})] \tag{5.37}$$

One then seeks effective potentials $v_s(\vec{x})$ and $A_s(\vec{x})$ that yield the correct ground state density and current via the solution of the single particle equation:

$$\left[\frac{1}{2}\{-i\vec{\nabla} + \vec{A}_s(\vec{x})\}^2 + v_s(\vec{x})\right] \Phi_\alpha(\vec{x}, \sigma) = \varepsilon_\alpha \Phi_\alpha(\vec{x}, \sigma). \tag{5.38}$$

where

$$\begin{aligned} n(\vec{x}) =& \sum_{\alpha,\sigma} |\Phi_\alpha(\vec{x}, \sigma)|^2 \\ \vec{j}_p(\vec{x}) =& \Im \sum_{\alpha,\sigma} \Phi^*_\alpha(\vec{x}, \sigma) \vec{\nabla} \Phi_\alpha(\vec{x}, \sigma). \end{aligned} \tag{5.39}$$

The single-particle vector potential, $\vec{A}_s(\vec{x})$) and effective potential, $v_s(\vec{x})$ are defined as

$$\begin{aligned} \vec{A}_s(\vec{x}) =& \vec{A}(\vec{x}) + \vec{A}_{xc}(\vec{x}) \\ v_s(\vec{x}) =& v(\vec{x}) + v_H(\vec{x}) + v_{xc}(\vec{x}) + f(\vec{A}_{xc}(\vec{x}), \vec{j}_p(\vec{x}), n(\vec{x})), \end{aligned} \tag{5.40}$$

where

$$\begin{aligned} \vec{A}_{xc}(\vec{x}) =& \frac{\delta E_{xc}[n(\vec{x}), \vec{j}_p(\vec{x})]}{\delta \vec{j}_p(\vec{x})} \\ v_{xc}(\vec{x}) =& \frac{\delta E_{xc}[n(\vec{x}), \vec{j}_p(\vec{x})]}{\delta n(\vec{x})}, \end{aligned} \tag{5.41}$$

and $f(\vec{A}_{xc}(\vec{x}), \vec{j}_p(\vec{x}), n(\vec{x}))$ is a function that depends on the $\vec{A}_{xc}(\vec{x}), \vec{j}_p(\vec{x})$ and $n(\vec{x})$. The difficult step in the CDFT formalism is as always constructing a good approximation to both $\vec{A}_{xc}(\vec{x})$ and $v_{xc}(\vec{x})$. Once those are constructed, one just solves the self-consistent KS-type equations of (5.38) the same manner as done for DFT.

The scope of this work is to describe how *ab initio* CDFT can be translated to lattice models and how a suitable approximation for the 1D Hubbard Hamiltonian can be constructed. Our description follows closely the one previously given by Dzierzawa *et. al.* [142]. The one-dimensional Hamiltonian we shall consider is represented by

$$\hat{H}^{\Phi}_{MB} = \hat{H}^{\Phi}_{U} + \sum_{l}^{L} v_l^{ext} \hat{n}_l, \tag{5.42}$$

where $\hat{H}^{\Phi}_{U}$ is given by the equation (5.16) and $\{v_l^{\text{ext}}\}$ is the external potential.

Throughout this work we always consider the non-spin polarized case so that $\Phi_{\uparrow l} = \Phi_{\downarrow l} = \Phi_l$ and $n_{\uparrow l} = n_{\downarrow l} = n_l$. The first step in the construction of a CLDFT is the formulation of the problem in a functional form. The basic variables of the theory are the site occupation $n_l = \langle \Psi | \hat{n}_l | \Psi \rangle$ and bond paramagnetic current, $j_l = \langle \Psi | \hat{j}_l | \Psi \rangle$, where $|\Psi\rangle$ is the many-body wavefunction and the paramagnetic current operator is defined as

$$\hat{j}_l = -it(e^{-i\Phi_l/L}\, \hat{c}^{\dagger}_{l+1\sigma} \hat{c}_{l\sigma} - hc) \tag{5.43}$$

In complete analogy to *ab initio* CDFT we can write the total energy, E, of the Hamiltonian (5.42) as a functional of the local external potentials and phases

$$E = \mathcal{F} + \sum_{l} v_l^{\text{ext}} n_l + \sum_{l} \Phi_l j_l, \tag{5.44}$$

so that

$$\begin{aligned} n_l = \langle \hat{n}_l \rangle &= \frac{\partial E}{\partial v_l^{\text{ext}}}\,, \\ j_l = \langle \hat{j}_l \rangle &= \frac{\partial E}{\partial \Phi_l}\,. \end{aligned} \tag{5.45}$$

$\mathcal{F}[n_l, j_l]$ is a U dependent universal functional, whose functional derivatives with

respect to $\{n_l\}$ and $\{j_l\}$ satisfy the following two equations

$$\begin{aligned} v_l^{\text{ext}} &= -\frac{\partial \mathcal{F}}{\partial n_l} \\ \Phi_l &= -\frac{\partial \mathcal{F}}{\partial j_l}. \end{aligned} \tag{5.46}$$

Note that equations (5.44) through (5.46) follow directly from the properties of the Legendre transformation.

In order to make the theory practical we have now to introduce the auxiliary single-particle Kohn-Sham system. This is described by a single-particle Hamiltonian, $\hat{H}^{\text{s}}$, whose ground state site occupation and paramagnetic current are identical to those of the interacting system [equation (5.42)]. $\hat{H}^{\text{s}}$ reads

$$\hat{H}^{\text{s}} = \hat{T}^{s} + \sum_{l}^{L} v_l^s \hat{n}_l, \tag{5.47}$$

where $\hat{T}^{\text{s}} = -t \sum_{\sigma,l=1}^{L-1} (e^{-i\Phi_l^{\text{s}}/L}\, \hat{c}_{l+1\sigma}^{\dagger} \hat{c}_{l\sigma} + hc)$ and the associated local effective potentials and phases are v_l^{s} and Φ_l^{s} respectively. The single-particle Schrödinger equation is then

$$\hat{H}^{\text{s}} |\Psi_\alpha^{\text{s}}\rangle = \epsilon_\alpha |\Psi_\alpha^{\text{s}}\rangle, \tag{5.48}$$

and the site occupation is defined as

$$n_l^{\text{s}} = \sum_{\alpha} f_\alpha \langle \Psi_\alpha^{\text{s}} | \hat{n}_l | \Psi_\alpha^{\text{s}} \rangle \,, \tag{5.49}$$

where f_α is the occupation number. An analogous expression can be written for j_l^{s}.

The energy functional associated the Kohn-Sham system, $\mathcal{F}^{\text{s}}$, can be constructed by performing again a Legendre transformation

$$\mathcal{F}^{\text{s}} = E^{\text{s}} - \sum_{l} v_l^{\text{s}} n_l^{\text{s}} - \sum_{l} \Phi_l^{\text{s}} j_l^{\text{s}} \,, \tag{5.50}$$

where E^{s} is the total energy of the single-particle system and the following two equations are valid

$$\begin{aligned} v_l^{\mathrm{s}} &= -\frac{\partial \mathcal{F}^{\mathrm{s}}}{\partial n_l^{\mathrm{s}}} \\ \Phi_l^{\mathrm{s}} &= -\frac{\partial \mathcal{F}^{\mathrm{s}}}{\partial j_l^{\mathrm{s}}} \,. \end{aligned} \tag{5.51}$$

The crucial point is that in the ground state the real and the Kohn-Sham system share the same site occupation and paramagnetic current, i.e. $n_l = n_l^{\mathrm{s}}$ and $j_l = j_l^{\mathrm{s}}$.

Thus we are now in the position of defining the XC energy, E^{xc}, as the usual difference between $\mathcal{F}$ for the interacting and the Kohn-Sham systems, after the classical Hartree energy E^{H} has also been subtracted,

$$E^{\mathrm{xc}}[n_l, j_l] = \mathcal{F}[n_l, j_l] - \mathcal{F}^{\mathrm{s}}[n_l, j_l] - E^{\mathrm{H}}[n_l] \,. \tag{5.52}$$

Note that for all functionals in equation (5.52) we took the short notation $\{n_l\} \to n_l$ and $\{j_l\} \to j_l$, i.e. the functionals depend on all the on-site occupations and paramagnetic currents. This allows us to define the single-particle effective potentials and phases. One in fact just needs to take the functional derivative of equation (5.52) with respect to n_l and j_l, and use the equations (5.46) and (5.51) to obtain

$$\begin{aligned} v_l^{\mathrm{s}} &= v_l^{\mathrm{ext}} + v_l^{\mathrm{H}} + v_l^{\mathrm{xc}} \,, \\ \Phi_l^{\mathrm{s}} &= \Phi_l + \Phi_l^{\mathrm{xc}} \,, \end{aligned} \tag{5.53}$$

where

$$\begin{aligned} v_l^{\mathrm{xc}} &= \frac{\partial E_l^{\mathrm{xc}}}{\partial n_l} \,, \\ \Phi_l^{\mathrm{xc}} &= \frac{\partial E_l^{\mathrm{xc}}}{\partial j_l} \,, \end{aligned} \tag{5.54}$$

and $v_l^{\mathrm{H}} = \partial E_l^{\mathrm{H}} / \partial n_l$ $(= U n_l / 2)$ is the Hartree potential.

Finally we can re-write E^{xc} in terms of the expectation values of the original Hamiltonians. In fact by substituting the functional forms of $\mathcal{F}$ and $\mathcal{F}^{\mathrm{s}}$ into the

equation (5.52),

$$E^{\mathrm{xc}} = E - E^{\mathrm{s}} + \sum_l (v_l^{\mathrm{s}} - v_l^{\mathrm{ext}}) n_l + \sum_l (\Phi_l^{\mathrm{s}} - \Phi_l) j_l - E^{\mathrm{H}}[n_l] \,, \tag{5.55}$$

by using the equations (5.42) and (5.47),

$$\sum_l (v_l^{\mathrm{s}} - v_l^{\mathrm{ext}}) n_l = E^{\mathrm{s}} - E - \langle \Psi^{\mathrm{s}} | \hat{T}^{\mathrm{s}} | \Psi^{\mathrm{s}} \rangle + \langle \Psi | \hat{T} + \hat{U} | \Psi \rangle \,, \tag{5.56}$$

and again substituting equation (5.56) into equation (5.55), we obtain

$$E^{\mathrm{xc}} = \langle \Psi | \hat{T} + \hat{U} | \Psi \rangle - \langle \Psi^{\mathrm{s}} | \hat{T}^{\mathrm{s}} | \Psi^{\mathrm{s}} \rangle + \sum_l (\Phi_l^{\mathrm{s}} - \Phi_l) j_l - E^{\mathrm{H}}[n_l]. \tag{5.57}$$

Now that the theory has been formally established we need to find an appropriate approximation to E^{xc}. As for the case of standard LDFT [34, 35], the strategy here is that of considering the BA solution for the homogeneous limit of $\hat{H}_{MB}^{\Phi}$ (this is defined in equation (5.42) by setting $v_l = v$ and $\Phi_l = \Phi$) and then take its local density approximation $n \to n_l$, $\Phi \to \Phi_l$ [142], i.e.

$$E_{\mathrm{LDA}}^{\mathrm{xc}}[n_l, j_l] = \sum_l e^{\mathrm{xc}}[n_l, j_l], \tag{5.58}$$

where $e^{\mathrm{xc}} = E^{\mathrm{xc}}[n, j]/L$ is the XC energy density (per site) of the homogeneous system. The first term of the equation (5.57) can be calculated exactly using the BA procedure [148]. This will provide the ground state energy as a function of n and Φ, so that one still needs to re-express it in terms of n and j. However the phase variable Φ can be eliminated from the ground state energy by using

$$j = \frac{\partial E(n, \Phi)}{\partial \Phi} \,. \tag{5.59}$$

Thus one can finally explicitly write $e^{\mathrm{xc}}(n, j)$ (the full derivation for the 1D Hub-

bard Hamiltonian is presented in Appendix C)

$$e^{\mathrm{xc}}(n,j) = e^{\mathrm{xc}}(n,0) + \frac{1}{2}\Lambda^{\mathrm{xc}}(n)j^2, \tag{5.60}$$

where

$$\begin{aligned} e^{\mathrm{xc}}(n,0) =& \frac{E^{\mathrm{BA}}(n,0) - E^{0}(n,0) - E^{\mathrm{H}}(n)}{L}, \\ \Lambda^{\mathrm{xc}}(n) =& \frac{1}{2}\left[\frac{1}{D_c^0(n)} - \frac{1}{D_c^{\mathrm{BA}}(n)}\right]. \end{aligned} \tag{5.61}$$

In the equations above $E^0(n,0)$ and $D_c^0(n)$ are respectively the non-interacting ground state energy and charge stiffness, while $E^{\mathrm{BA}}(n,0)$ and $D_c^{\mathrm{BA}}(n)$ are the same quantities for the interacting case as calculated from the BA. Finally, the XC contributions to the Kohn-Sham potential can be obtained by simple functional derivative (in this case by simple derivative) of the exchange and correlation energy density with respect to the fundamental variables n and j, i.e.

$$v^{\mathrm{xc}}_{\mathrm{BALDA}}(n_l, j_l) = \frac{\partial e^{\mathrm{xc}}(n,j)}{\partial n}|_{n\to n_l, j\to j_l}, \tag{5.62}$$

and

$$\Phi^{\mathrm{xc}}_{\mathrm{BALDA}}(n_l, j_l) = \frac{\partial e^{\mathrm{xc}}(n,j)}{\partial j} = \Lambda^{\mathrm{xc}}(n)j|_{n\to n_l, j\to j_l}, \tag{5.63}$$

where BALDA, as usual, stands for Bethe Ansatz Local Density Approximation.

In the two panels of Figure 5.2 we present $e^{\mathrm{xc}}(n,0)$ and $\Lambda^{\mathrm{xc}}(n)$ as a function of the electron density, n, for different interaction strengths U/t. As in the case of standard LDFT also for CLDFT there is a divergence in the n-derivative of both $e^{\mathrm{xc}}(n,0)$ and $\Lambda^{\mathrm{xc}}(n)$ at half-filing ($n = 1$). This is in correspondence of the metal-insulator-transition present in the 1D Hubbard model for finite U/t. In the case of $\Lambda^{\mathrm{xc}}(n)$ the divergence is due to the vanishing limit of D_c^{BA} at half-filling.

The solution of the Kohn-Sham problem proceeds as follows. First an initial guess for the site occupation is used to construct the initial local paramagnetic current den-

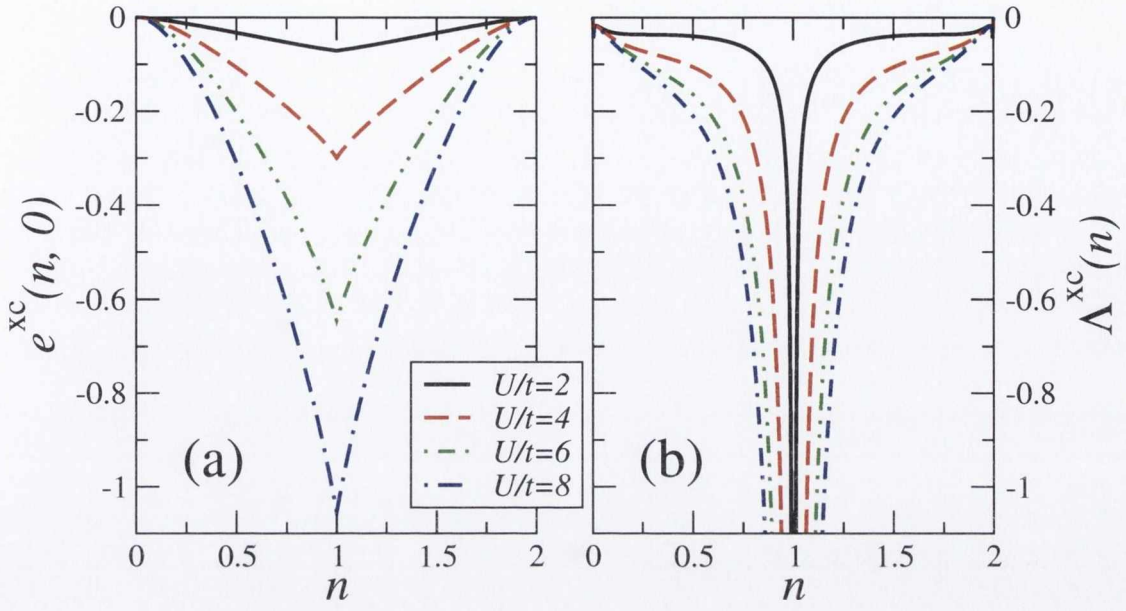

Figure 5.2: The XC energy density (per site) for a homogeneous 1D Hubbard ring threaded by a magnetic flux as a function of the electron density and for different values of interaction strength U/t: (a) $e^{xc}(n, 0)$ and (b) $\Lambda^{xc}(n)$.

sity. Then, the functional derivatives of equations (5.62) and (5.63) are evaluated at these given n and j so that the Kohn-Sham potential is constructed. The Kohn-Sham equations are then solved to obtain the new set of Kohn-Sham orbitals from which the new orbitals occupations are evaluated via the equation (5.49). The procedure is then repeated until self-consistency is reached, i.e. until the potentials (or the densities) at two consecutive iterations vary below a certain threshold. After convergence is achieved the total energy for the interacting system is calculated from

$$E = \sum_{\alpha} f_{\alpha}\epsilon_{\alpha} + E^{\mathrm{xc}}[n_l, j_l] - E^{\mathrm{H}}[n_l] - \sum_{l} v_l^{\mathrm{xc}} n_l, \tag{5.64}$$

where the first term is the sum of single-particle energies and the other terms are the so-called *double counting* corrections.

5.4 Results and Discussion

We now discuss how CLDFT performs in describing both the energetics and the transport properties of 1D Hubbard rings in presence of a magnetic flux. For small rings our results will be compared with those obtained by diagonalizing exactly the Hamiltonian of equation (5.42), while CLDFT for large rings will be compared with the BA solution. First we will consider homogeneous rings and then we will explore the single impurity problem.

5.4.1 Homogeneous Ring

In this section we focus our attention on discussing the general features of CLDFT applied to homogeneous Hubbard rings threaded by a magnetic flux, i.e. on the performance of CLDFT in describing the Ahanorov-Bohm effect. We start our analysis by comparing the CLDFT results with those obtained by ED. Since ED is numerically intensive such a comparison is limited to small systems.

In figure 5.3 we present the first low-lying energy levels, E, calculated by ED as a function of the magnetic flux, Φ, for a small 12-site ring at quarter filling ($n = 1/2$). In particular we present results for the non-interacting case [panel (a)] and for the interacting one at three different interaction strengths: (b) $U/t = 2$, (c) $U/t = 4$ and (d) $U/t = 6$. Exact results (ED) are in black, while those obtained with CLDFT in red. In general the ground state energy is minimized at $\Phi = 0$ when the number of electrons is $N = 4m + 2$ and at $\Phi = \pi$ for $N = 4m$, with m being an integer [159]. Here we consider the case $N = 4m + 2$ where the ground state is a singlet [145].

For non-interacting electrons the ground state is a singlet and the total energy is a parabolic function of Φ. Also the various excited states have a parabolic dependence on Φ and simply correspond to single-particle levels with different wave-vectors. As the Coulomb interaction is turned on, the non-interacting spectrum gets modified in

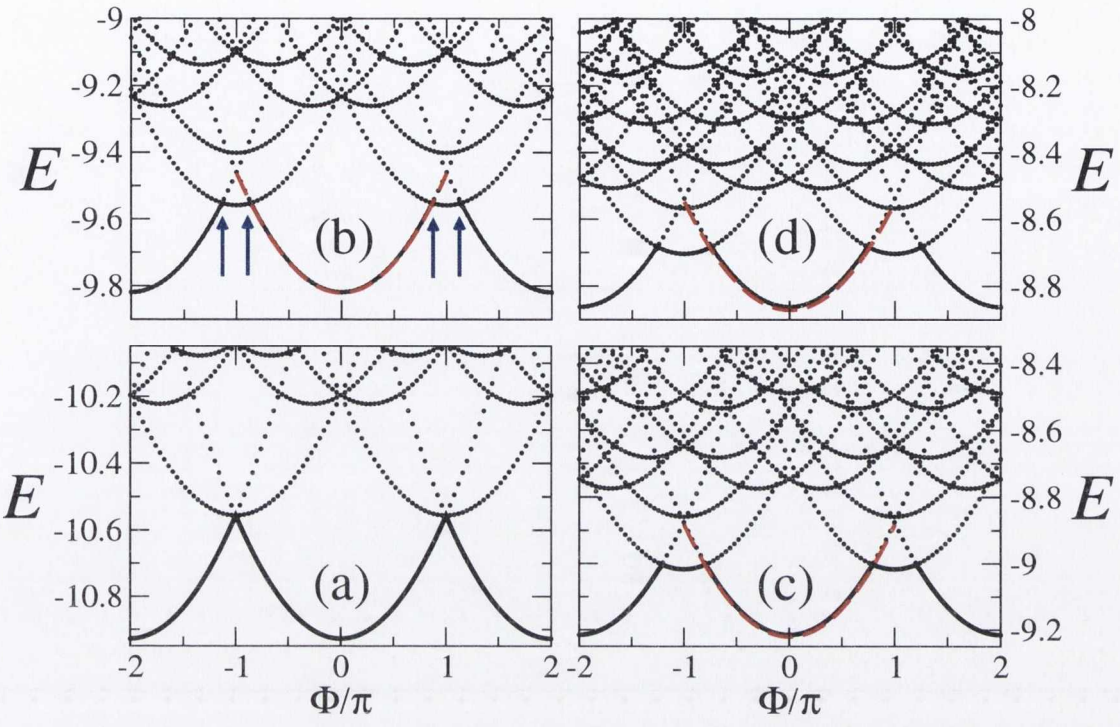

Figure 5.3: The low lying energy spectrum, E, of a 12-site ring at quarter filling ($n = 1/2$) as a function of the magnetic flux, Φ, and calculated for different interaction strengths U/t. The red dashed line is the ground state energy. ED results are in black while the dashed red lines are for CLDFT. (a) $U/t = 0$, (b) $U/t = 2$, (c) $U/t = 4$ and (d) $U/t = 6$. In panel (b) the blue arrows indicate the region where the triplet state becomes the ground state.

two ways. Firstly there is a second branch in the ground state energy as a function of Φ appearing at around $\Phi = \pm\pi$ (see the blue arrows in panel (b) of Fig. 5.3). This originates from the degeneracy lifting between the singlet and the triplet solution at $\Phi = \pm\pi$, with the triplet being pushed down in energy and becoming the ground state. The Φ region where the ground state is a triplet widens as the interaction strength increases. The second effect is the expected increase in the ground state total energy as U/t increases.

Since CLDFT is a ground state theory, it provides access only to the ground state energy, E_0. This is calculated next and plotted in Figure 5.3 in the interval $-\pi \leq \Phi \leq \pi$ for different U/t. As one can clearly see from the Figure the performance of CLDFT is rather remarkable, to a point that the CLDFT energy is practically

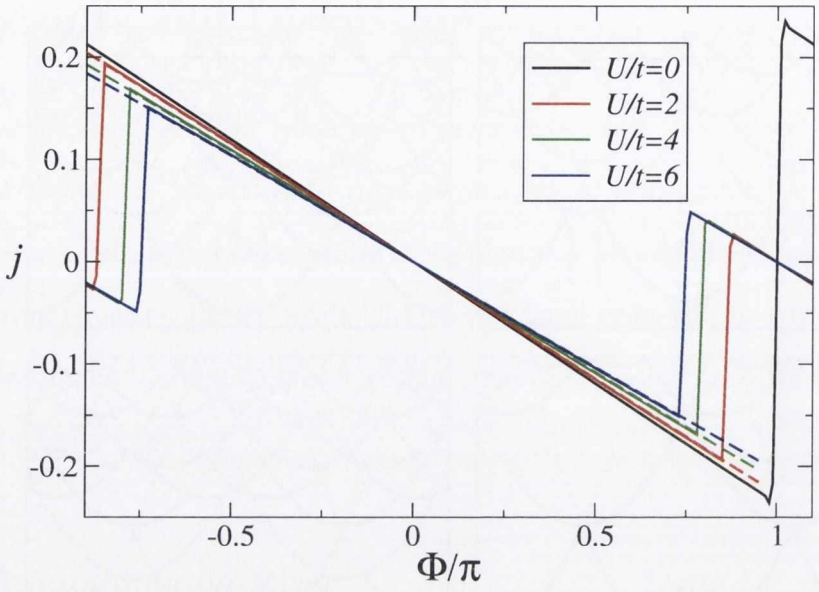

Figure 5.4: Persistent current profile, j, for a 12-site ring at quarter filling obtained with both ED and CLDFT for different U/t. The full lines are the j calculated with ED while the dashed ones are for CLDFT.

identical to that calculated with ED. However CLDFT completely misses the cusps in the $E_0(\Phi)$ profile arising from the crossover between the singlet and the triplet state. Level crossing invalidates the BA approximation leading to the breakdown of the interacting XC energy [see equation (C.5) in appendix C] and so failures are expected [146]. This observation is in agreement with earlier studies [132] in which the inability of CDFT to reproduce level crossing was already noted. Nevertheless, as long as the singlet remains the ground state, the agreement between CLDFT and ED results is remarkable, even if this small ring is rather far from being a good approximation of the thermodynamic limit (the BA solutions) upon which the functional has been constructed.

Having calculated the total energies with both ED and CLDFT, the corresponding persistent currents, j, can be obtained by taking the numerical derivative of $E_0(\Phi)$ with respect to Φ. In Figure 5.4 we show results for the quarter-filled 12-site ring whose total energy was presented in Figure 5.3. In particular we plot j only over

a period $-\pi < \Phi < \pi$, since all quantities are 2π periodic. The Figure confirms the linearity of the persistent currents with the magnetic flux for all the interaction strengths considered. The same is also true for other fillings (not presented here for the 12-site ring) away from half-filling. We also observe that the magnitude of persistent currents reduces with increasing U/t for both ED and CLDFT and that the precise dependence of j on U/t is different for different fillings. This is in good agreement with previous calculations based on the BA technique [147].

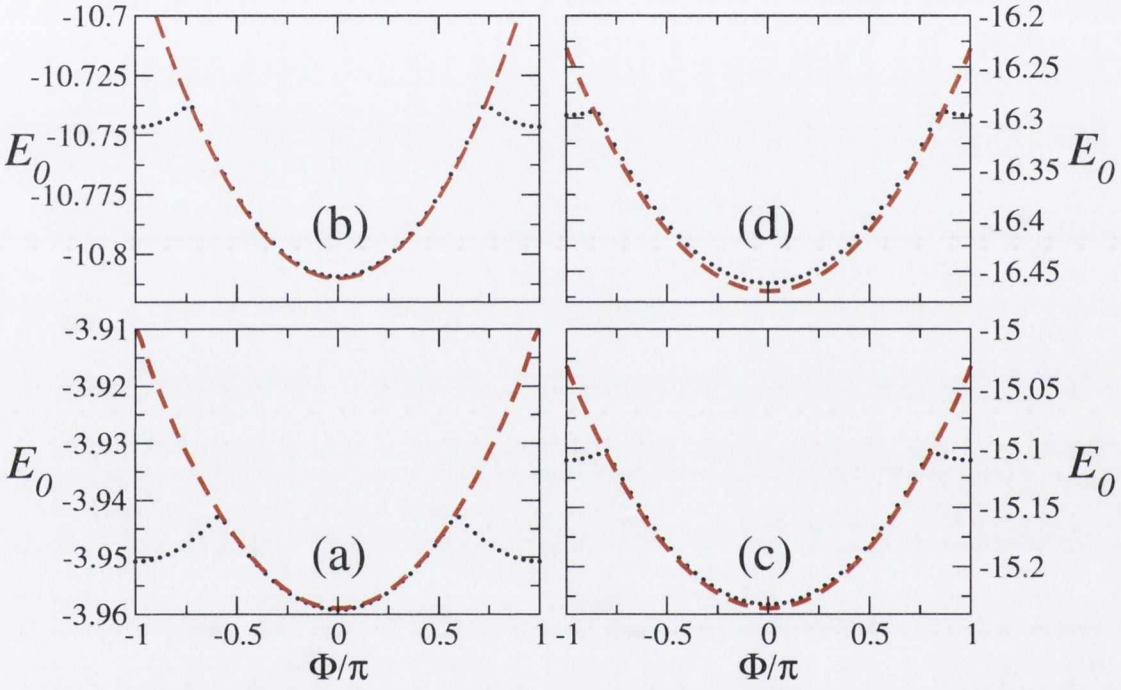

Figure 5.5: Ground state energy, $E_0(\Phi)$,as a function of the magnetic flux, Φ, calculated with both the BA technique (black line) and CDFT (dashed red line). Calculations are carried out for $L = 20$, $U/t = 4$ and different numbers of electrons: (a) $N = 2$, (b) $N = 6$, (c) $N = 10$ and (d) $N = 14$.

ED is computationally demanding and cannot be performed beyond a certain system size. For this reason, in order to benchmark CLDFT for larger rings, we have calculated the ground state energy with the BA method. An example of these calculations is presented in Figure 5.5, where once again we show $E_0(\Phi)$ for $L = 20$, $U/t = 4$ and different numbers of electrons. Also in this case the agreement between

the BA results and those obtained with CLDFT is remarkably good as long as the ground state is a singlet. Interestingly we note that the agreement is better for low filling but it deteriorates as one approaches the half-filling case ($N = 20$ in this case). This is somehow expected given the derivative discontinuity of the CLDFT XC potentials at half-filling, leading to the Mott transition.

The final quantity we wish to consider is the Drude weight, D_c, defined using (5.7). This is essentially the slope of the persistent current as a function of Φ calculated at $\Phi = 0$ and defines the magnitude of the real part of the optical conductivity in the long wave-length limit. D_c determines both qualitatively and quantitatively the transport properties of the ring. Importantly in the limit of large rings it exponentially vanishes for insulators, while it saturates to a finite value for metals. Many studies have been devolved to calculating D_c in interacting systems. Römer and Punnoose have studied D_c for finite Hubbard rings using an iterative BA technique [146]. Eckern *et. al.*, for spinless fermions, related D_c to the so-called phase sensitivity, ΔE, which is the difference in the total energy calculated at $\Phi = 0$ (periodic ground state) and that at $\Phi = \pi$ (antiperiodic ground state) [44, 161]. Recently, a DMRG algorithm has been developed to deal with complex Hamiltonian matrices and used to calculate D_c for spinless fermions [135].

Since the agreement between CLDFT and ED is proved for small rings (the slopes of the persistent currents as a function of Φ calculated with CLDFT and ED are essentially identical in figure 5.4) we concentrate here on a larger system, namely a homogeneous 60 site ring at quarter filling. Our results for the Drude weight as a function of U/t are presented in figure 5.6. Again the CLDFT data are compared with those calculated with the BA in the thermodynamic limit ($L \to \infty$) and the agreement is rather satisfactory. We note that, as for the ground state energy, also for the Drude weight the CLDFT seems to perform less well as U/t increases, i.e. as the interaction strength becomes large.

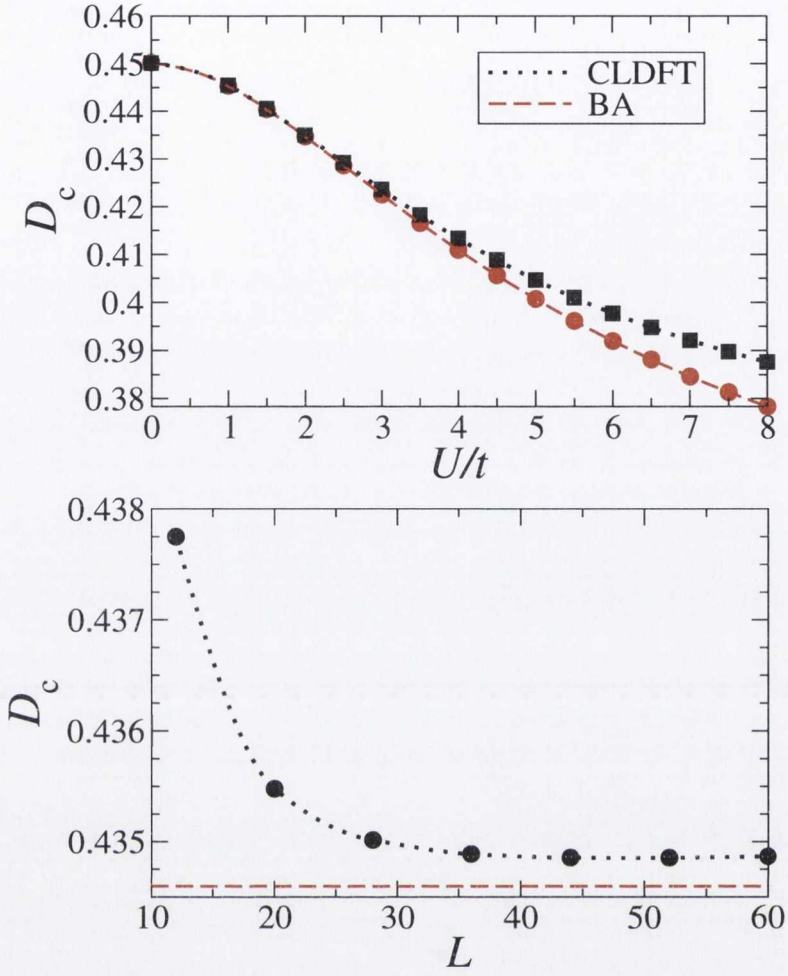

Figure 5.6: Drude coefficient D_c as a function of the interaction strength U/t (top panel) and of the number of sites in the ring, L (bottom panel). All the calculations are for quarter filling and the results in the top panel are for a 60-site ring. In the figure we compare CLDFT results (dotted black lines) with those obtained by the BA technique in the thermodynamic limit (dashed red lines). Calculations in the lower panel are for $U/t = 2$..

Then in the lower panel of figure 5.6 we illustrate the scaling properties of D_c as a function of the number of sites in the ring, L (we consider quarter filling and $U/t = 2$). Clearly D_c does not vanish at any lengths demonstrating that the system remains metallic. Furthermore it approaches a constant value already for $L > 40$. In the picture we also report the asymptotic value predicted by the BA in the thermodynamic limit $L \to \infty$ for this set of parameters. We find that the calculated

CLDFT value is only 0.06% larger than the BA one, i.e. it is in quite remarkable good agreement.

5.4.2 Scaling properties

Next we take a more careful look at the scaling properties of the persistent currents and the Drude weights as a function of both the ring size and the interaction strength. It is well known that j is strongly size dependent, since it originates from electron coherence across the entire ring [135]. For a perfect metal one expect j to scale as $1/L$ [133]. In Figure 5.7 the value of the persistent currents as a function of the ring size are presented for different electron fillings and for the two representative interaction strengths of $U/t = 2$ (a) and $U/t = 4$ (b). Calculations are performed with both the exact BA and CLDFT. As a matter of convention we calculate the persistent currents at $\Phi = \pi/2$.

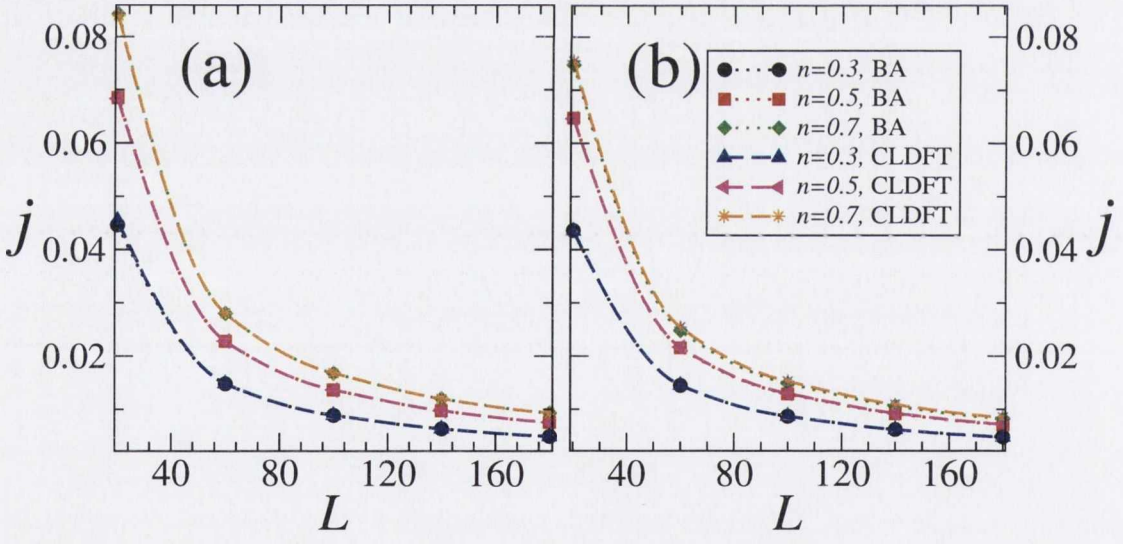

Figure 5.7: Persistent current, j, as a function of the number of site in the ring, L, and for different electron occupations, n: (a) $U/t = 2$, (b) $U/t = 4$. Results are obtained with both the exact BA technique and CLDFT. In the figure the persistent currents are calculated at $\Phi = \pi/2$, i.e. $j = j(\pi/2)$.

In general we find a monotonic reduction of the persistent current with L and an

overall excellent agreement between the BA and the CLDFT results over the entire range of lengths, occupations and interaction strengths investigated. A non-linear fit of all the curves of figure 5.7 returns us an almost perfect $1/L$ dependence of j with no appreciable deviations at any n or U/t. This indicates a full metallic response of the rings in the region of parameters investigated, thus confirming previous results obtained with the BA approach [147].

Then we look at the dependance of j and D_c on the interaction strength. In this case we consider a 60 site ring and three different different electron fillings. In general for small fluxes one expects $j = 2D_c\Phi$ and our numerical results of Fig. 5.4 demonstrates that this is approximately correct also for our definition of persistent currents $[j = j(\Phi = \pi/2)]$ over the entire U/t range investigated. We find that both

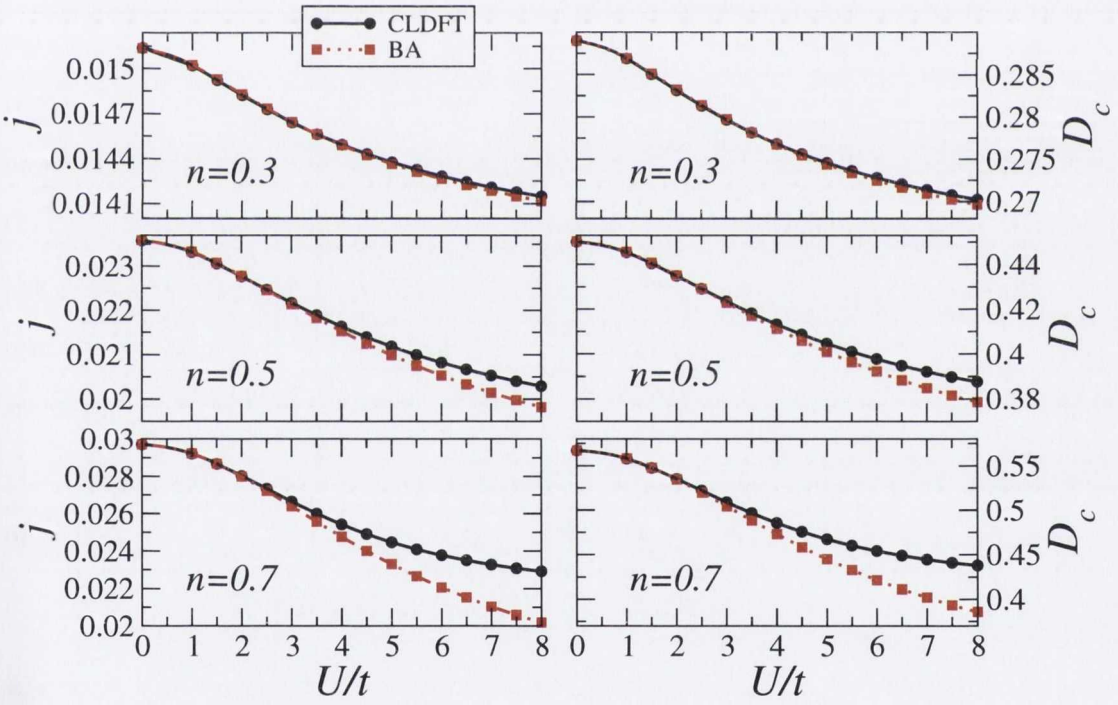

Figure 5.8: Persistent current, j, and Drude weight, D_c as a function of interaction strength U/t for a 60 site ring at different fillings. Results are obtained with both the exact BA technique and CLDFT.

j and D_c monotonically decrease as a function of the interaction strength, essentially meaning that the predicted long-wavelength optical conductivity is reduced as the

electron repulsion gets larger.

Also in this case the agreement between the BA and the CLDFT results is substantially good, although significant deviations appear in the limit of large U/t and electron filling approaching half-filling. This again corresponds to a region of the parameter space where the XC potential approaches the derivative discontinuity.

It was numerically demonstrated in the past [147] that the persistent current (and so the Drude weight) at half-filling follows the scaling relation $j \sim \mathrm{e}^{-U^2/\xi}$, with $\xi \sim 1$. However, to the best of our knowledge, no scaling relation was ever provided in the metallic case. We have then carried out a fitting analysis (the fit is limited to values of j and D_c for $U/t > 2$) and found that our data can be well represented by the scaling laws

$$j = j_0(U/t)^{-\beta}, \qquad D_\mathrm{c} = D_0(U/t)^{-\gamma}\,. \tag{5.65}$$

In general and as expected we find $\beta = \gamma$ and a quite significant dependence of the exponents on the filling. In particular table 5.1 summarizes our results and demonstrates that the decay rate of both the persistent currents and the Drude weights increases as the filling approaches half-filling. Furthermore the table also quantifies the differences between the BA and the CLDFT solutions, whose exponents increasingly differ from each other as the electron filling gets closer to $n = 1$ (for $n = 0.7$ we find $\beta^{\mathrm{BA}} \sim 2\beta^{\mathrm{CLDFT}}$).

n	β^{CLDFT}	β^{BA}
0.3	0.036	0.036
0.5	0.085	0.104
0.7	0.151	0.246

Table 5.1: Exponents for the empirical scaling laws of equation (5.65) as fitted from the data of figure 5.8.

Finally, by combining all the results of this section we can propose a scaling law for both the persistent currents and the Drude weights, valid in the metallic limit of

the Hubbard model, i.e. away from half-filling. This reads

$$j = \frac{j_0(n)}{L}\left(\frac{U}{t}\right)^{-\beta(n)} , \tag{5.66}$$

where both the constant j_0 and the exponent β are function of the electron filling n. Note that an identical equation holds for D_c.

5.4.3 Scattering to a single impurity

Having established the success of the BALDA to CLDFT for the homogeneous case we now move to a more stringent test for the theory, namely the case of a ring penetrated by a magnetic flux in the presence of a single impurity. This is a problem, which has received already considerable attention in the past [139, 160, 144]. Note that, as in *ab initio* DFT, this is a situation different from the reference system used to construct the BALDA (since it deals with a non homogeneous system) and therefore one might expect a more pronounced disagreement with exact results. As the BA equations are integrable only for the homogeneous case we now benchmark our CLDFT results with those obtained by ED. This however limits our analysis to small rings.

The single impurity in the ring is described by simply adding to the Hamiltonian of equation (5.42) the term

$$\hat{H}_{\text{imp}} = \varepsilon_{\text{imp}}\hat{n}_i , \tag{5.67}$$

where ε_{imp} is the modification to the on-site energy at the impurity site i. The inclusion of an impurity produces in general electron backscattering so that we expect the persistent currents to get reduced. In figure 5.9 we present the general transport features for this inhomogeneous system. Calculations have been obtained with CLDFT for a ring comprising 53 sites and $N = 26$ and $U/t = 4$. Again the persistent currents are calculated at $\Phi = \pi/2$.

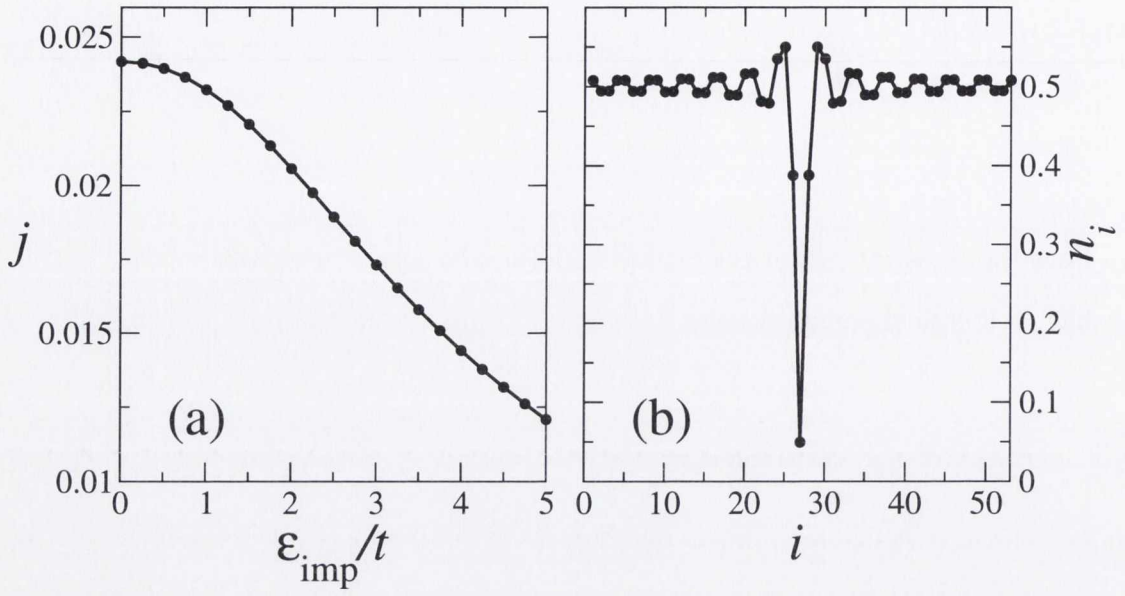

Figure 5.9: (a) Persistent current, j, as a function of single impurity strength, ε_{imp}, obtained from the CLDFT for $L = 53$, $N = 26$, $U/t = 4$ and $\Phi = \frac{\pi}{2}$. In (b) we show a typical site density profile for a positive single impurity site potential.

Panel (a) shows j as a function of the impurity on-site energy. As expected from standard scattering theory the current is reduced as the the impurity potential increases, thus creating a potential barrier. The electron density profile for this situation is presented in panel (b), where one can clearly observe an electron depletion at the impurity site and Friedel's oscillations around it.

A quantitative assessment of our CLDFT results is provided in Fig. 5.10 where they are compared with those obtained by exact diagonalization for a 13 site ring close to quarter filling ($N = 6$). In particular we present j as a function of the impurity potential, ε_{imp}, for both $U/t = 2$ and $U/t = 4$. In general we find a rather satisfactory agreement between CLDFT and the exact results in particular for small ε_{imp} and U/t. As the electron scattering becomes more significant deviations appear and the quantitative agreement is less good. Importantly we notice that the ED results systematically provide a persistent current lower than that calculated with CLDFT, at least for the values of electron filling investigated here. This seems to be

a consistent trend also present for the homogeneous case (see figure 5.8), although the deviations in that case are less pronounced (for the same electron filling and interaction strength). Therefore we tentatively conclude that most of the errors in the impurity problem have to be attributed to the errors already present in the homogeneous case. We then expect that CLDFT provides a good platform for investigating scattering problems at only minor computational costs. As such CLDFT appears as the ideal tool for investigating the interplay between electron-electron interaction and disorder in low dimensional structures.

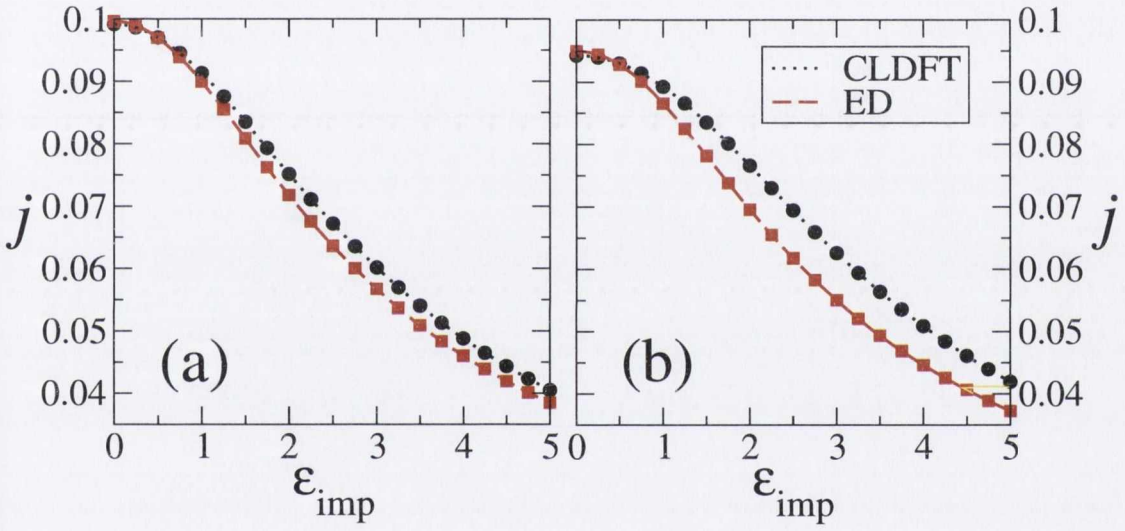

Figure 5.10: Comparison between the persistent currents calculated with CLDFT (black symbols and dotted line) and by ED (red symbols and dashed line) for a 13 site ring and $N = 6$. The j's are obtained at $\Phi = \pi/2$ for two different values of the interaction strength, namely $U/t = 2$ (a) and $U/t = 4$ (b).

We remark here that our XC functionals (both the static and dynamic ones) in the presence single impurity could, in principle, be used to investigate locality or otherwise of the CLDFT as previously done for LDFT. Such investigation is currently under study.

5.5 Summary

In this chapter, we have presented an extension of the BALDA for the one-dimensional Hubbard problem on a ring to CLDFT. Then we have investigated the response of interacting rings to an external flux both in the homogeneous and inhomogeneous case, and we have compared our results with those obtained by exact techniques. Our analysis has been confined to the metallic limit, i.e. away from half-filling, where the Hubbard model has a metal to insulator transition. In general we have found that CLDFT performs rather well in calculating both the persistent currents and the Drude weights in the homogeneous case. Furthermore a similar level of accuracy is transferred to the impurity problem. With these results in hands we propose to use CLDFT in the study of AB rings where the combined effect of electron-electron interaction and disorder can be addressed for large rings, so that a numerical evaluation of the various scaling laws proposed in the past can be accurately carried out.

Part II

Chapter 6

The *Siesta* code and beyond LDA functionals

6.1 *Siesta* code

In Chapter 2, we described the basics of DFT and the various approximate XC potentials that are most commonly used. There are many packages available containing a practical implementation of KS DFT. The choice of a package depends on many parameters such as cost, functionality, efficiency, ease of usage and robustness.

Calculations in this part of the thesis are based on the DFT code *Siesta* (Spanish Initiative for the Estimation of Systems with Thousands of Atoms) [162, 163]. *Siesta* is an advanced DFT code using pseudopotentials and efficient numerical atomic orbital basis sets. In this section a brief overview of the package is given while for detailed descriptions one can refer to references [162, 163, 164, 165]. Together with being a very efficient code, it is readily available and its source is distributed in such a way that it allows academic license users to make modifications depending on their interests.

6.1.1 Pseudopotential

Solid state properties are mainly determined by the outermost (valence) electrons of a given atom, while the core electrons are 'frozen' in their atomic state. This is because the core electrons do not participate in the chemical bonding, being placed in the fully occupied inner shells. Only the electronic properties of the valence electrons are influenced strongly by the chemical environment. This simple consideration underpins the so called pseudopotential method. The idea is to replace the individual nuclear and core electron potentials by an effective potential which takes into account their net effects on the valence electrons. This effective potential (often referred to as pseudopotential [166]) provides a convenient way of reducing both the electronic states and basis required for any calculation.

A pseudopotential is required for each atomic species in any simulation. To generate a pseudopotential, two steps are required: Firstly, the true wavefunctions calculated for the atom by an all-electron DFT approach are modified in the core region to remove rapid oscillations of the wavefunctions near the nucleus, due to the very strong potential in that region and the orthogonality condition between different states. Next, the pseudopotential that will reproduce the pseudo wavefunctions is then calculated by inverting the Schrödinger equation. The pseudo wavefunctions corresponding to this modified potential possess smoother behaviour than the true wavefunctions (see Figure 6.1), which in turns dramatically reduces the number of basis functions required to describe the wavefunction.

Usually, the following conditions must be satisfied when pseudopotentials are generated:

- The corresponding pseudo wavefunctions and the all-electron agree beyond a chosen core radius r_c (see Figure 6.1).

- Pseudo and all-electron eigenvalues agree for a chosen atomic reference con-

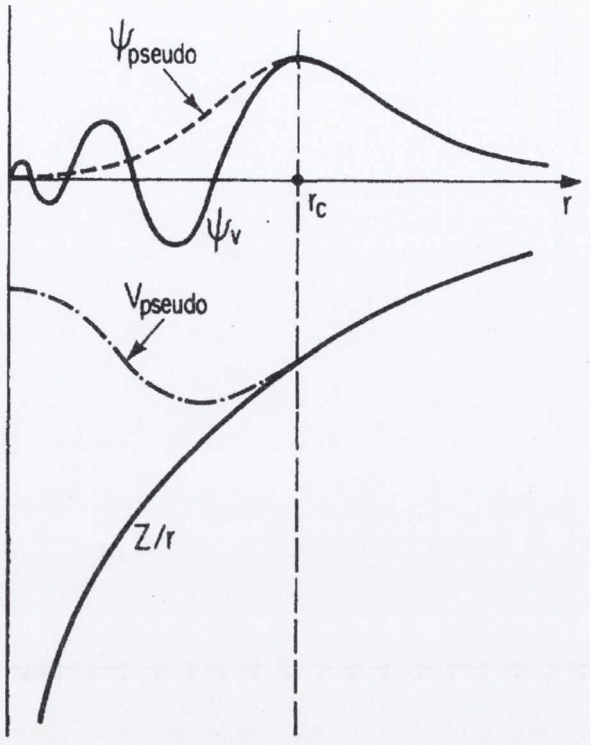

Figure 6.1: A sketch illustrating all-electron potential (solid line) and pseudopotential (dashed line), and their corresponding wavefunctions. The radius, r_c, represents the radius above which the all-electron and pseudopotential values are equal. Picture is taken from [167].

figurations. In other words, the pseudopotential must describe the valence properties in a different environment including atoms, ions, molecules and condensed matter.

- The logarithmic derivatives of the pseudo and the all-electron wavefunctions agree at r_c.

- The integrated charge inside r_c for each wavefunction agrees i.e. the pseudo and the all-electron wavefunctions have the same norm (*norm-conserving pseudopotential*).

Siesta uses nonlocal [168], norm-conserving [169] fully separable Troullier-Martins pseudopotentials. This means that the pseudopotentials are built from a smooth local

part, identical for all the angular momentum channels, plus a non-local part.

6.1.2 Basis set

Practical DFT calculations expand the density matrix and all the operators over a basis set. There are two classes of basis set most commonly used in electronic calculations. The first class consists of basis functions that resemble the exact eigenstates of the system (e.g. pseudoatomic orbitals or gaussians) whereas the second are system-independent (e.g. plane waves or wavelets). *Siesta* package utilizes a basis of localized pseudoatomic orbitals (PAOs) [170]. For each atom I positioned at $\vec{R}_I$ a set of PAOs are defined as the product of a numerical radial function and a spherical harmonic [170]

$$\phi_{I,lmn}(\vec{r}) = \varphi_{Iln}(r_I)Y_{lm}(\widehat{\vec{r}_I}). \tag{6.1}$$

Here, $\vec{r}_I = \vec{r}_I - \vec{R}_I$ and the angular momentum is labeled l, m. The numerical radial functions defined in the equation (6.1) are made strictly zero beyond a certain cut-off radius r_c [171]. This confinement of PAOs is very important for making the Hamiltonian and overlap matrices in sparse form and crucial for efficiency of the package. Unlike the plane-wave basis, the PAOs basis enables faster and larger calculations, mainly due to the strict cutoff at r_c in the basis functions, which increases locality, and enables even linear scaling for large systems. On the other hand, the method provides no systematic way to obtain convergence (such as the plane-wave cutoff energy), so that many parameters must be optimized to achieve reliable results and required level of accuracy. Example of such parameters in *Siesta* include pseudopotentials, k-mesh and mesh-cutoff. The convergence test then proceeds by choosing relevant quantity of the problem (e.g. total energy) and then start the calculation with a reasonable minimum value for each of the parameters to obtain the chosen quantity. By gradually increasing the parameter in question, one finds that the relevant property for the study will converge.

Generally, there will be several orbitals (labelled by the index n) possesing the same angular dependence, but different radial dependence. These are the so-called multiple-ζ basis functions. They are constructed by using the split-valence method [172]. For example, the second-ζ is a function whose radial part has the same tail as that of the corresponding first-ζ beyond a split-radius r_l^s and a polynomial of the form

$$\varphi_l^{2\zeta} = \begin{cases} r^l(a_l - b_l r^2) & \text{if } r < r_l^s \\ \varphi_l^{1\zeta} & \text{if } r \geq r_l^s \end{cases} . \tag{6.2}$$

where a_l and b_l are determined by imposing the continuity of the wavefunction and of its first derivative at r_l^s. The quality of the basis set can be further enhanced by including the so-called polarization functions. These are obtained by introducing a small external electric field to the PAOs. Such perturbation accounts for the deformation induced by bond formation and produces basis functions corresponding to angular momenta not present among the valence states. Such a procedure enlarges the variational freedom in the minimization scheme.

6.1.3 Self-consistent iteration

Within the nonlocal pseudopotential approximation, the standard KS single-particle Hamiltonian in *Siesta* is written as

$$\hat{\mathcal{H}} = \hat{\mathcal{T}} + \sum_I \hat{v}_I^{nloc} + \sum_I \hat{v}_I^{loc} + \hat{v}_H + \hat{v}_{xc}, \tag{6.3}$$

where $\hat{\mathcal{T}}$, $\hat{v}_H$, and $\hat{v}_{xc}$ are the kinetic energy, the Hartree potential and the XC potential operators respectively. The local and nonlocal parts of the pseudopotential operator of atom I are represented by $\hat{v}_I^{loc}$ and $\hat{v}_I^{nloc}$ respectively. The eigenstate, Ψ, of the Hamiltonian is expanded over PAO basis set, ϕ_μ, so that KS equations can

then be written as

$$\begin{aligned} \hat{\mathcal{H}}\Psi &= E\Psi \quad \text{with} \\ \Psi_i &= \sum_{\mu} c_{\mu}^{i}\phi_{\mu}, \end{aligned} \tag{6.4}$$

where μ denotes set of indices $\{Inlm\}$. By defining the overlap matrix

$$S_{\nu\mu} = \int d\vec{r}\phi_{\nu}^{*}(\vec{r})\phi_{\mu}(\vec{r}), \tag{6.5}$$

the Hamiltonian matrix is obtained by computing the following integrals

$$\mathcal{H}_{\nu\mu} = \int d\vec{r}\phi_{\nu}^{*}(\vec{r})\hat{\mathcal{H}}\phi_{\mu}(\vec{r}). \tag{6.6}$$

The size of these matrices is a function of the basis set used in the simulation. The electron charge density is given by

$$n(\vec{r}) = \sum_{i} f_i|\Psi_i|^2, \tag{6.7}$$

where $f_i \in [0, 1]$ is the occupation number of the state Ψ_i and energy E_i. By using the PAO basis set, the real space representation of the electron charge density becomes

$$n(\vec{r}) = \sum_{\nu\mu} n_{\nu\mu}\phi_{\nu}^{*}\phi_{\mu}, \tag{6.8}$$

where $n_{\nu\mu}$ is the density matrix expressed as

$$n_{\nu\mu} = \sum_{i} c_{\nu}^{i*}c_{\mu}^{i}g(E_i), \tag{6.9}$$

with $g(E_i)$ being the Fermi-Dirac distribution. The total number of electrons, N_e, in the valence band can be expressed in terms of the density and overlap matrices

$$N_e = \sum_{\nu\mu} n_{\nu\mu} S_{\nu\mu} = \mathrm{Tr}[nS]. \tag{6.10}$$

In order to eliminate the long range interaction of v_I^{loc} in the equation (6.3), it is screened with a neutral atom (NA) potential v_I^{NA} created by a NA charge density n_I^{NA}. The NA potential is short range since the core attraction and the electron Coulomb repulsion of the NA charge cancel each other beyond r_c and is defined as [165]

$$v_I^{NA} = v_I^{loc} + \int d\vec{r}' \frac{n^{NA}(\vec{r}')}{|\vec{r} - \vec{r}'|}, \tag{6.11}$$

so that the equation (6.3) becomes

$$\hat{\mathcal{H}} = \hat{T} + \sum_I \hat{v}_I^{nloc} + \sum_I \hat{v}_I^{NA} + \delta\hat{v}_H + \hat{v}_{xc}, \tag{6.12}$$

where

$$\delta\hat{v}_H(\vec{r}) = \int d\vec{r}' \frac{\delta n(\vec{r}')}{|\vec{r} - \vec{r}'|} \quad \text{with} \quad \delta n(\vec{r}') = n(\vec{r}') - n^{NA}(\vec{r}'). \tag{6.13}$$

The matrix elements of the first three terms in the equation (6.12) and the overlap matrix are calculated in reciprocal space and tabulated as a function of interatomic distances since the operators are independent of $n(\vec{r})$ [162]. On the other hand, the operators $\delta\hat{v}_H$ and $\hat{v}_{xc}$ depend on $n(\vec{r})$ and thus their matrix elements are calculated on a real space grid whose fineness is determined by single energy cutoff (mesh-cutoff) equivalent to the highest energy of the planewaves can be represented on the same grid.

Since the Hamiltonian depends on the electron charge density and vice-versa, a self-consistent solution is sought for. An initial density matrix, n^{init}, is used to construct an initial Hamiltonian, $\mathcal{H}[n^{init}]$. From this Hamiltonian a new density matrix,

$n^{out} = n(\mathcal{H}[n^{init}])$ is calculated corresponding to the solution of the KS equation from $\mathcal{H}[n^{init}]$. This new density matrix (usually part of the new density matrix is mixed with the initial density matrix in order to achieve fast convergence) is then used as the initial density matrix i.e. $n^{out} = n^{init}$ to construct a new Hamiltonian. This procedure is repeated until a convergence criteria is fulfilled. In other words, the matrix norm of n^{init} and n^{out} must be less than a predetermined tolerance:

$$||n^{init} - n^{out}|| < \delta. \tag{6.14}$$

Accelerated and better convergence is reached with more sophisticated algorithms mixing input and output density matrices. *Siesta* uses one those algorithms called Pulay mixing [173], which mixes the density matrices collected from several preceding iterations.

6.1.4 Brillouin-Zone sampling and the total energy

For periodic systems, the real space integration over the (infinitely extended) system is replaced by integrating over the (finite) first Brillouin-Zone (BZ) in reciprocal space via the Bloch's theorem. Since *Siesta* assumes periodic boundary conditions, the real Hamiltonian matrix elements can be written, following Bloch's theorem, at a given $\vec{k}$-point $\vec{k}$ $(\equiv k_x, k_y, k_z)$ in the form

$$\mathcal{H}_{\mu\nu}(\vec{k}) = \sum_{\nu' \equiv \nu} \mathcal{H}_{\mu\nu'} e^{i\vec{k}\cdot(\vec{R}_{\nu'} - \vec{R}_{\mu})}, \tag{6.15}$$

where $(\nu' \equiv \nu)$ means that $\phi_{\nu'}$ and ϕ_{ν} are equivalent orbitals under lattice translation noting that ϕ_{μ} and ϕ_{ν} are centred on a unit cell. This yields a complex $N \times N$ eigenvalue problem, where N is the number of orbitals in the unit cell, which is then solved at every sampled $\vec{k}$-point in the BZ.

For any given $\vec{k}$-vector in the BZ, the wavefunction can be expanded over the

localized orbitals as follows:

$$\Psi_i(\vec{k},\vec{r}) = \sum_{\mu'} e^{i\vec{k}\cdot\vec{R}_{\mu'}} \phi_{\mu'}(\vec{r}) c^i_{\mu'}(\vec{k}), \tag{6.16}$$

where the band index is labelled by i, $c^i_{\mu'} = c^i_{\mu}$ if $(\mu' \equiv \mu)$, and $\Psi_i(\vec{k},\vec{r})$ is normalized in the unit cell. The electron charge density is

$$n(\vec{r}) = \sum_i \int_{BZ} d\vec{k} f_i(\vec{k}) |\Psi_i(\vec{k},\vec{r})|^2 = \sum_{\mu',\nu'} n_{\mu',\nu'} \phi^*_{\nu'}(\vec{r}) \phi_{\mu'}(\vec{r}), \tag{6.17}$$

and

$$n_{\mu,\nu} = \sum_i \int_{BZ} d\vec{k} c^i_{\mu}(\vec{k}) f_i(\vec{k}) c^i_{\nu}(\vec{k}) e^{i\vec{k}\cdot(\vec{R}_{\nu}-\vec{R}_{\mu})} \tag{6.18}$$

is the density matrix which is real and such that $n_{\mu,\nu} = n_{\mu',\nu'}$ if $(\mu,\nu) \equiv (\mu',\nu')$. The $\vec{k}$-points for the integration of the equation (6.18) are typically chosen according to the scheme of Monkhorst and Pack [174].

The KS total energy can then be written as

$$E_{KS} = \sum_{\mu\nu} \mathcal{H}_{\mu\nu} n_{\mu\nu} - \frac{1}{2} \int d\vec{r} v_H(\vec{r}) n(\vec{r}) + \int d\vec{r} (\varepsilon_{xc}(\vec{r}) - v_{xc}(\vec{r})) n(\vec{r}) + \sum_{I<J} \frac{Z_I Z_J}{R_{IJ}}, \tag{6.19}$$

where I, J are atomic indices, $R_{IJ} \equiv |R_I - R_J|$, Z_I, Z_J are the valence ion pseudoatom charges and $\varepsilon_{xc}(\vec{r})$ is the XC energy density.

6.2 Beyond LDA functionals in the *Siesta* code

As remarked in Chapter 2, the inadequacies of the DFT stems from the approximate nature of commonly used functionals. This include the self-interaction error (SIE), i.e. the fact that an electron experiences the Hartree and XC potentials generated by its own charge density. The reason for this error is attributed to only a partial cancellation of the SI contained in the classical Coulomb energy with that in the XC

term [74, 175]. The presence of SIE is reflected in the wrong asymptotic behaviour of approximate functionals for finite systems. For example, the KS potential, instead of having a $-1/r$ decay as $r \to \infty$ for neutral systems (like an atom), decays exponentially with the distance in both the LDA and GGA. One major effect of this behaviour is that the eigenvalue of the highest occupied KS orbitals does not correspond to the negative of the ionization potential as it should. Quite a number of works have been carried out in order to construct SI free functionals [176], however there is no known exchange functional that is completely SI free apart from the direct self-interaction correction (SIC) formalism of Perdew and Zunger [74]. This is an approach which uses a KS orbital-dependent XC potential, whose practical implementations are computationally demanding. Therefore its applications are restricted to small systems. In view of this, various attempts have been made to develop more computationally undemanding SIC schemes. The atomic SIC (ASIC) is a recent development in this direction and has been implemented in *Siesta* package.

Another computationally inexpensive feature added to *Siesta* is the LDA+U scheme [177]. It consists in correcting the LDA XC energy to give a better description of electronic correlations. Here, the LDA XC energy is replaced with the Hubbard-U energy which depends on the orbital occupations. Typically the correction is done for the more localized orbitals like the d and f orbitals.

In this section, we give a brief description of the ASIC starting from a general overview of the SIC and the LDA+U algorithms. References [75, 76] give a complete description of ASIC and LDA+U scheme and their implementation in *Siesta*.

6.2.1 Self-interaction correction

The seminal work of Perdew and Zunger [74] pioneered the modern theory of SIC. Let us rewrite the spin-polarized form of the KS total energy as

$$E_{KS}[n^{\uparrow}, n^{\downarrow}] = \mathcal{T}_s[n] + E_H[n] + \int d\vec{r} n(\vec{r}) v(\vec{r}) + E_{xc}[n^{\uparrow}, n^{\downarrow}], \tag{6.20}$$

where $n = n^{\uparrow} + n^{\downarrow}$. The first term is the kinetic energy of the non-interacting system, the second is the Coulomb interaction and the third is the interaction between electron charge density $n(\vec{r})$ and an external potential $v(\vec{r})$. These three terms are all known exactly, however the last term is unknown and therefore is usually approximated by some functional form.

The main idea of the Perdew and Zunger SIC is that of subtracting directly the spurious SI for each Kohn-Sham (KS) orbital ψ_i. The SIC-LDA [178] XC energy thus writes

$$E_{xc}^{\mathrm{SIC}}[n^{\uparrow}, n^{\downarrow}] = E_{xc}^{\mathrm{LDA}}[n^{\uparrow}, n^{\downarrow}] - \sum_{i\sigma}^{\text{occupied}} \delta_i^{\mathrm{SIC}}, \tag{6.21}$$

where $E_{xc}^{\mathrm{LDA}}[n^{\uparrow}, n^{\downarrow}]$ is the LDA-XC energy and δ_i^{SIC} is the sum of the self-Hartree and self-XC energy associated to the charge density $n_i^{\sigma} = |\psi_i^{\sigma}|^2$ of the fully occupied KS orbital ψ_i^{σ}

$$\delta_i^{\mathrm{SIC}} = E_H[n_i^{\sigma}] + E_{xc}^{\mathrm{LDA}}[n_i^{\sigma}, 0]\,. \tag{6.22}$$

Here E_H is the Hartree energy and $\sigma = \uparrow, \downarrow$ is the spin index.

The search for the energy minimum is not trivial, since E_{xc}^{SIC} is not invariant under a unitary rotation of the occupied KS orbitals. As a consequence the KS method becomes either non-orthogonal or size-inconsistent. These problems however can be avoided [179, 180, 181] by introducing a second set of orbitals ϕ_n^{σ} related to the

canonical KS orbitals by a unitary transformation $\mathcal{M}$

$$\psi_i^\sigma = \sum_j \mathcal{M}_{ij}^\sigma \phi_j^\sigma \,. \tag{6.23}$$

The functional can then be minimized by varying both the orbitals ψ and the unitary transformation $\mathcal{M}$. This leads to a system of equations

$$H_i^\sigma \psi_i^\sigma = (H_0^\sigma + \Delta v_i^{\mathrm{SIC}})\psi_i^\sigma = \epsilon_i^{\sigma,\mathrm{SIC}} \psi_i^\sigma \,, \tag{6.24}$$

$$\psi_i^\sigma = \sum_j \mathcal{M}_{ij} \phi_j^\sigma \,, \tag{6.25}$$

$$\Delta v_i^{\mathrm{SIC}} = \sum_j \mathcal{M}_{ij} v_j^{\mathrm{SIC}} \frac{\phi_j^\sigma}{\psi_i^\sigma} = \sum_j v_j^{\mathrm{SIC}} \hat{P}_i^\phi \,, \tag{6.26}$$

where H_0^σ is the LDA Hamiltonian, $\hat{P}_j^\phi \psi_i^\sigma(\vec{r}) = \phi_j^\sigma(\vec{r})\langle\phi_j^\sigma|\psi_i^\sigma\rangle$ and $v_i^{\mathrm{SIC}} = v_H([n_i];\vec{r}) + v_{xc}^{\sigma,\mathrm{LDA}}([n_i^\uparrow, 0];\vec{r})$, with v_H and $v_{xc}^{\sigma,\mathrm{LDA}}$ the Hartree and LDA-XC potential respectively.

In equation (6.24) we have used the fact that at the energy minimum the matrix of SIC KS-eigenvalues $\epsilon_{ij}^{\sigma,\mathrm{SIC}}$ is diagonalized by the KS orbitals ψ_i. Importantly such minimization scheme can be readily applied to extended systems, without loosing the Bloch representation of the KS orbitals [182, 183].

6.2.2 Atomic SIC scheme

The ASIC method consists in taking two drastic approximations in equation (6.24). First we assume that the orbitals ϕ_j, that minimize the SIC functional are atomic-like orbitals Φ_j^σ (ASIC orbitals) thus

$$\sum_j v_j^{\mathrm{SIC}}(\vec{r})\hat{P}_j^\phi \;\rightarrow\; \alpha \sum_j \tilde{v}_j^{\sigma\mathrm{SIC}}(\vec{r})\hat{P}_j^\Phi \,, \tag{6.27}$$

where $\tilde{v}_j^{\sigma\mathrm{SIC}}(\vec{r})$ and $\hat{P}_j^{\Phi}$ are the SIC potential and the projector associated to the atomic orbital Φ_j^{σ}. Secondly we replace the non-local projector $\hat{P}_j^{\Phi}$ with its expectation value in such a way that the final ASIC potential reads

$$v_{\mathrm{ASIC}}^{\sigma}(\vec{r}) = \alpha \sum_j \tilde{v}_j^{\sigma\mathrm{SIC}}(\vec{r}) p_j^{\sigma} \,, \tag{6.28}$$

where p_j^{σ} is the orbital occupation (essentially the spin-resolved Mülliken orbital population [184]) of Φ_j.

Note that in the final expression for the potential a factor α appears. This is an empirical scaling term that accounts for the fact that the ASIC orbital Φ in general do not coincide with those that minimize the SIC functional (6.21). By construction $\alpha = 1$ in the single particle limit, while it vanishes for the homogeneous electron gas. Although in general $0 < \alpha < 1$, extensive testing [75, 76] demonstrates that a value around 1 describes well ionic solids and molecules, while a value around 1/2 is enough for mid- to wide-gap insulators. In the following chapter we will label with $\mathrm{ASIC}_{1/2}$ and ASIC_1 calculations obtained respectively with $\alpha = 1/2$ and $\alpha = 1$.

Finally we make a few comments over the total energy. The present theory is not variational since the KS potential cannot be related to a functional by a variational principle. However, since typical LDA energies are more accurate than their corresponding KS potentials, we use the expression of equation (6.21) as suitable energy. In this case the orbital densities entering the SIC are those given by the ASIC orbital Φ. Moreover, in presenting the data in the following chapter, we will distinguish results obtained by using the SIC energy (6.21) from those obtained simply from the LDA functional evaluated at the ASIC density, i.e. without including the δ_n corrections (6.22).

6.2.3 LDA+U scheme

The LDA+U [78, 79, 80] is another extension to the LDA where a generalized Hubbard model is introduced in order to treat localized electrons. The scheme is not computationally demanding and is considered to be an efficient approach for the description of large scale correlated systems. The LDA+U total energy functional, E_{LDA+U}, is usually given by adding the energy of a generalized Hubbard model, E_U, for the localized electrons to the LDA functional, E_{LDA}, and then subtracting a double counting energy, E_{DC}, of the localized electrons described in a mean-field sense, i.e.

$$E_{LDA+U}[n^\sigma, p^\sigma] = E_{LDA}[n^\sigma] + E_U[p^\sigma] - E_{DC}[p^\sigma], \tag{6.29}$$

where E_U and E_{DC} are

$$\begin{aligned} E_U &= \frac{1}{2}U \sum_{m_1,m_2,\sigma} p^\sigma_{m_1} p^{\bar{\sigma}}_{m_2} + \frac{1}{2}(U-J) \sum_{m_1 \neq m_2,\sigma} p^\sigma_{m_1} p^\sigma_{m_2}, \\ E_{DC} &= \frac{U}{2} p(p-1) - \frac{J}{2} \sum_\sigma \tilde{p}_\sigma (\tilde{p}_\sigma - 1). \end{aligned} \tag{6.30}$$

$\tilde{p}_\sigma = \mathrm{Tr}(p^\sigma_{m_1,m_2}) = \sum_m p^\sigma_{mm}$, $p = \sum_\sigma \tilde{p}_\sigma$, $p^\sigma_m = p^\sigma_{mm}$ and $p^\sigma_{m_1,m_2}$ are the elements of an occupation number matrix, $\mathbf{p}_\sigma$, which is calculated self-consistently within the scheme. The screened Coulomb and exchange parameters U and J respectively are assumed to be independent of the magnetic quantum number m but depend on the quantum number l. These approximations correspond to neglecting the possible non-spherical character of the effective interactions. Additionally, the parameters U and J are usually redefined into an effective parameter $U_{eff} = U - J$

Knowledge of the occupation numbers is important in order to determine correlation effect. The occupation matrix $\mathbf{p}_\sigma$ can be evaluated by introducing a projection operator $\hat{P}^\sigma_m$ as

$$p^\sigma_m = \sum_\alpha f^\sigma_\alpha \langle \phi^\sigma_\alpha | \hat{P}^\sigma_m | \phi^\sigma_\alpha \rangle, \tag{6.31}$$

where ϕ_α^σ are the KS eigenvectors for the α state with spin σ and f_α^σ is their occupation. The index α contains the band and momentum indices while m index includes the site, angular momentum and multiplicity of basis function indices. For non-orthogonal basis orbitals, different sets of occupation number matrices are expected to arise from different choice of the projection operators, $\hat{P}_m^\sigma$. The effective non-local potential in terms of the projectors is now

$$\hat{v}^\sigma = \sum_m U_{eff} \left(\frac{1}{2} - p_m^\sigma \right) \hat{P}_m^\sigma, \tag{6.32}$$

such that the KS potential and the orbital energy are respectively

$$\begin{aligned} \hat{v}_{LDA+U}^\sigma &= \hat{v}_{LDA}^\sigma + \sum_m U_{eff} \left(\frac{1}{2} - p_m^\sigma \right) \hat{P}_m^\sigma \\ \epsilon_{m[LDA+U]}^\sigma &= \frac{\partial E}{\partial p_m^\sigma} = \epsilon_{m[LDA]}^\sigma + U_{eff} \left(\frac{1}{2} - p_m^\sigma \right). \end{aligned} \tag{6.33}$$

The major difference between ASIC and LDA+U arises from the way unoccupied states are treated. While LDA+U has the capacity to correct the unoccupied states by shifting their orbital energies upward, ASIC only acts on the occupied orbitals which are shifted towards lower energies. This, therefore, leads to two different mechanisms in which the opening of the band gaps of electronic structure is handled. Since ASIC only acts on the occupied states, corrections are not expected for covalent systems where conduction and valence bands are bonding and antibonding states from the same atomic orbitals. However, for ionic systems ASIC will be effective due to the difference in the orbital contents of the valence and conduction bands.

Many-body perturbation theory in Hedins GW approximation [185] has become a method of choice in quantitatively describing quasiparticle excitations in solids as measured by direct and inverse photoemission spectroscopy (PES/IPES) or optical absorption. Here, the self-energy in the Hedin's approximation is calculated to lowest order in the screened interaction W. The method has, over the last decade, been

applied to d- or f- electron systems though not as successful as anticipated because it suffers from similar pathologies of the LDA being its starting point [186]. Since the method is yet to be implemented in *Siesta*, we do not wish to discuss it in detail but just to mention that LDA+U has been shown to be an approximate GW scheme for localized d/f states [78, 186].

Chapter 7

Performance of ASIC functional in computing exchange parameters of selected systems

7.1 Introduction

Theoretical studies based on density functional theory (DFT) [31, 32] have given remarkable insights into the electronic and magnetic properties of both molecules and solids [187]. In particular, a number of these studies attempt to quantitatively describe the magnetic interaction in a broad range of systems including transition metals [188], hypothetical atomic chains [189, 190], ionic solids [191, 192, 193], transition metal oxides [194, 195] and transition metal polynuclear complexes [196, 197, 198]. DFT uses an effective single-particle picture where spin symmetry is generally broken. For this reason exchange parameters J are conventionally extracted by using a mapping procedure, where total energy calculations are fitted to a classical Heisenberg Hamiltonian [188, 199]. This is then used for evaluating the Curie or Néel temperatures, the magnetic susceptibility and for interpreting neutron diffraction experiments [200].

Notably, the accuracy and reliability of the numerical values of the J's depend on the XC functional used, being the only approximated part of the DFT total energy [175]. Calculations based on local and semi-local functionals, namely the local density approximation (LDA) and the generalized gradient approximation (GGA), are successful with itinerant magnetism in transition metals [188], but largely over-estimates the Heisenberg exchange parameters in many other situations [191, 192, 193, 195, 198]. Additional corrections based on the kinetic energy density (metaGGA) [201] marginally improves the agreement with experiments [193], although an extensive investigation over several solid state systems has not been carried out so far.

This Chapter, therefore, is a contribution towards computing the exchange interaction for a number of prototypical materials, critical to local exchange and correlation functionals using the ASIC scheme. Despite the simplicity of the method, it has been applied with success to a number of interesting physical systems including , transition metal monoxides [202, 203], silver halides [204], noble metal oxides [205], ferroelectric materials [202, 206, 207], high-k materials [208], diluted magnetic semiconductors [209, 210] and also to quantum transport [211, 212].

As already pointed out in the previous Chapter, the method is strictly speaking not variational, in the sense that an energy functional generating the ASIC potential via variational principle is not available. However, since typically the LDA energy is a good approximation of the exact DFT energy, although the LDA potential is rather different from the exact KS potential, a "practical" definition of total energy can be provided. In this work we evaluate the ability of this approximated energy in describing exchange parameters for a variety of magnetic systems.

7.2 Results

All our results have been obtained with an implementation of the ASIC method [75, 76] based on the DFT code *Siesta* [162, 163, 164, 165]. In order to compare the exchange parameters obtained with different XC functionals we consider the LDA parameterization of Ceperly and Alder [213], the GGA functional obtained by combining Becke exchange [214] with Lee-Yang-Parr correlation [215] (BLYP), the nonempirical Purdew, Burke and Ernzerhof (PBE) GGA [216], and the ASIC scheme as implemented in reference [75, 76].

Calculations are performed for different systems critical to LDA and GGA, ranging from molecules to extended solids. These include hypothetical H-He atomic chains, the ionic solid $KNiF_3$ and the transition metal monoxides MnO and NiO. DFT total energy calculations are mapped onto an effective pairwise Heisenberg Hamiltonian

$$H_{\mathrm{H}} = -\sum_{\langle nm \rangle} J_{nm} \vec{S}_n \cdot \vec{S}_m \,, \tag{7.1}$$

where the sums runs over all the possible pairs of spins. In doing this we wish to stress that the mapping is a convenient way of comparing total energies of different magnetic configurations calculated with different functionals. In this spirit the controversy around using the spin-projected (Heisenberg mapping) or the non-projected scheme is immaterial [189, 217, 218].

7.2.1 H-He chain

As an example of molecular systems, we consider H-He monoatomic chains with an inter-atomic separation of 1.625 Å (see Figure 7.1). This is an important benchmark for DFT since the wave-function is expected to be rather localized and therefore to be badly described by local XC functionals. In addition the system is simple enough to be accessible by accurate quantum chemistry calculations, so that theoretical bench

marks exist.

As basis set we use two radial functions (double-ζ) for the s and p angular momenta of both H and He, while the density of the real-space grid converges the self-consistent calculation at 300 Ry. Here we consider all possible Heisenberg pa-

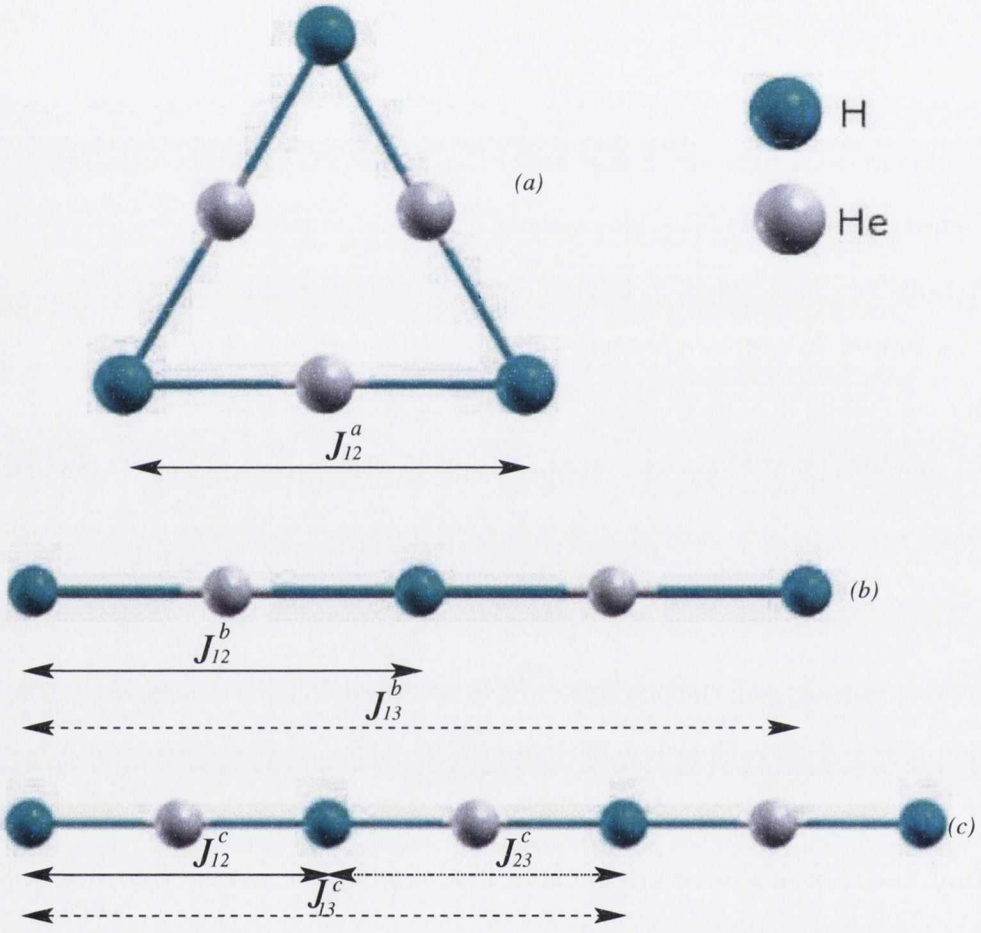

Figure 7.1: H-He-H chains at an inter-atomic distance of 1.625Å.

rameters. Thus the triangular molecule (Figure 7.1a) has only one nearest neighbour parameter J^a_{12}, the 5-atom chain (Figure 7.1b) has both first J^b_{12} and second neighbour J^b_{13} parameters, and the 7-atom chain (Figure 7.1c) has three parameters describing respectively the nearest neighbour interaction with peripheral atoms J^c_{12}, the nearest neighbour interaction between the two middle atoms J^c_{23} and the second neighbour interaction J^c_{13}. We have used the procedure proposed by Ruiz *et. al.* [196] for the

Method	J^a_{12}	J^b_{12}	J^b_{13}	J^c_{12}	J^c_{23}	J^c_{13}	δ (%)
CASPT2	-24	-74	-0.7	-74	-79	-0.7	0
SIC-B3LYP	-31	-83	-0.2	-83	-88	-0.3	16
LDA	-68	-232	-6	-234	-260	-6	210
PBE	-60	-190	-1.8	-190	-194	-1.6	152
BLYP	-62	-186	-2	-186	-200	-1	147
$ASIC_1$	-36	-112	-1	-110	-122	-0.6	51
$ASIC_{1/2}$	-44	-152	-1	-152	-168	-1.4	101
$ASIC^*_1$	-40	-128	-0.6	-128	-142	-1.0	73
$ASIC^*_{1/2}$	-50	-170	-1.4	-170	-190	-1.8	127

Table 7.1: Calculated J values (in meV) for the three different H–He chains shown in Fig.7.1. The CASPT2 values are from reference [196], while the SIC-B3LYP are from reference [189]. The last two rows correspond to J values obtained from the LDA energy calculated at the ASIC density.

theoretical estimation of J_{nm} with $S_n = 1/2$ in this case.

Following reference [189], accurate calculations based on second-order perturbation theory (CASPT2) [196] are used as comparison. The quality of each particular functionals is measured as the relative mean deviation of the nearest neighbour exchange parameters only (J^a_{12}, J^b_{12}, J^c_{12}, J^c_{23}), since those are the largest ones

$$\delta = \frac{1}{4}\sum_i^4 \frac{|J_i - J_i^{\mathrm{CASPT2}}|}{|J_i^{\mathrm{CASPT2}}|} \,. \tag{7.2}$$

Our calculated J values and their relative δ are presented in table 7.1, where we also include results for a fully self-consistent SIC calculation over the B3LYP functional (SIC-B3LYP) [189]. It comes without big surprise that the LDA systematically overestimates all the exchange parameters with errors up to a factor 6 for the smaller J (J^b_{13} and J^c_{13}) and an average error δ for the largest J of about 200%. Standard GGA corrections considerably improve the description although the J's are still systematically larger than those obtained with CASPT2. Note that the results seem rather independent of the particular GGA parameterization, with PBE and BLYB producing similar exchange constants. This is in good agreement with

previous calculations [189].

SIC in general dramatically improves the LDA and GGA description and our results for $ASIC_1$ are reasonably close to those obtained with the full self-consistent procedure (SIC-B3LYP). This is an interesting result, considering that our ASIC starts from a local exchange functional, while B3LYP already contains non-local contributions. We also evaluate the J parameters by using the LDA energy evaluated at the ASIC density (last two rows in table 7.1). In general this procedure gives J's larger than those obtained by using the energy of equation (6.21), meaning that the δ_n^{SIC} contributions reduce the J values.

It is then clear that the ASIC scheme systematically improves the J values as compared to local functionals. The agreement however is not as good as the one obtained by using a fully self-consistent SIC scheme, meaning that for this molecular system the ASIC orbitals are probably still not localized enough. This can alter the actual contribution of δ_n^{SIC} to the total energy and therefore the exchange parameters.

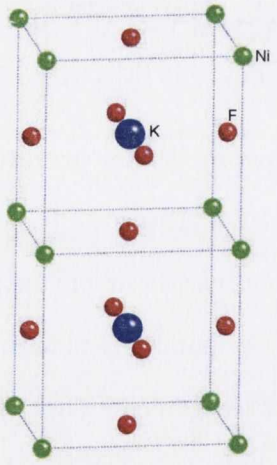

Figure 7.2: Cubic perovskite structure of $KNiF_3$. Color code: Green=Ni, Red=F, Blue=K.

7.2.2 Ionic antiferromagnets: $KNiF_3$

Motivated by the substantial improvement of ASIC over LDA, we then investigate its performances for real solid-state systems, starting from $KNiF_3$. This is a prototypical Heisenberg antiferromagnet with strong ionic character, a material for which our ASIC approximation is expected to work rather well [75]. It is also a well studied material, both experimentally [219, 220] and theoretically [221, 222, 191, 192], allowing us extensive comparisons. The $KNiF_3$ has cubic perovskite-like structure with the nickel atoms at the edges of the cube, fluorine atoms at the sides and potassium atoms at the center (see Figure 7.2). At low temperature, $KNiF_3$ is a type II antiferromagnetic insulator consisting of ferromagnetic (111) Ni planes aligned antiparallel to each other (see Figure 7.3 for the schematic representation of type II and type I antiferromagnetic ordering). For our calculations we use a double-ζ polarized basis for the s and p orbitals of K, Ni and F, a double-ζ for the $3d$ of K and Ni, and a single-ζ for the $3d$ of F. Finally, we use $5\times5\times5$ k-points in the full Brillouin zone and the real-space mesh cutoff is 550 Ry. Note that the configuration used to generate the pseudopotential is that of Ni^{2+}, $4s^1 3d^7$.

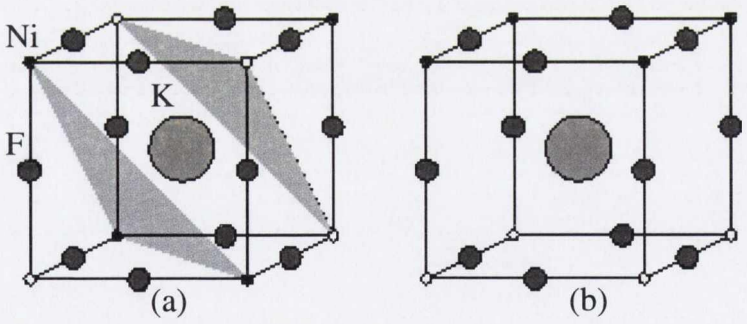

Figure 7.3: Unit cell of $KNiF_3$ for (a) type II and (b) type I antiferromagnetic phases. Black and white small spheres represent spin up and down Ni ions.

We first consider the band-structure as obtained with LDA and ASIC. For comparison we also include results obtained with LDA+U [78, 80] as implemented in *Siesta* [177]. In this case we correct only the Ni d shell and we fix the Hubbard-

U and Hund's exchange-J parameters by fitting the experimental lattice constant ($a_0 = 4.014$ Å). The calculated values are U=8 eV and J=1 eV. The bands obtained with the three methods and the corresponding orbital projected density of states (DOS) are presented in Figures 7.4 and 7.5 respectively. From the bands, the LDA introduces many more bands in the energy window considered when compared with those of ASIC and LDA+U. This is due to the way ASIC and LDA+U treat the unoccupied states as we already mentioned in last section of Chapter 6. LDA+U is able to correct the unoccupied states by shifting their orbital energies upward while ASIC only acts on the occupied orbitals which are shifted towards lower energies.

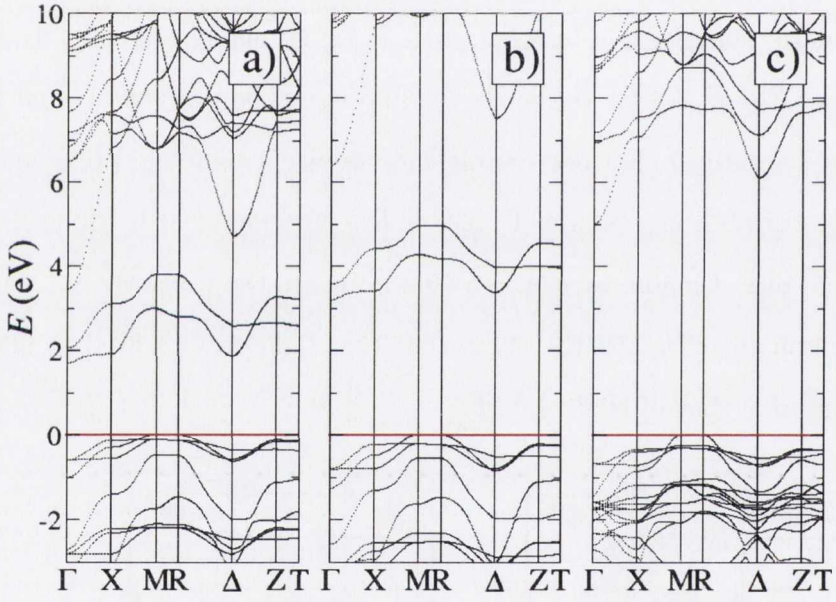

Figure 7.4: Band structure for type II antiferromagnetic $KNiF_3$ obtained with a) LDA, b) $ASIC_1$ and c) LDA+U (U=8 eV and J=1 eV). The valence band top is aligned at E=E_F=0 eV (horizontal line).

All the three functionals describe $KNiF_3$ as an insulator with bandgaps respectively of 1.68 eV (LDA), 3.19 eV ($ASIC_1$), and 5.0 eV (LDA+U). An experimental value for the gap is not available and therefore a comparison cannot be made. In the case of LDA and ASIC the gap is formed between Ni states, with conductance band bottom well described by e_g orbitals. These are progressively moved upwards

in energy by the SIC, but still occupy the gap. Such feature is modified by LDA+U which pushes the unoccupied e_g states above the conductance band minimum, which is now dominated by K 4s orbitals.

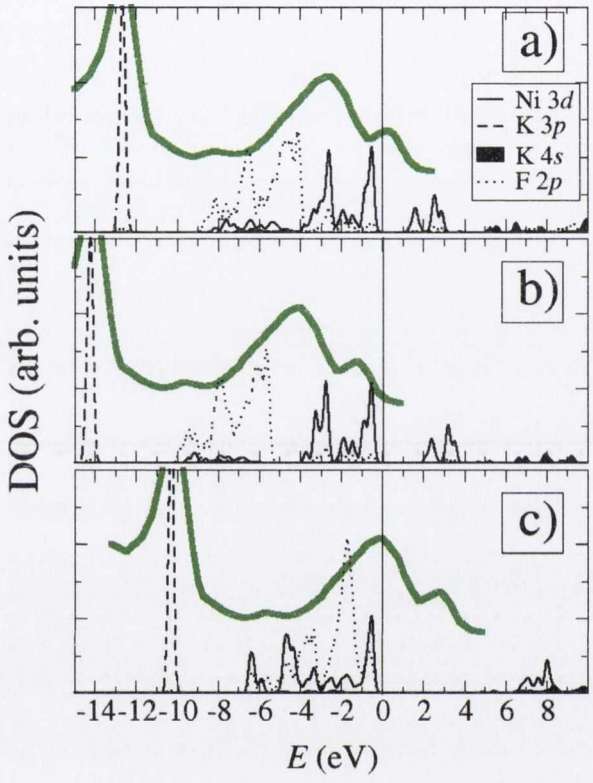

Figure 7.5: DOS for type II antiferromagnetic $KNiF_3$ obtained with a) LDA, b) $ASIC_1$ and c) LDA+U (U=8 eV and J=1 eV). The valence band top is aligned at E=0 eV (vertical line). The experimental UPS spectrum from reference [223] is also presented (thick green line). The relative binding energy is shifted in order to match the K 3p peak.

In more detail the valence band is characterized by a low-lying K 3p band and by a mixed Ni-3d/F 2p. While the K 3p band is extremely localized and does not present substantial additional orbital components the amount of mixing and the broadening of the Ni-3d/F 2p varies with the functionals used. In particular both LDA and ASIC predict that the Ni 3d component occupies the high energy part of the band, while the F 2p the lower. For both the total bandwidth is rather similar and it is about 9-10 eV. In contrast LDA+U offers a picture where the Ni-F hybridization spread

across the whole bandwidth, which is now reduced to less than 7 eV.

Experimentally, ultraviolet photoemission spectroscopy (UPS) study of the whole KMF_3 (M: Mn, Fe, Co, Ni, Cu, Zn) series [223] gives us a spectrum dominated by two main peaks: a low K $3p$ peak and broad band mainly attributed to F $2p$. These two spectroscopical features are separated by a binding energy of about 10 eV. In addition the 10 eV wide F $2p$ band has some fine structure related to various Ni d multiplets. An analysis based on averaging the multiplet structure [223] locates the occupied Ni d states at a bounding energy about 3 eV smaller than that of the F $2p$ band. In Figure 7.5, we superimpose the experimental UPS spectrum to our calculated DOS, with the convention of aligning in each case the sharp K $3p$ peak.

It is then clear that ASIC provides in general a better agreement with the UPS data. In particular both the Ni-$3d$/F $2p$ bandwidth and the position of the Fermi energy (E_F) with respect to the K $3p$ peak are correctly predicted. This is an improvement over LDA, which describes well the Ni-$3d$/F $2p$ band, but positions the K $3p$ states too close to E_F. For this reason, when we align the UPS spectrum at the K $3p$ position, this extends over E_F. Finally in the case of LDA+U, there is a substantial misalignment between the UPS data and our DOS. LDA+U in fact erroneously pushes part of the Ni d mainfold below the F $2p$ DOS, which now forms a rather narrow band.

We now turn our attention to total energy related quantities. In table 7.2 we present the theoretical equilibrium lattice constant a_0 and the Heisenberg exchange parameter J for all the functionals used. Experimentally we have J=8.2 $\pm$ 0.6 meV [219]. The values of a_0 and J are calculated for the type II antiferromagnetic ground state, by constructing a supercell along the (111) direction. Importantly values of J obtained by considering a supercell along the (100) direction, i.e. by imposing antiferromagnetic alignment between ferromagnetic (100) planes (type I antiferromagnet), yield essentially the same result, confirming the fact that the interaction is effectively

Method	a_0	J_{th}	P_d^{th}	J_{ex}	P_d^{ex}
LDA	3.951	46.12 (53.1)	1.829	40.4	1.834
PBE	4.052	33.98 (37.0)	1.813	36.48	1.808
BLYP	4.091	31.10 (37.6)	1.821	36.72	1.812
$\text{ASIC}_{1/2}$	3.960	40.83	1.876	36.14	1.878
ASIC_1	3.949	36.22	1.907	30.45	1.914
$\text{ASIC}^*_{1/2}$	3.969	43.44	1.876	38.57	1.878
ASIC^*_1	3.949	39.80	1.907	33.56	1.914
LDA+U	4.007	12.55		10.47	1.940

Table 7.2: Calculated J parameters (in meV) and the Mülliken magnetic moment for Ni $3d$ (P_d) in $KNiF_3$. The experimental values for J and a_0 are 8.2 ± 0.6 meV and 4.014Å respectively while the values in brackets are those from reference [193]. In the table we report values evaluated at the theoretical (J_{th} and P_d^{th}) and experimental (J_{ex} and P_d^{ex}) lattice constant. $\text{ASIC}^*_{1/2}$ and ASIC^*_1 are obtained from the LDA energies evaluated at the ASIC density.

only extending to nearest neighbors. Furthermore we report results obtained both at the theoretical equilibrium lattice constant (J_{th}) and at the experimental one (J_{ex}). Here, we have used the energy difference, ΔE, between the ferromagnetic and the antiferromagnetic state to extract J by using the following relation [221]:

$$\Delta E = 2zS^2J, \tag{7.3}$$

where z is the number of Ni second neighbours with opposite spin (6 and 2 for type I and type II antiferromagnets respectively) and S is the total spin moment ($S = 1$ in this present case).

Also in this case local XC functionals largely overestimate J, with errors for J_{ex} going from a factor 8 (LDA) to a factor 4.5 (GGA-type). ASIC improves these values, although only marginally, and our best agreement is found for ASIC_1, while $\text{ASIC}_{1/2}$ is substantially identical to GGA. Interestingly the ASIC_1 performance is rather similar, if not better, to that of meta-GGA functionals [193]. The situation is however worsened when we consider J parameters obtained at the theoretical lattice constant. The ASIC-calculated a_0 are essentially identical to those from LDA and

about 2% shorter than those from GGA. Since J depends rather severely on the lattice parameter we find that at the theoretical lattice constant GGA-functionals perform actually better than our ASIC. Finally, also in this case the J's obtained by simply using the LDA energies are larger than those calculated by including the SIC corrections (see equation 6.21).

In general the improvement of the J parameters is correlated to a higher degree of electron localization, in particular of the Ni d shell. In table 7.2 the magnetic moment of the Ni d shell, P_d, obtained from the Mülliken population, is reported. This increases systematically when going from LDA to GGA to ASIC approaching the atomic value expected from Ni^{2+}.

Our best result is obtained with LDA+U, which returns an exchange of 10.47 meV for the same U and J that fit the experimental lattice constant. This is somehow superior performance of LDA+U with respect to ASIC should not be surprising and it is partially related to an increased localization. The Ni ions d shell in octahedral coordination splits into t_{2g} and e_g states, which further split according to Hund's rule. The t_{2g} states are all filled, while for the e_g only the majority are. By looking at the LDA DOS one can recognize the occupied $t_{2g}^{\uparrow}$ orbitals (we indicate majority and minority spins respectively with $\uparrow$ and $\downarrow$) at -3 eV, the $e_g^{\uparrow}$ at -2 eV and the $t_{2g}^{\downarrow}$ at about 0 eV, while the empty $e_g^{\downarrow}$ are at between 1 and 3 eV above the valence band maximum.

The local Hund's split can be estimated from the $e_g^{\uparrow}$-$e_g^{\downarrow}$ separation. The ASIC scheme corrects only occupied states [224], and therefore it enhances the local exchange by only a downshift of the valence band. From the DOS of Figure 7.5 it is clear that this is only a small contribution. In contrast the LDA+U scheme also corrects empty states, effectively pushing upwards in energy the $e_g^{\downarrow}$ band. The net result is that of a much higher degree of localization of the d shell with a consequent reduction of the Ni-Ni exchange. This is similar to the situation described by

the Hartree-Fock method, which however returns exchange parameters considerably smaller than the experimental value [221, 222, 225, 226]. Interestingly hybrid functionals [191] have the right mixture of non-local exchange and electron correlation and produce J's in close agreement with the experiments.

We further investigate the magnetic interaction by evaluating J as a function of the lattice constant. Experimentally this can be achieved by replacing K with Rb and Tl, and indeed de Jongh and Block [227] early suggested a $d^{-\alpha}$ power law with $\alpha = 12 \pm 2$. Our calculated J as a function of the lattice constant d for LDA, GGA, $ASIC_1$ and LDA+U (U=8 eV and J=1 eV) are presented in Figure 7.6. For

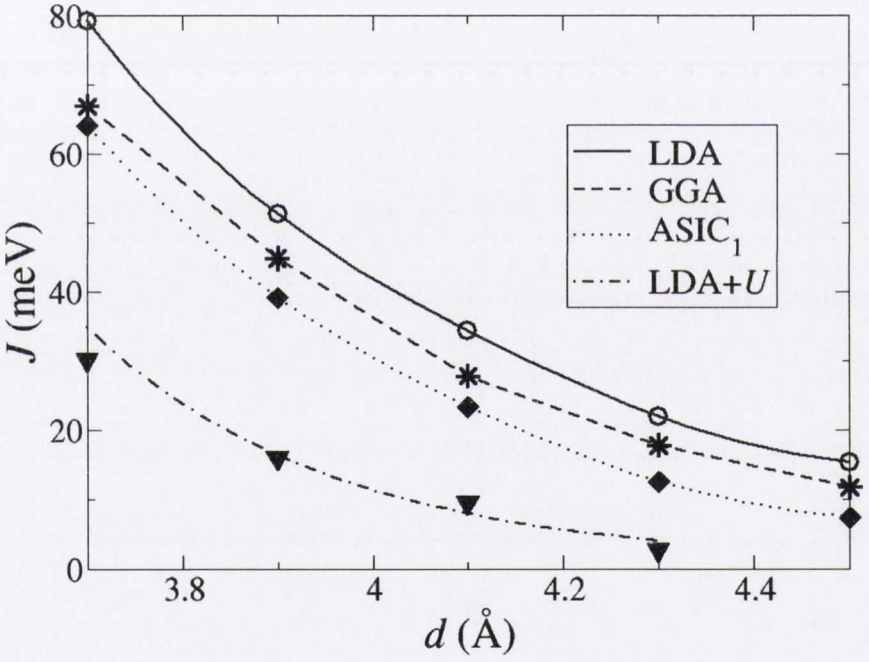

Figure 7.6: J as a function of the lattice constant for LDA, GGA, $ASIC_1$ and LDA+U (U=8 eV and J=1 eV). The symbols are our calculate value while the solid lines represent the best power-law fit.

all the four functionals investigated J varies as a power law, although the calculated exponents are rather different: 8.6 for LDA, 9.1 for GGA, 11.3 for $ASIC_1$ and 14.4 for LDA+U. This further confirms the strong underestimation of the exchange constants from local functionals. Clearly the relative difference between the J obtained with

different functionals becomes less pronounced for small d, where the hybridization increases and local functionals perform better. Note that only $ASIC_1$ is compatible with the experimental exponent of 12 ± 2, being the one evaluated from LDA+U too large. Importantly we do not expect to extrapolate the LDA+U value at any distance, since the screened U and J parameters change with the lattice constant.

In conclusion for the critical case of $KNiF_3$ the ASIC method appears to improve the LDA results. This is essentially due to the better degree of localization achieved by the ASIC as compared with standard local functionals. However, while the improvement over the bandstructure is substantial, it is only marginal for energy-related quantities. The main contribution to the total energy in the ASIC scheme comes from the LDA functional, which is now evaluated at the ASIC density. This is not sufficient for improving the exchange parameters, which in contrast need at least a portion of non-local exchange.

7.2.3 Transition metal monoxides

Another important test for the ASIC method is that of transition metal monoxides. These have been extensively studied both experimentally and theoretically and they are the prototypical materials for which the LDA appears completely inadequate. Here we consider MnO and NiO, which have respectively half-filled and partially-filled $3d$ shells. They both crystallize in the rock-salt structure and in the ground state they are both type-II antiferromagnetic insulators. The Néel's temperatures are 116 K and 525 K respectively for MnO and NiO. In all our calculations we consider double-ζ polarized basis for the s and p shell of Ni, Mn and O, double-ζ for the Ni and Mn $3d$ orbitals, and single-ζ for the empty $3d$ of O. We sample $6\times6\times6$ k-points in the full Brillouin zone of both the cubic and rhombohedral cell describing respectively type I and type II antiferromagnetism. Finally the real-space mesh cutoff is 500 Ry.

The calculated band structures obtained from LDA, $ASIC_{1/2}$ and $ASIC_1$ are

shown in Figures 7.7 and 7.8 for MnO and NiO respectively. These have been already discussed extensively in the context of the ASIC method [202, 75] and here we report only the main features. For both the materials LDA already predicts an insulating behavior, although the calculated gaps are rather small and the nature of the gaps is not what experimentally found. In both cases the valence band top has an almost pure d component, which suggests these materials to be small gap Mott-Hubbard insulators. The ASIC downshifts the occupied d bands, which now hybridize with the O-p manifold. The result is a systematic increase of the band-gap which is more pronounced as the parameter α goes from 1/2 to 1. Importantly, as noted already before [75], the experimental band-gap is obtained for $\alpha \sim 1/2$.

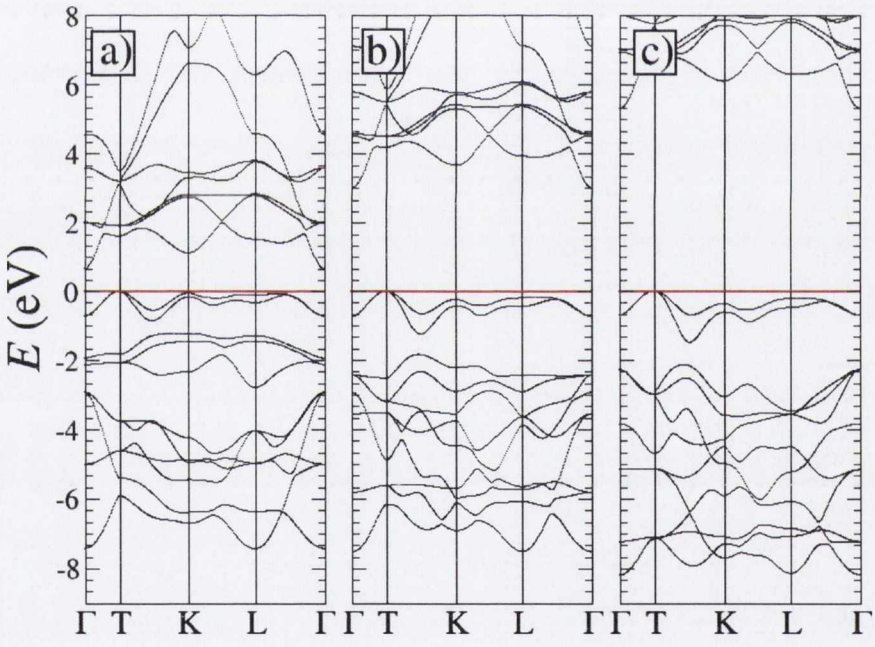

Figure 7.7: Calculated band structure for the type II anti-ferromagnetic MnO obtained from a) LDA, b) $ASIC_{1/2}$ and c) $ASIC_1$. The valence band top is aligned at 0 eV (horizontal line).

We then moved to calculating the exchange parameters. In this case we extend the Heisenberg model to second nearest neighbors, by introducing the first (J_1) and second (J_2) neighbor exchange parameters. These are evaluated from total energy

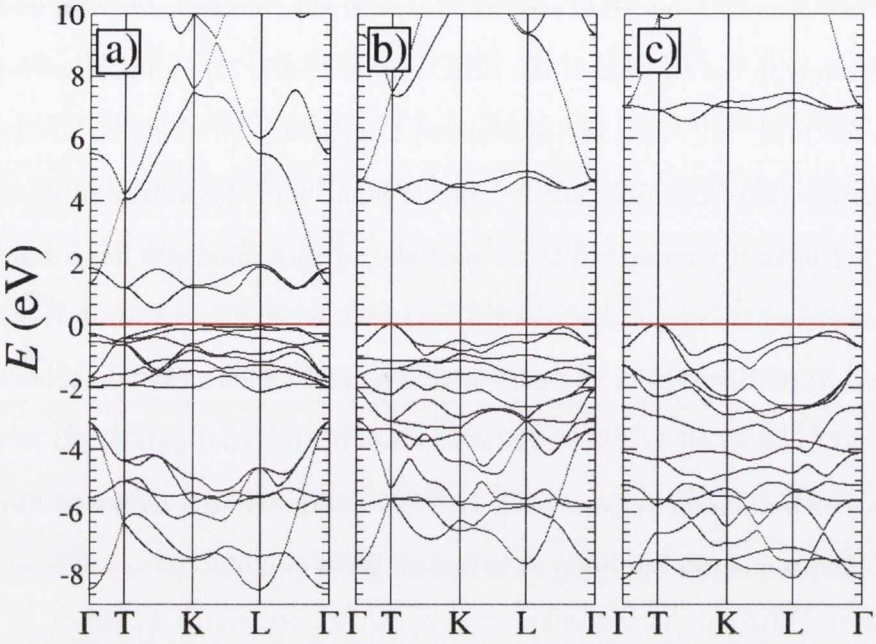

Figure 7.8: Calculated band structure for the type II anti-ferromagnetic NiO obtained from a) LDA, b) $ASIC_{1/2}$ and c) $ASIC_1$. The valence band top is aligned at 0 eV (horizontal line).

calculations for a ferromagnetic and both type II and type I antiferromagnetic alignments. It has been shown [194] that the Heisenberg Hamiltonian of the equation (7.1) reduces to

$$\begin{aligned} E^{FM} &= (6J_1 + 3J_2)S^2 \\ E^{AF1} &= (-2J_1 + 3J_2)S^2 \\ E^{AF2} &= -3J_2S^2, \end{aligned} \tag{7.4}$$

where E^{FM}, E^{AF1} and E^{AF2} are the ground state total energies of the ferromagnetic, type I antiferromagnetic and type II antiferromagnetic ordering respectively. The magnitude of the spin S is 5/2. Our calculated results, together with a few selected data available from the literature are presented in table 7.3.

Let us first focus our attention to MnO. In this case both the J's are rather small and positive (antiferromagnetic coupling is favorite), in agreement with the Goodenough-Kanamori rules [228] and the rather low Néel temperature. Direct

Method	MnO			NiO		
	J_1	J_2	P_d	J_1	J_2	P_d
LDA	1.0	2.5	4.49 (4.38)	13.0	-94.4	1.41 (1.41)
PBE	1.5	2.5	4.55 (4.57)	7.0	-86.8	1.50 (1.59)
$ASIC_{1/2}$	1.15	2.44	4.72 (4.77)	6.5	-67.3	1.72 (1.77)
$ASIC_1$	0.65	1.81	4.84 (4.86)	3.8	-41.8	1.83 (1.84)
$ASIC^*_{1/2}$	1.27	2.65	4.72 (4.77)	7.1	-74.6	1.72 (1.77)
$ASIC^*_1$	0.69	2.03	4.84 (4.86)	4.4	-47.9	1.83 (1.84)
SE1[a]	0.86	0.95				
HF[b]	0.22	0.36				
B3LYP[c]	0.81	1.71				
PBE0[b]	0.96	1.14				
B3LYP[d]				2.4	-26.7	
HF[d]				0.8	-4.6	
SIC-LDA[e]				2.3	-12	
Expt.[f]				1.4	-19.8	
Expt.[g]				1.4	-17.0	

Table 7.3: Calculated J_1 and J_2 in meV for MnO and NiO. P_d is the magnetic moment of the d shell calculated from the type II antiferromagnetic phase. Values in bracket are for P_d evaluated from the ferromagnetic ground state. $ASIC^*_{1/2}$ and $ASIC^*_1$ are obtained from the LDA energies evaluated at the ASIC density. a) Ref. [229], b) Ref. [230], c) Ref. [231], d) Ref. [195], e) Ref. [232], f) Ref. [234], g) Ref. [235]

experimental measurements of the exchange parameters are not available and the commonly accepted values are those obtained by fitting the magnetic susceptibility with semi-empirical methods [229]. Importantly this fit gives almost identical first and second nearest neighbour exchange constants. In contrast all the exchange functionals we have investigated offer a picture where J_2 is always approximately twice as large as J_1. This gives us a reasonably accurate value of J_1 for LDA and GGA, but J_2 is overestimated by approximately a factor 2, in agreement with previous calculations [194].

ASIC systematically improves the LDA/GGA description, by reducing both J_1 and J_2. This is related to the enhanced localization of the Mn d electrons achieved

by the ASIC, as it can be seen by comparing the Mn d magnetic moments (P_d) calculated for different functionals (see table 7.3). Thus $ASIC_1$, which provides the largest magnetic moment, gives also J's in closer agreement with the experimental values, while $ASIC_{1/2}$ is not very different from LDA.

Importantly for half-filling, as in MnO, the ASIC scheme for occupied states is fundamentally analogous to the LDA+U method, with the advantage that the U parameter does not need to be evaluated. Finally, at variance with $KNiF_3$, it does not seem that a portion of exact exchange is strictly necessary in this case. Hartree-Fock [230] results in a dramatic underestimation of the J parameters, while B3LYP [231] is essentially very similar to $ASIC_1$. Curiously the best results available in the literature [230] are obtained with the PBE0 functional [233], which combines 25% of exact-exchange with GGA.

The situation for NiO is rather different. The experimentally available data [234, 235] show antiferromagnetic nearest neighbour and ferromagnetic second nearest neighbour exchange parameters. The magnitude is also rather different with $|J_2| > 10\,|J_1|$. Standard local functionals (LDA and GGA) fail badly and overestimate both the J's by more than a factor 5. ASIC in general reduces the exchange constants and drastically improves the agreement between theory and experiments. In particular $ASIC_1$ gives exchange parameters only about twice as large as those measured experimentally.

A better understanding can be obtained by looking at the orbital-resolved DOS for the Ni d and the O p orbitals (Figure 7.9) as calculated from LDA and ASIC. There are two main differences between the LDA and the ASIC results. First there is an increase of the fundamental band-gap from 0.54 eV for LDA to 3.86 eV for $ASIC_{1/2}$ to 6.5 eV for $ASIC_1$. Secondly there is change in the relative energy positioning of the Ni d and O p contributions to the valence band. In LDA the top of the valence band is Ni d in nature, with the O p dominated part of the DOS lying between 4 eV

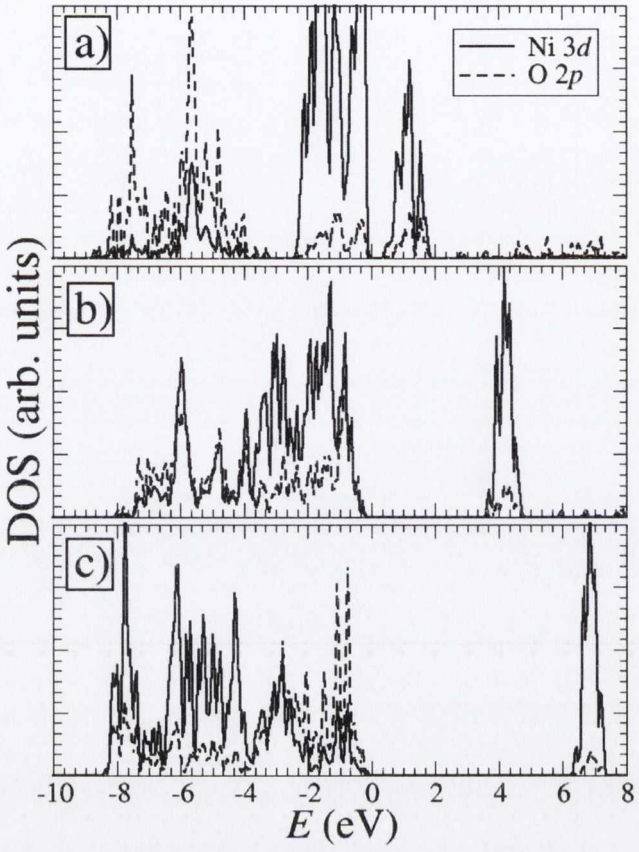

Figure 7.9: Calculated orbital resolved DOS for type II anti-ferromagnetic NiO obtained with a) LDA, b) $ASIC_{1/2}$ and c) $ASIC_1$. The valence band top is aligned at 0 eV.

and 8 eV from the valence band top. ASIC corrects this feature and for $ASIC_{1/2}$ the O p and Ni d states are well mixed across the whole bandwidth. A further increase of the ASIC corrections ($\alpha = 1$) leads to a further downshift of the Ni d band, whose contribution becomes largely suppressed close to the valence band-top. Thus, increasing the portion of ASIC pushes NiO further into the charge transfer regime.

Interestingly, although $ASIC_{1/2}$ gives the best bandstructure, the J's obtained with $ASIC_1$ are in better agreement with the experiments. This is somehow similar to what observed when hybrid functionals are put to the test. Moreira et al. demonstrated [195] that J's in close agreement with experiments can be obtained by using 35% Hartree-Fock exchange in LDA. Moreover, in close analogy to the ASIC

behaviour, as the fraction of exact exchange increases from LDA to purely Hartree-Fock, the exchange constants decrease while the band-gap gets larger. However, while the best J's are obtained with 35% exchange, a gap close to the experimental one is obtained with B3LYP, which in turns overestimates the J's. This remarks the subtile interplay between exchange and correlations in describing the magnetic interaction of this complex material. Finally, it is worth remarking that a fully self-consistent SIC [232] seems to overcorrect the J's, while still presenting the erroneous separation between the Ni d and O p states.

7.3 Summary

Here, the approximated ASIC total energy is put to the test in calculating the exchange parameters of a variety of materials, where local and gradient-corrected XC functionals fail rather badly. This has produced mixed results. On the one hand, the general bandstructure and in particular the valence band, is considerably improved and resembles closely available photo-emission data. On the other hand, the exchange constants are close to experiments only when the magnetism originates from half-filled shells. For other fillings, as in the case of NiO or $KNiF_3$ the ASIC improvement over LDA is less satisfactory, suggesting that a much better XC functional, incorporating a portion at least of exact exchange, is needed. Importantly ASIC seems to be affected by the same pathology of hybrid functional, i.e. the amount of ASIC needed for correcting the J is different from that needed for obtaining a good bandstructure.

Chapter 8

Summary and Outlook

8.1 Summary

Electronic correlation is an important feature of condensed matter systems responsible for fascinating physics in any dimension. In this dissertation, we have presented a range of theoretical methods to investigate electric and magnetic properties of one-dimensional and three-dimensional correlated systems. The first part was devoted to one-dimensional systems while the second focused on three-dimensional ones

8.1.1 Part I

The interest in one-dimensional structures stems from their possible practical realization with potential applications in molecular electronics. Indeed, carbon nanotubes and other quasi one-dimensional material exist and have already shown much promise in fields such as nanotechnology, electronics, optics, materials science, and architecture. Theoretical simulations are vital tools to investigate these systems as they can lead to a deeper understanding of the physics involved.

Experimentally observed properties of real systems are often described by theories based on underlying model Hamiltonians. For one-dimensional strongly correlated systems, the Hubbard model is usually adopted as a prototype. Here, the interplay

between Coulomb repulsion and kinetic energy produces an enormous variety of properties. In this work we have used lattice density functional theory (LDFT) within the Bethe Ansatz local density approximations (BALDA) to tackle Hubbard problem in 1D. Also, we have extended LDFT to current-LDFT (CLDFT), where a vector potential is included in the Hubbard Hamiltonian. We constructed a new exchange-correlation (XC) functional for a Hubbard ring enclosing a magnetic flux within the BALDA.

In contrast to other numerical techniques, the LDFT/CLDFT-BALDA offers the following advantages:

- **Easy to implement** - The simplicity of its implementation is striking. Immediately after the formalism is understood, the implementation of the code is straight forward.

- **Speed and resources** - LDFT/CLDFT-BALDA is an extremely fast method and does not require a huge amount of computer memory. It is well-suited to perform calculations over a wide range parameter space and system size.

- **Flexibility** - It is possible to describe the homogeneous and inhomogeneous cases by LDFT/CLDFT-LDA unlike the conventional BA that can only tackle homogeneous systems. Furthermore, both open and periodic boundary conditions can be efficiently explored.

Disadvantages include:

- **Approximate nature** - Due to the approximations in defining the unknown XC energy in the formulation of LDFT/CLDFT, the method still remains approximate.

- **Convergence issues close to the Mott-Insulator transition (MIT)** - Self-consistent convergence is difficult to reach for systems close to or at half-

filling as a result of the phase transition present in the homogeneous one-dimensional Hubbard model for that particular filling. This scenario means that the half-filling case must always be avoided in numerical calculations.

Despite these limitations, LDFT/CLDFT-BALDA is a very promising method to study zero-temperature properties of one-dimensional strongly correlated systems.

We have applied LDFT-BALDA to calculate the ground-state energies of the one-dimensional Hubbard model with both open and periodic boundary conditions. We used the two existing schemes in constructing an XC potential at the LDA level, namely BALDA/FN and BALDA/LSOC, and investigated a broad range of parameters such as the length of the chain, the number of electrons, the band fillings, the interaction strength and inhomogeneity. The ground state energies obtained by both the XC functionals are quite accurate and compare well with the results of well-established numerical methods like ED and DMRG. We find that the accuracy and convergence of the KS equations are not affected by the boundary conditions of the systems.

Consequently, we investigated two different physical properties with the DFT-BALDA functionals. The first one involves the response of one-dimensional metals to an external electric field. By using the ground state energy, we perform calculations for the linear polarizabilities, α, of 1D chains. The BALDA calculated values for α are compared with those obtained by ED and the DMRG, over a broad range of parameters. In general BALDA linear polarizabilities are in good agreement with the exact results. This agreement is particularly good in the case of BALDA/FN. Similarly, we show that the response of XC potentials are best described by the BALDA/FN where we obtain the interesting result that the potential response is always along the same direction of the perturbing potential, in contrast to what happens in *ab initio* DFT. We have also addressed the possible source of remaining error in the functionals which we attributed to the breakdown of the local approximation.

Secondly, with our extended scheme for the XC potential to CLDFT, we have studied a one-dimensional Hubbard ring threaded by a magnetic flux. We have calculated the ground state energy profile with the flux, from which equilibrium transport properties were estimated. The ground state energies of such a homogeneous Hubbard ring studied by CLDFT-BALDA have accuracies comparable to the BA and ED methods. We examined the performance of CLDFT-BALDA in predicting well known characteristics of persistent current and Drude weight with respect to the ring length, the band filling, the interaction strength and inhomogeneity. In all cases, the qualitative features are well reproduced while the results are as good as other many-body methods. However, the method encounters convergence problems close to the MIT or with significantly strong interactions which makes accuracy in those cases less satisfactory. Altogether, the comparison of ED and BA results proved that the CLDFT-BALDA captures the physics of Ahanorov-Bohm (AB) rings.

8.1.2 Part II

In this part, we have presented a systematic study of systems where correlations are important, by using an approximate self-interaction correction (SIC) scheme, namely Atomic SIC (ASIC) to DFT. In general, we have calculated the bandstructures of these systems by using the ASIC method. More specifically, exchange parameters, J, are extracted and compared to those calculated with other available theoretical methods as well as available experimental data. The bandstructures calculated by ASIC show that the quality of the valence band is enhanced and resembles closely available experimental data. In contrast, the exchange constants compare well to experiments only when magnetism arises from half-filled shells. We conclude that in order to obtain satisfactory estimates of J, a portion of exact exchange must be added to the XC functional.

8.2 Future work

Our calculations of the static linear polarizability have been carried out for a 1D Hubbard Hamiltonian in an electric field. One possible area of application for these calculations is in the field of ultracold fermions in optical lattices [25]. These systems bear close resemblance to correlated electron systems in condensed matter and have received considerable attention both experimentally and theoretically over the last decade. We plan to address the response of such systems in the presence of a harmonic confining potential. Numerical studies of the one-dimensional fermion-Hubbard model in harmonic traps within the LDFT [39, 41] and time-dependent LDFT [236] already exist in the literature. Our work will likely stimulate further interesting activity along the same lines.

In an attempt to correct for self-interaction errors in the XC energy, Vieira and Capelle have proposed three different approaches for the one-dimensional Hubbard model within the LDFT-BALDA [96]. One can, therefore, consider to include such a correction into the XC energy of the CLDFT-BALDA in order to offer much opportunity for improvement.

As we have mentioned in the introduction, the LDFT for strongly correlated systems has also been extended to time-dependent DFT (TDDFT) as pioneered by the work of Verdozzi [42]. This area however is still in an early stage (See references [42, 43]). While CLDFT, as we have discussed in Chapter 5, and TDDFT are two different theories that can be used to study strongly correlated one-dimensional systems, merging them into a single scheme, will be novel. A development in this direction would be the natural extension of this aspect of this thesis. This is of immediate interest for our future study.

Implementation of XC potentials which include full SIC and exact exchange into *Siesta* is currently in progress. It will be then interesting to observe their effects when estimating exchange parameters in future investigations. The only drawback

is that such methods are orbital dependent and so they are highly computationally expensive.

Bibliography

[1] N. W. Ashcroft and N. D. Mermin, *Solid State Physics*, Brooks Cole, 1976.

[2] J. Zaanen and O. Gunnarsson, Phys. Rev. B. **40**, R7391 (1989).

[3] N. F. Mott and R. Peierls, Proceedings of the Physical Society of London **49**, 72 (1937).

[4] N. F. Mott, Proceedings of the Physical Society of London Series A **62**, 416 (1949).

[5] J. T. Devreese, R. P. Evrard and V. E. van Doren, (eds) *Highly Conducting One-Dimensional Solids* (Plenum, New York, 1979).

[6] P. Fazekas *Lecture Notes on Electron Correlation and Magnetism* (World Scientific, Singapore 1999).

[7] A. R. Moodenbaugh, Youwen Xu, and M. Suenaga, T. J. Folkerts and R. N. Shelton, Phys. Rev. B **38**, 4596 (1988).

[8] L. D. Landau, Sov. Phys. JETP, **3**, 920 (1957), **5**, 101 (1957), **8**, 70 (1958).

[9] A. Troisi, Nature Mater. **8**, 538 (2009).

[10] F. D. M. Haldane, J. Phys. C. **14**, 2585 (1981); Phys. Rev. Lett. **47**, 1840 (1981).

[11] J. M. Luttinger, J. Math. Phys. **4** 609 (1963).

[12] T. Giamarchi, Chem. Rev. **104**, 5037 (2004).

[13] M. Bockrath, D. Cobden, J. Lu, A. Rinzler, R. Smalley, L. Balents, and P. McEuen, Nature **397**, 598 (1999).

[14] P. Segovia, D. Purdie, M. Hengsberger and Y. Baer, Nature **402**, 504 (1999).

[15] L. Venkataraman, Y. S. Hong, and P. Kim, Phys. Rev. Lett. **96**, 076601 (2006).

[16] S. Kagoshima, H. Hasegawa and T. Sambongi, *One Dimensional Conductors* (Springer, Berlin, 1987).

[17] See for example T. Giamarchi, *Quantum Physics in One Dimension*, First Edition, (Oxford University Press, 2004).

[18] J. D. Yuen, R. Menon, N. E. Coates, E. B. Namdas, S. Cho, S. T. Hannahs, D. Moses and A. J. Heeger, Nature Mater. **8**, 572 (2009).

[19] F. H. L Essler, H. Frahm, F. Göhmann, A. Klümper and V. E. Korepin, *The One-Dimensional Hubbard Model*, (Cambridge University Press, Cambridge (UK), 2005).

[20] M. C. Gutzwiller, Phys. Rev. Lett. **10**, 159 (1962).

[21] J. Hubbard, Proc. Roy. Soc. A **276**, 238 (1963), **277**, 237 (1964).

[22] J. Kanamory, Prog. Theor. Phys. **30**, 275 (1963).

[23] I. Bloch, J. Dalibard and W. Zwerger, Rev. Mod. Phys. **80**, 885 (2008); S. Giorgini, L. P. Pitaevskii and S. Stringari, Rev. Mod. Phys. **80**, 1212 (2008).

[24] L. Pezzà, L. Pitaevskii1, A. Smerzi, S. Stringari, G. Modugno, E. de Mirandes, F. Ferlaino, H. Ott, G. Roati, and M. Inguscio, Phys. Rev. Lett. **93**, 120401 (2004); M. Köhl, H. Moritz, T. Stöferle, K. Günter, and T. Esslinger, Phys. Rev. Lett. **94**, 080403 (2005).

[25] P. D. Drummond, J. F. Corney, A. J. Liu and H. Hu, J. Mod. Opt. **52**, 2261 (2005).

[26] F.H.L. Essler, H. Frahm, F. Göhmann, A. Klümper and V.E. Korepin, *The One-Dimensional Hubbard Model*, (Cambridge University Press, Cambridge, 2005).

[27] S. R. White, Phys. Rev. Lett. **69**, 2863 (1992).

[28] U. Schollwock, Rev. Mod. Phys. **77**, 259 (2005).

[29] O. Gunnarsson and K. Schonhammer, Phys. Rev. Lett. **56**, 1968 (1986).

[30] K. Schonhammer, O. Gunnarsson and R. M. Noack, Phys. Rev. B. **52**, 2504 (1995).

[31] P. Hohenberg and W. Kohn, Phys. Rev. **136**, B864 (1964).

[32] W. Kohn and L. J. Sham, Phys. Rev. **140**, A1133 (1965).

[33] R. Lopez-Sandoval and G. M. Pastor, Phys. Rev. B. **67**, 035115 (2003).

[34] N. A. Lima, L. N. Oliviera and K. Capelle, Euro. Phys. Lett. **60**, 601 (2002).

[35] N. A. Lima, L. N. Oliviera and K. Capelle, Phys. Rev. Lett. **90**, 146402 (2003).

[36] K. Capelle, N. A. Lima, M. F. Silva and L. N. Oliviera, in *The Fundamentals of Electron Density, Density Matrix and Density Functional theory in Atoms, Molecules and Solids*, Kluwer series, "Progress in Theoretical Chemistry and Physics," edited by N. I. Gidopoulos and S. Wilson (Kluwer, Dordrecht, 2003).

[37] M. F. Silva, N. A. Lima, A. L. Malvezzi, and K. Capelle, Phys. Rev. B. **71**, 125130 (2005).

[38] V. L. Campo, Jr. and K. Capelle, Phys. Rev. A. **72**, 061602(R) (2005).

[39] G. Xianlong, M. Polini, M.P. Tosi, V. L. Campo, K. Capelle and M. Rigol, Phys. Rev. B. **73**, 165120 (2006).

[40] G. Xianlong, M. Rizzi, M. Polini, R. Fazio, M.P. Tosi, V. L. Campo, and K. Capelle, Phys. Rev. Lett. **98**, 030404 (2007).

[41] G. Xianlong, Phys. Rev. B. **78**, 085108 (2008).

[42] C. Verdozzi, Phys. Rev. Lett. **101**, 166401 (2008).

[43] S. Kurth, G. Stefanucci, E. Khosravi, C. Verdozzi and E. K. U. Gross, Phys. Rev. Lett. **104**, 236801 (2010).

[44] S. Schenk, M. Dzierzawa, P. Schwab and U. Eckern, Phys. Rev. B. **78**, 165102 (2008).

[45] E. H. Lieb and F. Y. Wu, Phys. Rev. Lett. **20**, 1445 (1968), E. H. Lieb and F. Y. Wu, Physica A **321**, 1 (2003).

[46] S. Ishihara, M. Tachiki and T. Egami, Phys. Rev. B **49**, 16123 (1994); S. Ishihara, M. Tachiki and T. Egami, Phys. Rev. B **53**, 15563 (1996).

[47] A. G. Rojo and G. D. Mahan, Phys. Rev. B **47**, 1794 (1993); G. D. Mahan and A. G. Rojo, Phys. Rev. B **50**, 2642 (1994).

[48] A. Altland and B. Simons *Condensed Matter Field Theory* (Cambridge University Press, 2006).

[49] P. W. Anderson, Phys. Rev. **124**, 41 (1961).

[50] See for example A. C. Hewson, *The Kondo Problem to Heavy Fermions.* Cambridge University Press, New York, N. Y.,(1993).

[51] J. R. Schrieffer and P. A. Wolff, Phys. Rev. **149**, 491 (1966).

[52] R. Micnas, J. Ranninger and S. Robaszkiewicz, Rev. Mod. Phys. **62**, 113 (1990).

[53] S. Akbar Jafari, Iranian Journal of Physics Research **8**, 113 (2008), arXiv:0807.4878.

[54] G. F. Giuliani and G. Vignale, *Quantum Theory of the Electron Liquid* (Cambridge University Press, 2005).

[55] G. D. Mahan, *Many Particle Physics* (Plenum: New York, 1981).

[56] P. Nozières, *Interacting Fermi Systems*, (W. A. Benjamin Inc, New York 1964).

[57] A. A. Abrikosov, L. P. Gorkov, and I. E. Dzyaloshinski, *Quantum Field Theoretical Methods in Statistical Physics* (Pergamon Press, Oxford, 1965).

[58] H. A. Bethe, Z. Phys. **71**, 205 (1931).

[59] V. E. Korepin, N. M. Bogoliubov and A. G. Izergin, *Quantum Inverse Scattering Method and Correlation Functions* (Cambridge University Press, 1993).

[60] E. H. Lieb and W. Liniger, Phys. Rev. **130**, 1605 (1963), E. H. Lieb, Phys. Rev. **130**, 1616 (1963).

[61] C. N. Yang and C. P. Yang, Phys. Rev. **150**, 327 (1966), Phys. Rev. **151**, 258 (1966).

[62] R. J. Baxter, Phys. Rev. Lett. **26**, 834 (1971).

[63] T. B. Bahder and F. Woynarovich, Phys. Rev. B. **33**, 2114 (1986).

[64] F. Marsiglio, Phys. Rev. B. **55**, 575 (1997).

[65] C. Yang, A. N. Kocharian and Y. L. Chiang, J. Phys.: Condens. Matter **12**, 7433 (2000).

[66] R. O. Jones and O. Gunnarsson, Rev. Mod. Phys. **61**, 689 (1989).

[67] A. Szabo and N. S. Ostlund, *Modern Quantum Chemistry* (McGraw-Hill, New York, 1989).

[68] M. Levy, Proc. Natl Acad. Sci. USA, **76**, 6062 (1979). See also M. Levy, Phys. Rev. A **26**, 1200 (1982)

[69] E. Lieb, Int. J. Quantum Chem. **24**, 243 (1983).

[70] F. Block, Z. Physik **57**, 545 (1929), P. A. M. Dirac, Proc. Cambridge Phil. Soc. **26**, 376 (1930).

[71] M. Levy, J.P. Perdew, Phys. Rev. A **32**, 2010 (1985).

[72] J.P. Perdew, R.G. Parr, M. Levy, J.L. Balduz, Phys. Rev. Lett. **49**, 1691 (1982).

[73] A. D. Becke, J. Chem. Phys. **98**, 5648 (1993).

[74] J. P. Perdew and A. Zunger, Phys. Rev. B. **23**, 5048 (1981).

[75] C. D. Pemmaraju, T. Archer, D. Sanchez-Portal and S. Sanvito, Phys. Rev. B **75**, 045101 (2007).

[76] C. D. Pemmaraju, *PhD Thesis*, University of Dublin Trinity College (2007).

[77] A. Akande and S. Sanvito, J. Chem. Phys. **127**, 034112, (2007).

[78] V.I. Anisimov, F. Aryasetiawan and A.I.Lichtenstein, J. Phys.: Condens. Matter **9**, 767 (1997); V. I. Anisimov, J. Zaanen, and O. K. Andersen, Phys. Rev. B. **44**, 943 (1991); V. I. Anisomov, M. A. Korotin, J. A. Zaanen, and O. K. Anderson, Phys. Rev. Lett. **68**, 345 (1992).

[79] C. Tablero, J. Phys.: Condens. Matter **20**, 325205 (2008).

[80] M. T. Czyzyk and G. A. Sawatzsky, Phys. Rev. B **40**, 14211 (1994).

[81] C. Lanczos, J. Res. Nat. Bur. Stand. **45**, 255 (1950).

[82] E. Dagotto, Rev. Mod. Phys. **66**, 763 (1994).

[83] V. Hernández, J. E. Román, A. Tomás and V. Vidal, *SLEPc Technical Report STR-5*, (Universidad Politecnica de Valencia, 2006).

[84] C. C. Paige, J. Inst. Maths Applics, **18**, 341 (1976.).

[85] E. Anderson, Z. Bai, C. Bischof, J. Demmel, J. Dongarra, J. Du Croz, A. Greenbaum, S. Hammarling, A. McKenney, S. Ostrouchov, and D. Sorensen. *LAPACKs users guide.* Society for Industrial and Applied Mathematics, Philadelphia, PA, USA, 1992. Also available from http://www.netlib.org/lapack/.

[86] L. P. Kadanoff, Physics (Long Island City, N.Y.) **2**, 263 (1966).

[87] K. G. Wilson, Rev. Mod. Phys. **47**, 773 (1975).

[88] R. Bulla, T. A. Costi, and T. Pruschke, Rev. Mod. Phys. **80**, 395 (2008).

[89] H. R. Krishnamurthy, J. W. Wilkins and K. G. Wilson, Phys. Rev. B **21**, 1003 (1980)

[90] S. R. White and R. M. Noack, Phys. Rev. Lett. **68**, 3487 (1992).

[91] W. H. Press, B. P. Flannery, S. A. Teukolsky and W. T. Vetterling, *Numerical Recipes: The Art of Scientic Computing* (Cambridge University Press, Cambridge, 1987).

[92] E. Jeckelmann, Lecture note on Introduction to the density-matrix renormalization group (DMRG) (2006).

[93] *Density-Matrix Renormalization, A New Numerical Method in Physics*, edited by I. Peschel, X. Wang, M. Kaulke and K. Hallberg (Springer, Berlin, 1999).

[94] P. Fulde, *Electron Correlations in Molecules and Solids* (Springer, Berlin, 1991).

[95] W. Li, G. Xianlong, C. Kollath, and M. Polini, Phys. Rev. B. **78**, 195109 (2008).

[96] D. Vieira and K. Capelle, arXiv:0807.2816.

[97] E. R. Davidson, J. Comp. Phys **17**, 87 (1975); Computers in Physics **7**, No. 5, 519 (1993).

[98] P. Schlottmann, Int. J. Mod. Phys. B **11**, 355 (1997).

[99] A. N. Kocharian, C. Yang, and Y. L. Chiang, Phys. Rev. B. **59**, 7458 (1999).

[100] M. F. Silva, N. A. Lima, A. L. Malvezzi and K. Capelle, Phys. Rev. B. **71**, 125130 (2005).

[101] J. Silva-Valencia, E. Miranda and R. R. dos Santos, J. Phys.: Condens. Matter **13**, L619 (2001).

[102] T. Paiva, M. El. Massalami and R. R. dos Santos, J. Phys.: Condens. Matter **15**, 7917 (2003).

[103] F. Albuquerque et al., J. Magn. Magn. Mater. **310**, 1187 (2007).

[104] K. D. Bonin and V. V. Kresin, *Electric-dipole Polarizability of Atoms, Molecules and Clusters*, (World Scientific, Singapore, 1997).

[105] G. Maroulis, *Atoms, molecules and clusters in electric fields: Theoretical approaches to the calculation of electric polarizability*, (Imperial College Press, 2006).

[106] S. J. A. van Gisbergen, P. R. T. Schipper, O. V. Gritsenko, E. J. Baerends, J. G. Snijders, B. Champagne, and B. Kirtman, Phys. Rev. Lett. **83**, 694 (1997).

[107] S. Kmmel, L. Kronik and J.P. Perdew, Phys. Rev. Lett. **93**, 213002 (2004).

[108] T. Körzdörfer, M. Mundt and S. Kümmel, Phys. Rev. Lett. **100**, 133004 (2008).

[109] C. D. Pemmaraju, S. Sanvito and K. Burke, Phys. Rev. B **77**, 121204(R) (2008).

[110] C. O. Almbladh and A. C. Pedroza, Phys. Rev. A. **29**, 2322 (1984).

[111] U. von Barth, in *Many Body Phenomena at Surfaces*, D. Langreth and H. Suhl eds., Academic Press (1984)

[112] D. Karlsson, A. Privitera and C. Verdozzi, arXiv:1004.2264

[113] J. H. Davies, *The Physics of Low-Dimensional Semiconductor*, (Cambridge University Press, Cambridge, 1998).

[114] E. Zipper, M. Kurpas, M. Szelag, J. Dajka, and M. Szopa, Phys. Rev B **74**, 125426 (2006).

[115] P. Földi, O. Kálmán, M. G. Benedict, and F. M. Peeters, Phys. Rev. B **73**, 155325 (2006).

[116] A. Lorke, R. J. Luyken, A. O. Govorov, J. P. Kotthaus, J. M. Garcia and P. M. Petroff, Phys. Rev. Lett. **84**, 2223 (1999)

[117] A. Fuhrer, S. Lüsher, T. Ihn, T. Heinzel, K. Ensslin, W. Wegscheider and M. Bichler, Nature (London) **413**, 822 (2001)

[118] J. M Garcia, G. Medeiros-Ribeiro, K. Schmidt, T. Ngo, J. L. Feng, A. Lorke, J. Kotthaus and P. M. Petroff, Appl. Phys. Lett. **71**, 2014 (1997).

[119] A. Lorke and R. J. Luyken, Physica B **256**, 424 (1998).

[120] Y. Aharonov and D. Bohm, Phys. Rev. **115**, 485, (1959).

[121] L. P. Levy, G. Dolan, J. Dunsmuir and H. Bouchiat, Phys. Rev. Lett. **64**, 2074 (1990).

[122] M. Büttiker, Y. Imry and R. Landauer, Phys. Lett. A **96**, 365 (1983).

[123] F. Bloch, Phys. Rev. **137**, A787 (1965).

[124] F. Bloch, Phys. Rev. **166**, 415 (1968).

[125] M. Büttiker, Phys. Rev. B **32**, 1846(R) (1985).

[126] G. Queeroz-Pallegrino, J. Phys.: Condens. Matter **13** 8121 (2001).

[127] S. Kirchner, H.G Evertz and W. Hanke, PRB **59** 1825 (1999).

[128] R.A. Molina, D. Weinmann, R.A. Jalabert, G. Ingold and J. Pichard, Phys. Rev. B **67** 235306 (2003).

[129] S. K. Maiti, J. Chowdhury and S.N. Karmakar Phys. Lett. A **332** 497 (2004).

[130] T. Giamarchi and B. Sriram Shastry, Phys. Rev. B. **51**, 10915 (1995).

[131] E. B. Kolomeisky and J. P. Straley, Rev. Mod. Phys. **68**, 175 (1996).

[132] S. Viefers, P. Koskinen, P. Singha Deo, M. Manninen, Physica E **21**, 1 (2004).

[133] G. Bouzerar, D. Poiblanc and G. Montambaux, Phys. Rev. B **49**, 8258 (1994).

[134] V. Meden and U. Schollwöck, Phys. Rev. B **67**, 035106 (2003).

[135] F. C. Dias, I. R. Pimentel, and M. Henkel, Phys. Rev. B **73**, 075109 (2006).

[136] A. Cohen, K. Richter and R. Berkovits, Phys. Rev. B **57**, 6223 (1998).

[137] A. O. Gogolin and N. V. Prokofev, Phys. Rev. B **50**, 4921 (1994).

[138] S. Jaimungal, M. H. S. Amin and G. Rose, Int. J. Mod. Phys. B **13**, 3171 (1999)

[139] S. Viefers, P. Singha Deo, S. M. Reimann, M. Manninen and M. Koskinen, Phys. Rev. B **62**, 10668 (2000).

[140] F. Pederiva, A. Emperador, and E. Lipparini, Phys. Rev. B **66**, 165314 (2002).

[141] A. Akande and S. Sanvito, Phys. Rev. B **82**, 245114 (2010).

[142] M. Dzierzawa, U. Eckern, S. Schenk, and P. Schwab, Phys. Status Solidi B **246**, 941 (2009).

[143] Q. P. Li and X. C. Xie, Phys. Rev. B. **49**, 8273 (1994).

[144] H-F. Cheung, Y. Gefen, E. K. Riedel and W. H. Shih, Phys. Rev. B **37**, 6050 (1988).

[145] C. A. Stafford and A. J. Millis, Phys. Rev. B **48**, 1409 (1993).

[146] R. A. Römer and A. Punnoose, Phys. Rev. B **52**, 14809 (1995).

[147] B.-B. wei, S.-J. Gu and H.-Q. Lin, J. Phys.: Condens. Matter **20**, 395209 (2008).

[148] B. S. Shastry and B. Sunderland, Phys. Rev. Lett. **65**, 243 (1990).

[149] R. Peierls, Z. Phys. **80**, 763 (1933).

[150] M. Graf and P. Vogl, Phys. Rev. B **51**, 4940 (1995).

[151] W. Kohn, Phys. Rev **133** A171 (1964).

[152] N. Byers and C. N. Yang, Phys. Rev. Lett. **7** 46 (1961).

[153] F. V. Kusmartsev, J. Phys.: Condens. Matter **3** 3199 (1991).

[154] H. Frahm and V. E. Korepin, Phys. Rev. B **43**, 5653 (1991).

[155] N. Kawakami ans S-K Yang, Phys. Rev. B **44**, 7844 (1991).

[156] G. F. Giuliani and G. Vignale,*Quantum Theory of the Electron Liquid*, (Cambridge University Press, Cambridge (UK), 2005).

[157] G. Vignale and M. Rasolt, Phys. Rev. lett. **59**, 2360 (1987).

[158] G. Vignale and M. Rasolt, Phys. Rev. B. **37**, 10685 (1988).

[159] F. Nakano, J. Phys. A: Math. Gen. **33**, 5429 (2000).

[160] P. Koskinen and M. Manninen, Phys. Rev. B. **68**, 195304 (2003).

[161] P. Schmitteckert, T. Schulze, C. Schuster, P. Schwab, and U. Eckern, Phys. Rev. Lett. **80**, 560 (1998).

[162] J. M. Soler, E. Artacho, J. D. Gale, A. Garcia, J. Junquera, P. Ordejon, and D. Sanchez-Portal, J. Phys.: Condens. Matter **14**, 2745 (2002).

[163] E. Artacho, E. Anglada, O Dieguez, J. D. Gale, A. Garcia, J. Junquera, R. M. Martin, P. Ordejon, J. M. Pruneda, D. Sánchez-Portal and J. M. Soler, J. Phys.: Condens. Matter **20** 064208 (2008).

[164] P. Ordejon, Comput. Mater. Sci. **12**, 157 (1998).

[165] P. Ordejon, E. Artacho, and J. M. Soler, Phys. Rev. B **53**, 10441 (1996).

[166] R. M. Martin, *Electronic Structure: Basic Theory and Practical Methods*, (Cambridge University Press, Cambridge (UK), 2004).

[167] M. C. Payne, M. P. Teter, D. C. Allan, T. A. Arias and J. D. Joannopoulos, Rev. Mod. Phys. **64**, 1045 (1992).

[168] L. Kleinman and D. M. Bylander, Phys. Rev. lett. **48**, 1425 (1982).

[169] N. Troullier and J. L. Matins, Phys. Rev. B **43**, 1993 (1991).

[170] E. Artacho, D. Sánchez-Portal, P. Ordejón, A. García and J.M. Soler. Phys. Status Solidi B, **215**, 809 (1999).

[171] O. F. Sankey and D. J. Niklewski. Phys. Rev. B, **40**, 3979 (1989).

[172] S. Huzinaga, ed., *Gaussian Basis Sets for Molecular Calculations* (Elsevier Publishing Company, Amsterdam, 1991), 1st ed.

[173] P. Pulay, Chem. Phys. Lett. **73**, 393 (1980)

[174] H. J. Monkhorst and J. D. Pack, Phys. Rev. B **13**, 5188 (1976).

[175] R.G. Parr and W. Yang, *Density Functional Theory of Atoms and Molecules.*, (Oxford University Press, New York 1989).

[176] J.P. Perdew, S. Kurth, A. Zupan and P. Blaha, Phys. Rev. Lett. *82*, 2544 (1999).

[177] M. Wierzbowska, D. Sánchez-Portal and S. Sanvito, Phys. Rev. B **70**, 235209 (2004).

[178] Note that here we use "LDA" also to refer to the local spin density approximation (LSDA), i.e. to the spin unrestricted version of the theory.

[179] J.G. Harrison, R.A. Heaton and C.C. Lin, J. Phys. B: At. Mol. Phys. **16**, 2079 (1983).

[180] M.R. Pederson, R.A. Heaton and C.C. Lin, J. Chem. Phys. **80**, 1972 (1984).

[181] M.R. Pederson, R.A. Heaton and C.C. Lin, J. Chem. Phys. **82**, 2688 (1985).

[182] A. Svane and O. Gunnarsson, Phys. Rev. Lett. **65**, 1148 (1990).

[183] Z. Szotek, W.M. Temmerman and H. Winter, Phys. Rev. B **47**, 4029 (1993).

[184] R. S. Mülliken, J. Chem. Phys. **23**, 1833 (1955), F.M. Bickelhaupt, N. J. R. van Eikema Hommes, C. Fonseca Guerra and E.J. Baerends. Organometallics **15**, 2923 (1996).

[185] L. Hedin, Phys. Rev. **139**, A796 (1965).

[186] H. Jiang, R. I. Gomez-Abal, P. Rinke, and M. Scheffler, Phys. Rev. B **82**, 045108 (2010).

[187] W. Kock and M. C. Holthausen, *A Chemist's Guide to Density Functional Theory*, (Wiley-VCH, Weinheim, 2000).

[188] I. Turek, J. Kudronovsky, V. Drchals and P. Bruno, Phil. Mag. **86**, 1713 (2006).

[189] E. Ruiz, S. Alvarez, J. Cano, and V. Polo, J. Chem. Phys. **123**, 164110 (2005).

[190] E. Ruiz, J. Cano, S. Alvarez, and P. Alemany, J. Comput. Chem. **20**, 1391 (1999).

[191] R. L. Martins and F. Illas, Phys. Rev. Lett. **79**, 1539 (1997).

[192] F. Illas and R. L. Martins, J. Chem. Phys. **108**, 2519 (1998).

[193] I. Ciofini, F. Illas and C. Adamo, J. Chem. Phys. **120**, 3811 (2004).

[194] J. E. Pask, D. J. Singh, I. I. Mazin, C. S. Hellberg and J. Kortus, Phys. Rev. B **64**, 024403 (2001).

[195] I. de P. R. Moreira, F. Illas, and R. Martin, Phys. Rev. B **65**, 155102 (2002).

[196] E. Ruiz, A. Rodriguez-Fortea, J. Cano, S. Alvarez and P. Alemany, J. Comput. Chem. **24**, 982 (2003).

[197] J. Cabrero, N. Ben Amor, C. de Graaf, F. Illas and R. Caballol, J. Phys. Chem. A **104**, 9983 (2000).

[198] A. Bencini, F. Totti, C. A. Daul, K. Doclo, P. Fantucci, and V. Barone, Inorg. Chem. **36**, 5022 (1997).

[199] L. Noodleman, J. Chem. Phys. **74**, 5737 (1981).

[200] K. Yosida, *Theory of Magnetism*, Vol. 122 Springer Series in Solid State Sciences (Springer, Heidelberg, 1992).

[201] J. Tao, J.P. Perdew, V.N. Staroverov and G.E. Scuseria, Phys. Rev. Lett. **91**, 146401 (2003).

[202] A. Filippetti and N. A. Spaldin, Phys. Rev. B **67**, 2435 (2003).

[203] A. Filippetti and V. Fiorentini, Phys. Rev. Lett. **95**, 086405 (2005).

[204] D. Vogel, P. Krüger and J. Pollmann, Phys. Rev. B **58**, 3865 (1998).

[205] A. Filippetti and V. Fiorentini, Rev. B **73**, 035128 (2005).

[206] A. Filippetti and N.A. Spaldin, Phys. Rev. B **68**, 045111 (2003).

[207] B.B. Van Aken, T.T.M.A. Palstra, A. Filippetti and N.A. Spaldin, Nature Mat. **3**, 164 (2003).

[208] P. Delugas, V. Fiorentini and A. Filippetti, Phys. Rev. B **71**, 134302 (2005).

[209] A. Filippetti, N.A. Spaldin and S. Sanvito, Chem. Phys. **309**, 59 (2005).

[210] A. Filippetti, N.A. Spaldin and S. Sanvito, J. Magn. Magn. Mater. **290**, 1391 (2005).

[211] C. Toher, A. Filippetti, S. Sanvito and K. Burke, Phys. Rev. Lett. **95**, 146402 (2005).

[212] C. Toher and S. Sanvito, Phys. Rev. Lett. **99**, 056801 (2007).

[213] D.M. Ceperley and B.J. Alder, Phys. Rev. Lett. **45**, 566 (1980).

[214] A. D. Becke, Phys. Rev. A **38**, 3098 (1988).

[215] C. Lee, W. Yang and R. G. Parr, Phys. Rev. B **37**, 785 (1988).

[216] J. P. Perdew, K. Burke and M. Ernzerhof, Phys. Rev. Lett. **77**, 3865 (1996).

[217] C. Adamo, V. Barone, A. Bencini, R. Broer, M. Filatov, N.M. Harrison, F. Illas, J.P. Malrieu, and I. de P.R. Moreira, J. Chem. Phys. **124**, 107101 (2006).

[218] E. Ruiz, S. Alvarez, J. Cano, and V. Polo, J. Chem. Phys. **124**, 107102 (2006).

[219] M. E. Lines, Phys. Rev. **164**, 736 (1967).

[220] L. J. de Jongh and R. Miedema, Adv. Phys. **23**, 1 (1974).

[221] R. Dovesi, J. M. Ricart, V. R. Saunders and R. Orlando, J. Phys.: Condens. Matter **7**, 7997 (1995).

[222] I. de P. R. Moreira and F. Illas, Phys. Rev. B **55**, 4129 (1997).

[223] H. Onuki, F. Sugawara, M. Hirano and Y. Yamaguchi, J. Phys. Soc. Jpn. **49**, 2314 (1980).

[224] The ASIC method is not completely self-interaction free and therefore some spurious corrections to the unoccuplied KS states are present.

[225] J. M. Ricart, R. Dovesi, C. Roetti and V. R. Saunders, Phys. Rev. B **52**, 2381 (1995).

[226] R. Caballol, O. Castell, F. Illas, I. de P. R. Moreira and J. P. Malrieu, J. Phys. Chem. A **101**, 7860 (1997).

[227] L.J. de Jongh and R. Block, Physica **79B**, 568 (1975).

[228] J. Goodenough, *Magnetism and the Chemical Bond*, (John Wiley and Sons, New York, 1963).

[229] M. E Lines and E. D. Jones, Phys. Rev. **139**, A1313 (1965).

[230] C. Franchini, V. Bayer, R. Podloucky, J. Paier and G. Kresse, Phys. Reb. B **72**, 045132 (2005).

[231] X. Fenf, Phys. Rev. B **69**, 155107 (2004).

[232] D. Ködderitzsch, W. Hergert, W.M. Temmerman, Z. Szotek, A. Ernst and H. Winter, Phys. Rev. B **66**, 064434 (2002).

[233] M. Ernzerhof and G.E. Scuseria, J. chem. Phys. **110**, 5029 (1999).

[234] M. T. Hutching and E. J. Samuelsen, Phys. Rev. B **6**, 3447 (1972).

[235] R. Shanker and R. A. Singh, Phys. Rev. B **7**, 5000 (1973).

[236] D. Karlsson, C. Verdozzi, M. M. Odashima and K. Capelle, Europhysics Letters **93**, 23003 (2011).

Appendix A

The non-interacting fermion gas

In the case of $U = 0$, the $\hat{H}_U$ reduces to

$$\hat{H}_{U=0} = -t \sum_{\sigma} \sum_{\langle ij \rangle}^{L} (\hat{c}^{\dagger}_{i\sigma} \hat{c}_{j\sigma} + hc), \tag{A.1}$$

where L represents the total number of lattice sites. The operators $\hat{c}^{\dagger}_{i\sigma}$ and $\hat{c}_{i\sigma}$ obey anti-commutation relations for fermions, i.e.

$$\begin{aligned} \{\hat{c}^{\dagger}_{i\sigma}, \hat{c}^{\dagger}_{j\sigma'}\} =& \hat{c}^{\dagger}_{i\sigma} \hat{c}^{\dagger}_{j\sigma'} + \hat{c}^{\dagger}_{j\sigma'} \hat{c}^{\dagger}_{i\sigma} = 0 \\ \{\hat{c}_{i\sigma}, \hat{c}_{j\sigma'}\} =& \hat{c}_{i\sigma} \hat{c}_{j\sigma'} + \hat{c}_{j\sigma'} \hat{c}_{i\sigma} = 0 \\ \{\hat{c}_{i\sigma}, \hat{c}^{\dagger}_{j\sigma'}\} =& \hat{c}_{i\sigma} \hat{c}^{\dagger}_{j\sigma'} + \hat{c}^{\dagger}_{j\sigma'} \hat{c}_{i\sigma} = \delta_{ij} \delta_{\sigma\sigma'}. \end{aligned} \tag{A.2}$$

We can expand these operator in form of a new set of operators, $\hat{c}^{\dagger}_{k\sigma}$ and $\hat{c}_{k\sigma}$,

$$\begin{aligned} \hat{c}_{j\sigma} =& \frac{1}{\sqrt{L}} \sum_{k} \hat{c}_{k\sigma} e^{ikj} \\ \hat{c}^{\dagger}_{j\sigma} =& \frac{1}{\sqrt{L}} \sum_{k} \hat{c}^{\dagger}_{k\sigma} e^{-ikj}, \end{aligned} \tag{A.3}$$

where the quasi-momentum k takes L in-equivalent values in the Brillouin zone $-\pi \leq k \leq \pi$. This expansion is nothing but a Fourier transformation from the real

to reciprocal space. The new operators also satisfy the canonical anti-commutation relations (A.2). The relations (A.3) can be inverted:

$$\begin{aligned} \hat{c}_{k\sigma} &= \frac{1}{\sqrt{L}} \sum_k \hat{c}_{j\sigma} e^{-ikj} \\ \hat{c}^\dagger_{k\sigma} &= \frac{1}{\sqrt{L}} \sum_k \hat{c}^\dagger_{j\sigma} e^{ikj}. \end{aligned} \tag{A.4}$$

By substituting equation (A.3) into (A.1) and by using

$$\sum_j e^{i(k-k')j} = L\delta_{kk'} \quad \text{and} \quad \sum_{k \in BZ} e^{i(j-j')k} = L\delta_{jj'}, \tag{A.5}$$

$\hat{H}_{U=0}$ then becomes diagonal:

$$\hat{H}_{U=0} = \sum_\sigma \sum_k \varepsilon(k) \hat{c}^\dagger_{k\sigma} \hat{c}_{k\sigma}, \tag{A.6}$$

where

$$\varepsilon(k) = -2t \cos k. \tag{A.7}$$

The expression (A.7) describes a single electron band in the tight-binding approximation. For a one-dimensional lattice of L sites with periodic boundary condition, $k = 2\pi n/L$ where $n = -L/2 + 1, ..., 0, ..., L/2$.

Appendix B

Exact spin-polarized XC potential for 1D repulsive Hubbard model

The XC potential $\mathcal{V}_{xc,\sigma}^{hom}(n,m,t,U)$ of the homogeneous HM is written as

$$\mathcal{V}_{xc,\sigma}^{hom}(n,m,t,U) = \frac{\partial E}{\partial n_\sigma} \equiv \frac{\partial E}{\partial n}\frac{\partial n}{\partial n_\sigma} + \frac{\partial E}{\partial m}\frac{\partial m}{\partial n_\sigma}, \tag{B.1}$$

where $E = e(n,m,t,U) - e(n,m,t,U=0) - e_H(n,m,U)$. $\frac{\partial E}{\partial n}$ and $\frac{\partial E}{\partial m}$ are determined by

$$\frac{\partial E}{\partial \zeta} = -2t\int_{-Q}^{Q} dk \rho_\zeta(k)\cos k - 4tQ_\zeta\rho(Q)\cos Q + \Delta\mathcal{V}_{KH}^{\zeta} \tag{B.2}$$

ζ being either n or m. $\rho_\zeta(k) \equiv \partial\rho(k)/\partial\zeta$ and $\sigma_\zeta(\lambda) \equiv \partial\sigma(\lambda)/\partial\zeta$ satisfy the following integral equations:

$$\begin{aligned}\rho_\zeta(k) = &\cos k\int_{-B}^{B} d\lambda\sigma_\zeta(\lambda)K_1(\sin k - \lambda) \\ &+ \cos k[K_1(\sin k - B) + K_1(\sin k + B)]\sigma(B)B_\zeta,\end{aligned} \tag{B.3}$$

$$\begin{aligned}\sigma_\zeta(\lambda) = &\int_{-Q}^{Q} dk \rho_\zeta(k) K_1(\sin k - \lambda) - \int_{-B}^{B} d\lambda' \sigma(\lambda') K_2(\lambda - \lambda') \\ &+ [K_1(\sin Q - \lambda) + K_1(-\sin Q - \lambda)]\rho(Q) Q_\zeta \\ &- [K_2(\lambda - B) + K_2(\lambda + B)]\sigma(B) B_\zeta,\end{aligned} \tag{B.4}$$

and $Q_\zeta \equiv \partial Q/\partial\zeta$ and $B_\zeta \equiv \partial B/\partial\zeta$ are determined from the relations,

$$\int_{-Q}^{Q} \rho_\zeta(k) dk + 2\rho(Q) Q_\zeta = \frac{\partial n}{\partial \zeta}, \tag{B.5}$$

$$\int_{-B}^{B} \sigma_\zeta(\lambda) d\lambda + 2\sigma(B) B_\zeta = \frac{\partial[(n-m)/2]}{\partial \zeta}. \tag{B.6}$$

From equations (B.5) and (B.6), one can write

$$\begin{aligned} Q_\zeta &= \frac{1}{2\rho(Q)} \left(\frac{\partial n}{\partial \zeta} - \int_{-Q}^{Q} \rho_\zeta(k) dk \right) \\ B_\zeta &= \frac{1}{2\sigma(B)} \left(\frac{\partial[(n-m)/2]}{\partial \zeta} - \int_{-B}^{B} \sigma_\zeta(\lambda) d\lambda \right). \end{aligned} \tag{B.7}$$

Substituting equation (B.7) into (B.3) and (B.4) gives two coupled integral equations which can be solved to obtain the full numerical computation of the spin dependent XC potential. Finally,

$$\begin{aligned} \Delta\mathcal{V}^n_{KH} &= 2t \cos\left(\frac{n\pi}{2}\right) \cos\left(\frac{m\pi}{2}\right) - \frac{Un}{2} \\ \Delta\mathcal{V}^m_{KH} &= -2t \sin\left(\frac{n\pi}{2}\right) \sin\left(\frac{m\pi}{2}\right) + \frac{Um}{2}. \end{aligned} \tag{B.8}$$

Appendix C

Local Density Approximation for the CLDFT

We will use the BA solutions of $\hat{H}_U^{\Phi}$ to estimate the XC energy and then locally approximate the densities and currents, i.e.

$$E_{LDA}^{xc}[n_l, j_l] = \sum_l e^{xc}[n_l, j_l], \tag{C.1}$$

where $e^{xc}(= \frac{E^{xc}[n,j]}{L})$ is the XC energy per site in the homogeneous system. The first term of the equation (5.57) can be calculated exactly using the BA procedures [148] to obtain the ground state energy as a function of n and Φ. The phase variable Φ can be eliminated from the ground state energy to contain the current via

$$j = \frac{\partial E(n, \Phi)}{\partial \Phi}. \tag{C.2}$$

The full flux dependence of the ground state energy of the Mott insulator ($n = 1$) in the thermodynamic limit has been shown [145] to be

$$E(n, \Phi) - E(n, 0) = \frac{2D_c(n)}{L}(1 - \cos\Phi), \tag{C.3}$$

while for the non-half filled case and $L \to \infty$, the flux dependence is

$$E(n,\Phi) - E(n,0) = \frac{D_c(n)}{L}\Phi^2. \tag{C.4}$$

$D_c(n)$ is the charge stiffness.

We denote $E^{BA}(n_{BA},\Phi_{BA})$ and $E^0(n_0,\Phi_0)$ as the ground state energies for the interacting system (first term in equation (5.57)) and non-interacting system (second term in equation (5.57)) respectively. Since we deal with the away from half-filling cases, we write

$$\begin{aligned} E^{BA}(n_{BA},\Phi_{BA}) =& E^{BA}(n_{BA},0) + \frac{D_c^{BA}(n_{BA})}{L}\Phi_{BA}^2 \\ E^0(n_0,\Phi_0) =& E^0(n_0,0) + \frac{D_c^0(n_0)}{L}\Phi_0^2, \end{aligned} \tag{C.5}$$

and

$$\begin{aligned} j^{BA}(n_{BA},\Phi_{BA}) =& 2\frac{D_c^{BA}(n_{BA})}{L}\Phi_{BA} \\ j^0(n_0,\Phi_0) =& 2\frac{D_c^0(n_0)}{L}\Phi_0. \end{aligned} \tag{C.6}$$

The fundamental requirement of the KS mapping is that $n_{BA} = n_0 = n$ and $j^{BA} = j^0 = j$ while noting that $\Phi_{BA} = \Phi$ and $\Phi_0 = \Phi^s$ in equation (5.57). Substituting equation (C.5) and expressions for Φ^s and Φ obtained from equation (C.6) into equation (5.57) gives

$$E^{xc}(n,j) = E^{BA}(n,0) - E^0(n,0) - E^H(n) + \frac{L}{2}\Lambda^{xc}(n)j^2, \tag{C.7}$$

where

$$\Lambda^{xc}(n) = \frac{1}{2}\left[\frac{1}{D_c^0(n)} - \frac{1}{D_c^{BA}(n)}\right]. \tag{C.8}$$

$D_c^0(n)$ is the non-interacting charge stiffness defined by

$$D_c^0(n) = \frac{2t}{\pi}\sin\left(\frac{n\pi}{2}\right) \tag{C.9}$$

for $L \to \infty$ and $D_c^{BA}(n)$ is calculated using (5.33). Therefore,

$$e^{xc}(n,j) = e^{xc}(n,0) + \frac{1}{2}\Lambda^{xc}(n)j^2, \tag{C.10}$$

so that

$$v^{xc}_{BALDA}(n_l, j_l) = \frac{\partial e^{xc}(n,j)}{\partial n}|_{n\to n_l, j\to j_l}, \tag{C.11}$$

and

$$\Phi^{xc}_{BALDA}(n_l, j_l) = \frac{\partial e^{xc}(n,j)}{\partial j} = \Lambda^{xc}(n)j|_{n\to n_l, j\to j_l}. \tag{C.12}$$

Appendix D

Data used to generate the colour plots in Chapter 4

The tables shown below contain the data used to produce the colour plots of Figures 4.1 and 4.2 in Chapter 4.

L	BALDA	Number of electrons				
		2	4	6	8	10
3	LSOC	-0.651(2.3)				
	FN	-0.636(4.7)				
4	LSOC	-0.658(0.3)				
	FN	-0.641(2.4)				
5	LSOC	-0.605(0.9)	-0.662(3.3)			
	FN	-0.589(1.7)	-0.653(4.6)			
6	LSOC	-0.545(1.1)	-0.736(0.1)			
	FN	-0.531(1.4)	-0.720(2.3)			
7	LSOC	-0.491(1.2)	-0.740(1.1)	-0.649(3.4)		
	FN	-0.479(1.2)	-0.721(1.5)	-0.643(4.3)		
8	LSOC	-0.444(1.1)	-0.716(1.6)	-0.736(0.8)		
	FN	-0.434(1.0)	-0.696(1.1)	-0.724(2.3)		
9	LSOC	-0.404(1.1)	-0.681(1.8)	-0.768(0.6)	-0.638(3.2)	
	FN	-0.396(0.9)	-0.662(0.9)	-0.752(1.5)	-0.633(3.9)	
10	LSOC	-0.370(1.0)	-0.643(1.9)	-0.771(1.4)	-0.722(1.1)	
	FN	-0.363(0.7)	-0.626(0.8)	-0.752(1.1)	-0.714(2.3)	
11	LSOC	-0.340(0.9)	-0.606(1.9)	-0.757(1.8)	-0.766(0.2)	-0.629(3.0)
	FN	-0.335(0.5)	-0.591(0.7)	-0.738(0.9)	-0.753(1.5)	-0.625(3.5)
12	LSOC	-0.315(0.8)	-0.572(1.8)	-0.736(2.0)	-0.785(1.0)	-0.708(1.3)
	FN	-0.311(0.6)	-0.558(0.6)	-0.716(0.7)	-0.768(1.1)	-0.701(2.2)
13	LSOC	-0.293(0.8)	-0.539(1.8)	-0.711(2.1)	-0.787(1.5)	-0.756(0.2)
	FN	-0.289(0.5)	-0.527(0.6)	-0.691(0.7)	-0.768(0.9)	-0.746(1.5)
14	LSOC	-0.274(0.7)	-0.510(1.7)	-0.684(2.2)	-0.779(1.8)	-0.783(0.66)
	FN	-0.271(0.9)	-0.498(0.5)	-0.665(0.6)	-0.759(0.7)	-0.769(1.14)

Table D.1: Total energy per site, E_0/L, for different L and N for OBC and $U/t = 4$. The percentage deviation, Δ, from the ED in parenthesis.

L	BALDA	Number of electrons				
		2	4	6	8	10
3	LSOC	-1.068(2.6)				
	FN	-1.052(1.0)				
4	LSOC	-0.879(2.8)				
	FN	-0.858(0.4)				
5	LSOC	-0.736(2.6)				
	FN	-0.718(0.2)				
6	LSOC	-0.629(2.4)	-0.735(6.2)			
	FN	-0.614(0.1)	-0.718(8.3)			
7	LSOC	-0.547(2.1)	-0.752(3.2)	-0.788(1.5)		
	FN	-0.536(0.0)	-0.732(5.8)	-0.782(0.8)		
8	LSOC	-0.484(1.8)	-0.732(1.6)	-0.848(1.7)		
	FN	-0.475(0.0)	-0.711(4.4)	-0.837(0.3)		
9	LSOC	-0.433(1.6)	-0.698(0.7)	-0.860(2.1)	-0.662(3.6)	
	FN	-0.426(0.0)	-0.678(3.5)	-0.844(0.2)	-0.658(4.2)	
10	LSOC	-0.392(1.4)	-0.659(0.2)	-0.847(2.5)	-0.750(1.9)	
	FN	-0.386(0.0)	-0.641(2.9)	-0.827(0.1)	-0.742(3.0)	
11	LSOC	-0.357(1.2)	-0.621(0.2)	-0.821(2.7)	-0.795(0.7)	-0.709(1.0)
	FN	-0.353(0.0)	-0.605(2.4)	-0.800(0.1)	-0.782(2.3)	-0.706(0.5)
12	LSOC	-0.328(1.1)	-0.584(0.4)	-0.789(2.8)	-0.812(0.2)	-0.780(1.0)
	FN	-0.325(0.0)	-0.570(2.1)	-0.768(0.1)	-0.796(1.9)	-0.773(0.3)
13	LSOC	-0.304(1.0)	-0.550(0.5)	-0.756(2.8)	-0.813(0.8)	-0.820(1.4)
	FN	-0.301(0.0)	-0.538(1.8)	-0.735(0.0)	-0.794(1.6)	-0.810(0.2)
14	LSOC	-0.283(0.9)	-0.519(0.5)	-0.722(2.8)	-0.803(1.2)	-0.840(1.80)
	FN	-0.280(0.0)	-0.508(1.6)	-0.703(0.0)	-0.783(1.3)	-0.826(0.10)

Table D.2: Total energy per site, E_0/L, for different L and N for PBC and $U/t = 4$. The percentage deviation, Δ, from the ED in parenthesis.

L	BALDA	Number of electrons				
		2	4	6	8	10
3	LSOC	-0.582(5.6)				
	FN	-0.568(7.7)				
4	LSOC	-0.623(1.3)				
	FN	-0.607(3.7)				
5	LSOC	-0.584(0.2)	-0.560(6.5)			
	FN	-0.570(2.5)	-0.551(7.9)			
6	LSOC	-0.532(0.2)	-0.667(1.8)			
	FN	-0.520(1.9)	-0.654(3.8)			
7	LSOC	-0.482(0.4)	-0.692(0.1)	-0.532(6.3)		
	FN	-0.472(1.6)	-0.676(2.4)	-0.526(7.4)		
8	LSOC	-0.437(0.5)	-0.681(0.7)	-0.646(2.5)		
	FN	-0.430(1.3)	-0.665(1.7)	-0.636(4.0)		
9	LSOC	-0.399(0.5)	-0.655(1.0)	-0.700(0.6)	-0.512(5.7)	
	FN	-0.393(1.1)	-0.640(1.4)	-0.686(2.5)	-0.507(6.7)	
10	LSOC	-0.366(0.5)	-0.624(1.2)	-0.717(0.4)	-0.620(2.7)	
	FN	-0.361(0.9)	-0.609(1.2)	-0.702(1.8)	-0.612(4.0)	
11	LSOC	-0.338(0.5)	-0.591(1.3)	-0.715(1.0)	-0.683(1.0)	
	FN	-0.333(0.8)	-0.578(1.0)	-0.699(1.4)	-0.672(2.6)	
12	LSOC	-0.313(0.5)	-0.560(1.3)	-0.702(1.3)	-0.716(0.0)	-0.597(2.8)
	FN	-0.309(0.7)	-0.548(0.9)	-0.686(1.1)	-0.703(1.8)	-0.590(3.9)
13	LSOC	-0.291(0.4)	-0.530(1.3)	-0.683(1.5)	-0.730(0.7)	-0.662(1.3)
	FN	-0.288(0.6)	-0.519(0.8)	-0.667(1.0)	-0.715(1.4)	-0.653(2.7)
14	LSOC	-0.273(0.4)	-0.502(1.2)	-0.661(1.6)	-0.732(1.1)	-0.703(0.29)
	FN	-0.270(0.6)	-0.492(0.7)	-0.646(0.8)	-0.715(1.1)	-0.692(1.85)

Table D.3: Total energy per site, E_0/L, for different L and N for OBC and $U/t = 6$. The percentage deviation, Δ, from the ED in parenthesis.

Appendix E

Publications stemming from this work

• Exchange parameters from approximate self-interaction correction scheme, A. Akande and S. Sanvito, J. Chem. Phys. **127**, 034112, (2007). Also cond-mat/0704.1572.

• Electric field response of strongly correlated one-dimensional metals: a Bethe-Ansatz density functional theory study, A. Akande and S. Sanvito, Phys. Rev. B. **82**, 245114 (2010). Also cond-mat/1010.2860.

• Persistent current and Drude weight for the one-dimensional Hubbard model from current-lattice density functional theory, A. Akande and S. Sanvito, Submitted to Phys. Rev. B. Also Also cond-mat/1012.5908.

Other works not included in this thesis

• Energetics of 2D and 3D repulsive Hubbard model from their 1D counterpart using dimensional scaling for arbitrary fillings, A. Akande and S. Sanvito, (in preparation).

- Electronic structure of Quantum Dot in the Coulomb Blockade regime, A. Akande.